ABSTRACT

Title of Document:	Multi-scale Modeling of soft matter: Gas Vesicles and Red Blood Cells
	Hussein M. Ezzeldin, 2012
Directed by:	Assistant Professor Santiago D. Solares.
	Department of Mechanical engineering

Modeling of soft matter, nowadays, became an extremely active research field due to the advancement in computational power and theoretical physics. Not only because we can access and study larger length scales and longer time scales, but also, the ability to model more complex systems. In this dissertation, we utilized the state-of-the-art computational and theoretical tools to model and study two systems.

The first system is gas vesicles, a proteineous organelle that exist in microorganisms such as archea and bacteria. The structure and assembly process of gas vesicles have received significant attention in recent decades, although relatively little is still known. In this work we develop a model for the major gas vesicle protein, GvpA, and explore its structure within the assembled vesicle. Elucidating this protein's structure has been challenging due to its adherent and aggregative nature,

which has so far precluded in-depth biochemical analyses. Moreover, GvpA has extremely low similarity with any known protein structure, which renders homology modeling methods ineffective. Thus, alternate approaches were used to model its tertiary structure. Starting with the sequence from haloarchaeon *Halobacterium sp.NRC-1*, we performed *ab-initio* modeling and threading to acquire a multitude of structure decoys, which were equilibrated and ranked using molecular dynamics and mechanics, respectively. The highest ranked predictions exhibited an α-β-β-α secondary structure in agreement with earlier experimental findings, as well as with our own secondary structure predictions. Afterwards, GvpA subunits were docked in a quasi-periodic arrangement to investigate the assembly of the vesicle wall and to conduct simulations of contact-mode atomic force microscopy imaging, which allowed us to reconcile the structure predictions with the available experimental data. Finally, the GvpA structure for two representative organisms, *Anabaena flos-aquae* and *Calothrix sp. PCC 7601*, was also predicted, which reproduced the major features of our GvpA model, supporting the expectation that homologous GvpA sequences synthesized by different organisms should exhibit similar structures.

The second system studied in this dissertation is red blood cells and their hemolytic processes. Due to the significant progress that has been achieved in the treatment of patients with cardiovascular diseases, procedures such as heart valve replacements, either with mechanical or biological substitutes, have become routine operations. However, despite this progress, the use of cardiovascular implants always results in changes to the blood fluid dynamics, such that undesired damage to red blood

cells (hemolysis) occurs. This type of damage, which can also be brought about by certain medical procedures, such as dialysis, reduces the ability of the circulatory system to transport oxygen and carbon dioxide. To gain a deeper understanding of the conditions leading to hemolysis and to aid in the design of low-hemolysis cardiovascular implants, this document proposes the development of a coarse-grained dynamics model to simulate red blood cells, which will be integrated into a computational fluid dynamics solver and packaged into an integrated software tool. A novel aspect of the proposed model will be its ability to reproduce interactions between different red blood cells in large scale simulations, as well as hemolysis at the single-cell level due to the stresses imparted by the fluid. The model will be validated against previous experiments reported in the literature and will also be used to simulate model biodevices.

Multi-scale Modeling of Soft Matter: Gas Vesicles and Red Blood Cells

by

Hussein M Ezz Eldin

Dissertation submitted to the Faculty of the Graduate School of the
University of Maryland, College Park in partial fulfillment
of the requirements for the degree of
Doctor of Philosophy
2012

Advisory Committee:
Assistant Professor Santiago Solares, Chair/Advisor
Professor Amr Baz
Professor Michael Zachariah
Associate Professor Elias Balaras
Associate Professor Srinivasa R. Raghavan, Dean‘s Representative

Acknowledgments

I owe my gratitude to all the people who have made this thesis possible and because of whom my graduate experience has been one that I will cherish forever.

First and foremost I'd like to thank my advisor, Dr.Santiago Solares for giving me an invaluable opportunity to work on challenging and extremely interesting projects over the past four years. He has always made himself available for help and advice and there has never been an occasion when I've knocked on his door and he hasn't given me time. It has been a pleasure to work with and learn from such an extraordinary individual.

I would also like to thank my professors, Dr. Jeffery Klauda and Dr.Elias Balaras. Without their extraordinary theoretical ideas and computational expertise, this thesis would have been a distant dream. Also, we would like to thank Marco D. de Tullio for providing the data for the pathlines used in studying the real device simulation. Thanks are due to Professor Amr Baz, Professor Michael Zachriah and Professor Ragahvan Sirini for agreeing to serve on my thesis committee and for sparing their invaluable time reviewing the manuscript.

My colleagues at my group, Dr.Gaurav Chawla, Josh Crone, Charles A. Wright, Dr. lynn Munday and Adam Kareem, have enriched my graduate life in many ways and deserve a special mention. Also, my dear friend and colleague, Dr. Marcos

Vanella, helped me start-off by teaching me writing the basic simulation code in Fortran. .

I owe my deepest thanks to my family - my mother, father and my wife, Hala, who have always stood by me and guided me through my career, and have pulled me through against impossible odds at times. Words cannot express the gratitude I owe them.

I would like to acknowledge the financial support from the U.S. National Science Foundation (NSF) OCI-0904920 and CMMI-0841840 grant for all the projects discussed herein.

I apologize to those I've inadvertently left out.

Lastly, thank you all and thank God!

Contents

List of Tables

List of Figures

List of Abbreviations and Symbols

AFM	Atomic force microscopy
BDI	Blood damage index
CG	Coarse graining
CFD	Computational fluid dynamics
DPD	Dissipative particle dynamics
EI	Elongation index
HV	Heart valves
OT	Optical tweezers or optical traps
RBCs	Red blood cells
MA	Micropipette aspiration
MD	Molecular dynamics
MTC	Magnetic twisting cytometry
NIH	Normalized index of hemolysis
PHVs	Prosthetic heart vlaves
d	Separation between two adjacent RBCs surfaces
K	Area modulus of compression
k_B	Boltzmann constant
T	Temperature
k_a	Global area constraint constant
k_b	Bending rigidity (its units depend on the context)
k_d	Local area constraint constant
N^M	Force scaling basis
$(K_BT)^M$	Energy scaling basis
pHb	Normal plasma free hemoglobin
r	Distance between adjacent RBCs
r^M	Length scaling basis
ΔpHb	Increase in plasma free hemoglobin
δ	Thickness of the attached polymer
γ	Coefficient of friction for the DPD dissipative forces
Δ	Depletion thickness layer
ϕ	Distortion parameter of the strain-based hemolysis model
ϕ_I(r)	Interaction energy between two RBCs
κ	Debye-Hückel length
κ_c	Bending rigidity
μ	Shear modulus of the red blood cell
μ_d	Dynamic viscosity of fluid
μ_o	Shear modulus for the RBC two-dimensional network
μ_s	Mean deviation of Gaussian curve
Π	Osmotic pressure of the depletion-mediated
σ	Amplitude of noise for the random DPD random forces
σ_s	Standard deviation of the Gaussian
ω	Amplitude of the Gaussian
ω_E	Electrostatic component of the interaction energy between two RBCs

ω_D	Dissipative forces weighting function
ω_{Dep}	Depletion component of the interaction energy between two RBCs
ω_R	Random forces weighting function

Chapter 1

Introduction

Colloids, synthetic or bio-polymers, gels, fabrics, paint, biological macromolecules, etc. are very few, of the countless number of, examples of "soft matter" (see Figures 1.1 & 1.2) [1, 2, 3]. Soft matter clearly exists in almost everything. Therefore, understanding the mechanics and properties of soft matter are invaluable. Like every matter, soft matters are composed of varies constituents, however, colloidal systems for example are distinct from liquids or crystals of small molecules because the former usually consists of extremely large molecules. The inhomogeneity of these composites is still visible even on the micrometers scale, as shown in Figure 1.1a. Therefore, the softness of "soft matter" is attributed to the large size of the dispersed constituent that are held together with a weak interaction on the energy scale of $\sim K_B T$, which is two orders of magntidude less than that of molecular crystals.

Studies on soft matter systems started in the early 19th century, mainly on dispersion colloids, small amphiphiles and polymers [3], which usually, are systems consisting of "particles" that have a size in the range of 1 nm to 10 μm suspended

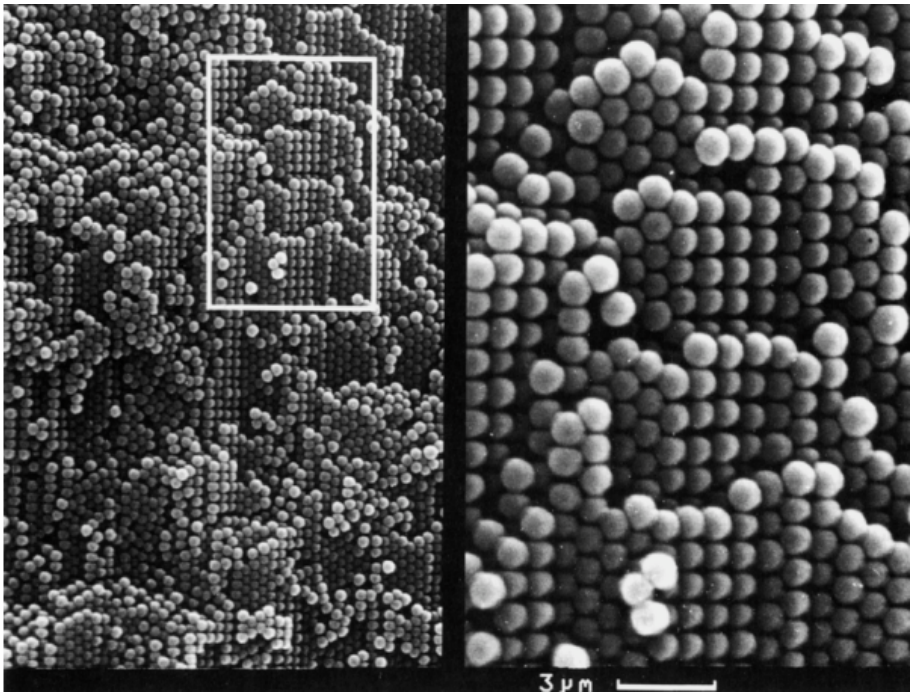

(a)

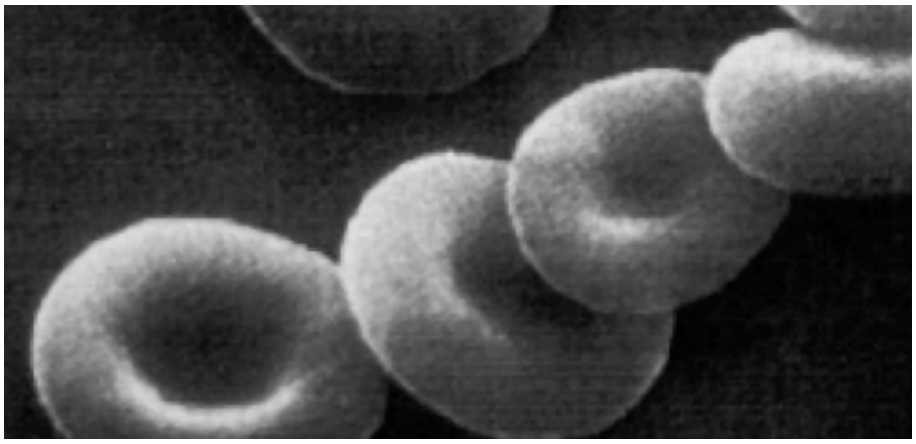

(b)

Figure 1.1: Examples of soft matter systems. (a) Transmission electron microscopy (TEM) picture of a colloidal crystal of spherical particles. The figure on the right is an enlargement of the part indicated by the white square in the figure on the left. The ordered arrangement of the colloidal particles is clearly visible [3]. (b) a suspension RBCs [3].

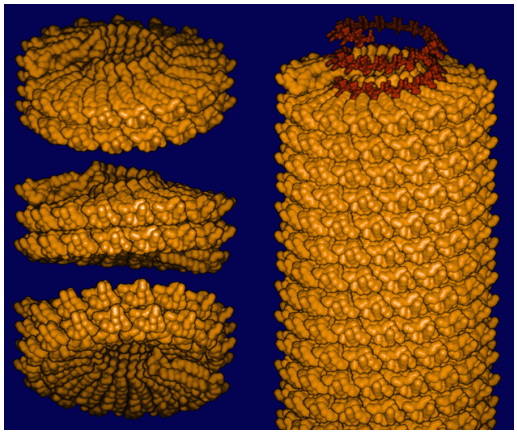

(a)

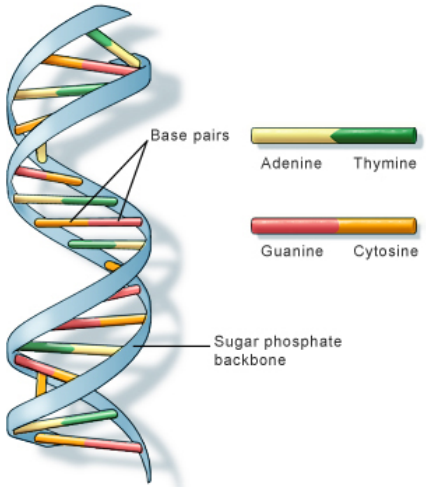

(b)

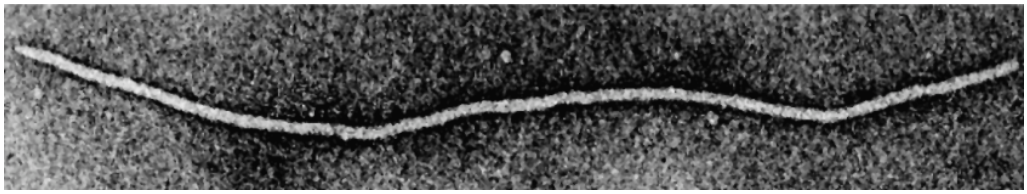

(c)

Figure 1.2: Tobacco mosaic virus particle and three views of the nucleating aggregate of its coat protein (taken from http://www.sb.fsu.edu/~caspar/). (b) DNA double helix formed by base pairs attached to a sugar-phosphate backbone (taken from http://ghr.nlm.nih.gov/handbook/basics/dna). (c) An fd virus has the shape of a long, semi-flexible rod. It has a diameter of about 6 nm, a length of 880 nm, and persistence length of about 2.2 μm [3].

in a solvent. These particles exist in the "powder" form when dry. Also, these particles have different shapes, for example, spherical as in silica suspensions, rigid rods, such as tobacco mosaic virus (Figure 1.2a), double-stranded DNA fragments (Figure 1.2b) and semi-flexible rods, such as the fd virus (Figure 1.2c). Although, we refer to the dispersed phase in soft matter systems as "large", they are small enough to exhibit thermal motion, i.e. Brownian motion. The methods and tech-

niques used in modeling soft matter systems are extended by the vast range of length and time scales of these systems. Simulation techniques such as molecular dynamics is usually used for the atomistic systems in the order of tens of nanometers. While, for larger systems mesoscopic methods such as Lattice Boltzman Method (LBM) and Dissipative Particle Dynamics (DPD) are more appropriate. These methods rely on a coarse-grained approach, where few hundred atoms are modeled as one particle. In addition, the high repulsive potentials between atoms, used in atomistic scale simulations (MD simulation), are replaced by a softened potential that allow using larger time steps, which gives access to longer simulation time.

In the work presented here two levels of simulations techniques were used. First, we used molecular dynamics for modeling and visualizing the gas vesicle protein (GVP) *in-silico*. While, for modeling blood flow through heart assisted devices such as prosthetic heart valves (PHVs) we used DPD coarse-grained model for simulating red blood cells that make ∼45% of the blood volume.

After this brief introduction about modeling of soft matter. First, we lay down the objectives of this dissertation in chapter 2. Then, in chapter 3 the macromolecular modeling and simulation of the gas vesicle protein A is discussed. While, in chapter 4 we present the worked done on the modeling of red blood cells and hemolysis processes. Finally, chapter 5 concludes by listing the intellectual contributions and anticipated benefits of this thesis.

Chapter 2

Dissertation Objectives

Below are the objectives we had in mind when conducting our research. We start with the objectives for the GvpA modeling, followed by the objectives for red blood cells.

Gas Vesicles Objectives

1. Gain a deeper understanding of the vesicle constituents and their structure
2. Build a model for GvpA subunit, which will be used to build a model for the gas vesicle walls
3. Achieve a milestone for a long-term multi-scale simulation method that could eventually be used to perform coarse-grained simulations of the entire gas vesicle

Red Blood Cells Objectives

1. Study the effect of hydrodynamic loading on RBCs, primarily due to shear loads that are known to cause RBC membrane trauma [4]. Throughout the body, blood is subjected to different flow conditions and geometries, therefore, an accurate representation of its components will allow better modeling of its rheology. Additionally, it is necessary to model the microscopic behavior of RBCs under varying loads, i.e. sinusoidal loads, as well as clusters of RBCs, in order to identify the dominant factors in blood damage.

2. Investigate the different loading scenarios that exist in biodevices that are used daily in treatments such as dialysis tubing, filters and blood pumps and downstream of the flow of implanted prosthetic heart valves [5], i.e., mechanical aortic and mitral heat valves. Therefore, studying the extent of damage of each scenario will aid in minimizing, if not eliminating, such negative effect by avoiding or reducing its occurrence in new designs.

3. Study mechanical hemolysis in biodevices such as prosthetic heart valves, capillaries and blood pumps. This will be done by introducing a comprehensive and rigorous blood-damage model that accounts for the different characteristic of the hemolysis phenomenon, which are neglected in today's blood-damage models [6, 7, 8].

Chapter 3

Gas Vesicles Proteins

3.1 Background

Gas vesicles are proteinous, lipid-free organelles commonly found in diverse prokaryotic species inhabiting aquatic environments, including both Archaea (halophiles, such as Halobacterium sp. NRC-1, and methanogens) and Bacteria (phototrophs and heterotrophs) [9, 10, 11, 12, 13]. Ecological studies have shown that they aid in cell buoyancy processes, such as in the stratification of cyanobacterial and halobacterial species (which increases their ability to respire and photosynthesize), although their function in other microorganisms, such as methanogens and soil bacteria, is unclear [14, 15, 13, 16]. Their morphology is organism dependent and can be found in cylindrical shapes with conical caps or lemon shapes [13], as shown in figure 3.1. They range in length from 50 nm to over 1 μm and in width from 30 to 250 nm [10, 17]. Interestingly, while these vesicles are hollow, gas-filled structures, they do not possess balloon characteristics. Instead, their membrane is permeable to

gases, and even to molecules as large as perfluorocyclobutane [18], but not to water [19, 20, 21]. Calculations have shown that if any pores exist across the membrane and if they are lined with hydrophobic material or open onto a hydrophobic inner surface, water surface tension should prevent water molecules from crossing the membrane. Additionally, experiments show that vesicles strongly prefer aqueous environments to oily phases, which suggests that they have a hydrophilic outer surface [19]. Thus, it has been postulated that their inner surface is hydrophobic while their outer surface is hydrophilic, which could be accounted for by the distribution of polar and non-polar side groups in the amino acids that form their proteinous membrane [19].

Earlier work by DasSarma et al. [10, 23, 24] determined that the successful formation of gas vesicles requires a gene cluster of 13 to 14 genes. Nevertheless, no clear evidence has yet been gathered regarding the existence of all the corresponding proteins in the gas vesicle membrane. Up to now, eight of them have been identified, of which seven are associated with gas vesicles [25, 26]. Most importantly, the two proteins GvpA and GvpC have been identified as the main constituents. The former typically comprises about 90% of the membrane mass, while the latter has been reported to typically constitute less than 10% [13, 26]. Previous work has showed that gas vesicle integrity is not significantly affected after releasing GvpC with sodium dodecyl sulfate [27] or urea [26]. This result, along with the vesicles's biocompatibility [28], biodegradability and operability over a broad range of conditions (including high salt concentrations, which enables their cultivation un-

Figure 3.1: Gas vesicles in a freeze-fractured cell of *Prosthecomicrobium pneumaticum* showing the varies shapes of the vesicles, the lemon shaped and the cylindrical with conical caps. The ribs on the surface of the membrane are clearly shown [22].

der nonsterile cost-effective conditions [29], potentially makes them highly advantageous bionanoparticles for applications such as vaccination [30, 31] and drug delivery

[32, 33, 34, 35]. Using such particles could, for example, avoid some of the health hazards associated with man-made nanoparticles [36, 37]. Moreover, gas vesicle synthesis and purification are relatively simple and well-established processes that can lend themselves to industrial optimization [30, 38, 31]. In a study by DasSarma et al. [39] using DNA microarray assay techniques to investigate gene expression in Halobacterium sp. NRC-1 under different environmental stressors, such as high and low salinities, high and low temperatures, low oxygen concentrations and heat shocks, it was observed that the expression of gas vesicle genes increased under cold temperatures, which assists Halobacterium in floating to the surface looking for warm places. Therefore, controlling the incubation temperature, for example, could be used as a means to boost gas vesicle production.

We began our structure prediction employing homology modeling. However, due to the uniqueness of the GvpA protein sequence, this analysis could neither be carried out with confidence nor provide structures that agreed with the available experimental data [40, 41, 12]. Thus, we turned to methods that do not depend on a template, namely, threading (using the I-TASSER web server [42]) and ab initio modeling (using the Rosetta software [43]). Both of these techniques, amongst others, have been tested extensively in the biennial CASP experiments (predictioncenter.org), which involve prediction of numerous targets in various categories [44]. Relevant to our case is the template-free prediction category, whereby templates are not available due to weak homology. For this category, the most successful groups in CASP6 [45], CASP7 [46] and CASP8 [47]) used methods

relying on *ab-initio* modeling (Rosetta), which have shown sensible improvements over the course of the CASP experiments [44]. Additionally, I-TASSER was declared the best server predictor in CASP8 and the second best in CASP7 (the official CASP7 and CASP8 results can be found in (predictioncenter.org/casp7/ & predictioncenter.org/casp8/)). Both approaches have been used in numerous cases involving peptide lengths and structures comparable to those of GvpA [47, 48, 44, 45, 49, 46].

In the present study, a series of tertiary structures were predicted for GvpA from Halobacterium sp. NRC-1 using threading, ab initio modeling and homology modeling. These structures were then equilibrated using constant temperature and pressure (NPT) molecular dynamics and ranked according to total energy using the Molecular Mechanics-Poisson Boltzmann Surface Area (MM-PBSA) method [50]. The top ranked structures were in agreement with previous experimental results [9, 40, 41, 12] and in good qualitative agreement with the previous structure prediction of Strunk et al. [51] and their point mutation experiments. Although our approach overlaps with theirs, we differ in the model base used, in the all-atom refinement techniques, in the procedure used to model GvpA dimerization and in the inclusion of predicted topographical images.

Additionally, a sequence identity analysis was conducted, which identified 65 GvpA sequences synthesized by various organisms exhibiting at least 35% sequence identity with the GvpA from Halobacterium sp. NRC-1. The tertiary structures of

two representative GvpA sequences from this group, exhibiting 50% sequence identity towards that of Halobacterium sp. NRC-1 (Anabaena flos-aquae and Calothrix sp. PCC 7601) were calculated and compared to the highest ranked structures in the MM-PBSA calculations, and showed similar structural features. Finally, GvpA subunits were docked in a quasi-periodic arrangement to investigate the assembly of the vesicle wall. Using this structure we conducted simulation of contact-mode atomic force microscopy (AFM) imaging, which allowed us to reconcile our results with the available experimental data.

3.2 Methods and Techniques

3.2.1 Structure Prediction

Secondary structure prediction

The 76-residue primary structure of GvpA in Halobacterium sp. NRC-1 has been fully determined through both protein sequencing [52] and gene/genome sequencing [53, 54] (see Figure 3.3, first row). To assist our tertiary structure prediction study, we performed a secondary structure prediction analysis of this sequence using the PORTER [55], SSPro [56], Jpred3 [57], NNpredict [58], DSC [59], MLRC [60], PHD [61], and PSIPRED [62] web servers (see Appendix A, whose algorithms unanimously predicted two β-sheets (yellow marked residues) and two α-helices (blue marked residues) as illustrated in Figure 3.3 (first row). Both X-ray diffraction data [9] and infrared spectra [40, 41], which detected the existence of β-sheets in the GvpA from Anabaena flos-aquae, are in agreement with the consensus of the secondary structure analysis. It is important to note that the structural data from IR spectroscopy are more accurate than those provided by X-ray diffraction, since the former is free of alignment or fitting errors [63, 64]. Therefore, the evidence provided by Jones and Jost [41] about the existence of α-helices in GvpA cannot be overlooked even though the X-ray diffraction analysis could not detect their existence. It is also worth mentioning that although those experimental studies are based on organisms other than Halobacterium sp. NRC-1, Walker et al. [52] showed

that the GvpA synthesized by six different organisms are homologous, amongst them cyanobacterium Anabaena flos-aquae and archaeon Halobacterium. Thus, it is not unreasonable to expect a priori that our tertiary structure predictions should exhibit general agreement with the available experimental data.

Tertiary structure prediction

Tertiary structure prediction was initially attempted using homology modeling techniques [56, 65], whereby the target sequence is run against sequences of all structurally known proteins using scoring matrices (e.g. BLOSUM62) to detect sequence identity. The sequences that match the target are called templates, whose backbone torsional angles are then used to predict the target backbone. We used the MODELLER [65, 66] and SCRATCH [56] methods to perform this analysis. First, the homology of GvpA was probed by running its sequence against multiple databases, amongst them MODBASE [67] and BLAST [68]. The MODBASE results detected no homology with solved structures using a threshold of 30% sequence identity. Similarly, BLAST detected a few templates with a maximum score of 27% sequence identity only when partial alignment was considered (i.e., when only part of the peptide was aligned). Consequently, the structures obtained from homology modeling neither agreed with the experimental data nor with our secondary structure prediction. Although our confidence on the two structures obtained was minimal, these were incorporated in further analyses (see below) in order to eliminate any method bias and to allow for inclusion of a significant set of structure

prediction techniques. In the remainder of the paper, the two homology derived structures will be referred to as MOD and SCH, as abbreviations for MODELLER and SCRATCH, respectively.

We continued our study using threading, which is a technique where the target sequence is compared against a set of sequences, which are known to correspond to given secondary structure folds (i.e., β-sheets or α-helices). The target sequence is "threaded" through these benchmark sequences to determine the best fold based on a pseudo-potential. We conducted this analysis using the I-TASSER web server [69], which combines a hierarchical protein structure modeling approach based on the secondary-structure enhanced Profile-Profile threading Alignment (PPA) [70] and the iterative implementation of the Threading ASSEmbly Refinement (TASSER) program [70]. I-TASSER provided the top 5 models of its prediction, which were ranked according to the I-TASSER energy function. The top 3 structures obtained from this prediction showed better agreement with the available data than those obtained from MODELLER or SCRATCH, as they possessed the secondary structure features depicted in the first row of Figure 3.3 (this figure also shows a comparison of the predicted secondary structure and that of the top 10 tertiary structures predicted in our study). The I-TASSER models were given the names 1_IT, 2_IT, up to 5_IT, resembling the I-TASSER sorter name convention.

We then turned to *ab-initio* structure prediction, which has shown to be a promising technique in template-free predictions, where combined methods of fragment as-

sembly and knowledge-based energy expression are used, especially for peptides containing less than 100 residues [71]. This method is based on calculating the propensity of the amino acid residues to adopt local structures, using an energy function that describes the interaction between different amino acids and the secondary structure assignment. This analysis was performed using the Rosetta suite 2.3 software [43], one of the most successful algorithms in CASP [47, 48, 44, 45, 49, 46]. Rosetta first uses a Monte Carlo algorithm for fragment assembly. Through a multi-stage process it then provides multiple decoys ranked according to an energy expression. We selected the top 20 structures ranked by the Rosetta score. In addition, all the decoys were clustered using a pair-wise RMSD based script associated with Rosetta. The centers of these clusters represent deeper regions of the energy landscape and the size of the cluster can be thought of as being proportional to the structure entropy. That is, larger size clusters have higher entropy, and thus, lower free energy. The top 20 Rosetta structures were given the names 1_R, 2_R, up to 20_R, where R stands for Rosetta and the numbers indicate the ranking according to the Rosetta score. We also included the centers of the top 5 clusters of decoys and they were named 1_RC, 2_RC, up to 5_RC.

3.2.2 Structure Equibiration and Total Energy Ranking

Molecular Dynamics (MD)

All the above structures were then equilibrated through molecular dynamics (MD) using a protocol based on earlier work by Lee et al. [72]. The structures were

prepared for the production phase using a four-step procedure. First, their geometry was optimized by energy minimization. Second, each was embedded in a box of solvent (TIP3P model for water) with 10 Åpadding in all directions. Third, energy minimization was performed for the water molecules alone to remove any unfavorable van der Waals interactions and to obtain a better orientation for the closest molecules around the protein. The minimization was continued until the change in the solvent energy was below 0.25 kcal/mol. Lastly, an equilibration phase was implemented to gradually heat the system from 0 to 300 K by performing sets of unconstrained isochoric-isothermal (NVT) MD simulations over a period of 25 ps (with a 0.5 fs timestep), during which the water molecules were allowed to move freely to fill up any voids in the system. The actual production phase consisted of 4 ns of MD simulation using the NPT ensemble with periodic boundary conditions and the CHARMM22/CMAP force field [73]. Full electrostatic calculations were performed by implementing the Particle Mesh Ewald (PME) [74] method for far field and a grid spacing of 1 Å. The near field was cutoff at 12 Åwith a switching function up to 10 Å. A multi-step integrator algorithm (r-RESPA) [75, 76] with 1 fs for short-range and 2 fs for full electrostatics was implemented with a pair list distance of 13.5 Å. All hydrogen bonds and angles were constrained using the SHAKE algorithm [77] with a timestep of 2 fs. The Nosè-Hoover Langevin piston method [78] was used for pressure control. Langevin dynamics with a weak coupling constant was used for temperature control. The simulations were performed using the NAMD 2.6 [79] software on a Linux cluster. Each production phase run took an average of 10 hours of walltime running on 64 processors of different speeds ranging from 2.3 GHz up

to 3.3 GHz, using gigabit interconnects for communication.

MM-PBSA calculations

Further calculations were performed using the MM-PBSA method along with the experimental constraints available. This method, initially proposed by Srinivasan et al. [50] to study the stability of DNA, RNA, and phosphoramidate-DNA helices, has been used in a variety of applications similar to ours. For example, Lee et al. [72] illustrated its ability to distinguish the native structure among different predicted structures for a set of 12 proteins. The method was also used to quantify the free energy differences between states of the "headpiece" subdomain in the protein villin, showing that it is capable of predicting the correct conformation of the native, intermediate folding and denatured states [80].

The free energy in the MM-PBSA method is composed of two terms, the solute intra-molecular energy E_{MM} calculated using the molecular mechanics force field and the change in solvation energy ΔG_{solv}, which is the energy required to transfer a solute molecule (i.e., the protein) from one medium to another (in this case, from vacuum to solvent). The former term, E_{MM} was calculated using the CHARMM22/CMAP force field [73]. The solvation energy has two components, namely, a cavity formation energy and a nonbonded energy change consisting of van der Waals (VDW) and electrostatic interactions, which yields three terms:

$$\Delta G_{solv} = \Delta G_{elec} + \Delta G_{VDW} + \Delta G_{cav} \tag{3.1}$$

where ΔG_{elec} is the electrostatic contribution to the energy of solvation and is obtained from the solution of the Poisson-Boltzmann equation for a medium of multiple dielectric constants (i.e. for the protein and the solvent). The DelPhi IV [81, 82] software was used to calculate the solvation energy component due to polarization of the medium. The solvent (water) dielectric constant was set to 80.0 and the protein dielectric constant was set to 4.0, as determined experimentally for most proteins. The remaining two components of the solvation energy were calculated using the following equation to account for the effects of cavity formation and VDW interactions:

$$\Delta G_{VDW} + \Delta G_{cav} = \gamma A + b \tag{3.2}$$

where A is the solvent accessible surface area (SASA) for the protein molecule. It is clear from equation (3.2) that the other two components of the solvation energy (ΔG_{VDW} and ΔG_{cav}) have a linear dependency on the SASA, where γ and b are the constants defining this relation. This correlation can be justified by arguing that both the work required to create the cavity against the solvent pressure and the entropic penalty for solvent reorganization, in addition to the VDW interactions, are dependent on the solvent molecules in the first solvation shell, whose number depends linearly on the SASA. For the results reported here we used values of 7.2 kcal/mol $\mathring{A}^2$ and 0.0 for γ and b, respectively, as reported by Still et al. [83]. We also verified that the ranking of our structures was not highly sensitive to these values, and did not change when using 0.00542 kcal/mol $\mathring{A}^2$ and 0.92 Kcal/mol for γ and b, respectively, as proposed by Sitkoff et al [84]. This is because the dominant energy

terms were E_{MM} and ΔG_{elec}. The SASA, as defined by Lee and Richard [85], was calculated using a plug-in in the VMD software [86] with a probe radius of 1.4 $\mathring{A}$ for water molecules.

The procedure for calculating the MM-PBSA energies was automated using a Tcl script within the VMD software. First, each production trajectory was loaded into VMD, and then frames 4 ps apart were exported to the PDB format along with the calculated SASA value for each case. Second, for each configuration, NAMD was used to determine the intra-solute energy using the CHARMM22/CMAP force field [73]. Third, DelPhi software was used to calculate the first term in equation (3.1). Finally, the SASA value was multiplied by the constant γ and all terms were added to give the MM-PBSA value. Thus, explicit water was used to run the simulation, and a continuum model was used to estimate ΔG_{solv} with the finite-difference Poisson-Boltzmann model accounting for the polarization component and a linear surface-area-dependent term for the non-polar component.

Finally, all simulations were checked for equilibration and stability. While all the MD energy trajectories were stable, not all the MM-PBSA energies fluctuated about a constant value over the 4 ns of the production phase. Since the fluctuations were observed primarily in the first 3 ns, we conducted our final structure energy ranking based on the data extracted from the last nanosecond of the run (see Table 3.1 and Figure 3.3 for the average energy and standard deviation of each structure during this period). The goodness-of-fit of the energies to a normal distribution was verified

over this last nanosecond using χ^2 (Chi-squared) tests. All the structure energies were approximately normally distributed at the 95% confidence level, except for the five structures labeled, 2_IT, 1_RC, 12_R, 15_R, and 20_R. As discussed below, the only structure that would require further consideration is the 2_IT structure since all others had very low ranking. However, we also discuss in the next section that the fact that structure 2_IT is not fully equilibrated does not affect the conclusions of the study.

3.2.3 Docking and Atomic Force Microscopy Simulation

In constructing the GvpA-GvpA dimer we chose to align the large hydrophobic residue tryptophan (TRP) from both units together, which results in the alignment of the oppositely charged residues E40 and R42 (on the β-I segment) from the one unit with residues R42 and E40 from the adjacent subunit (see Figure 3.3) based on the configuration proposed by Sivertsen et al. (see Figure 7 in [87]), although without incorporating dissimilar GvpA units. This arrangement yielded a tight GvpA-GvpA docked structure. By simulating the AFM characterization process for two opposite faces of a layer of docked GvpA molecules, we determined the general orientation of the features predicted in the images. This information was then reconciled with the available experimental data [87, 51], which allowed us to confirm the hypothesis that the α-helices of GvpA in the vesicle wall are exposed to the hydrated medium, while the β-sheets constitute the interior lining. The AFM simulation methods used resemble previous work on the study of tapping-mode AFM

imaging of bacteriorhodopsin molecules [88, 89] except that we used contact-mode imaging, similar to the experimental work of McMaster and Walsby [12]. The sample consisted of 12 GvpA subunits docked together in a matrix arrangement of 4 rows by 3 columns, as shown in Figure 3.5. Our highest-ranked predicted structure 1_IT was used for this study. Each column had alternating subunits to form anti-parallel β-sheets in agreement with previous Fourier transform infrared spectroscopy results [87]. The periodicity of the system was simulated by imaging the two GvpA units in the center of the structure (these were considered to be the unit cell) and then replicating the same image in both horizontal directions. The substrate consisted of a layer of 001 mica. Since no information on the geometry of the cantilever tip was provided in [12], a spherical 001 silicon tip with a 10 nm radius of curvature (typical highest-resolution probe available at the time) was used (see Figure 3.5). The tip apex was slightly sharpened through the addition of a silicon bilayer and hydrogen atoms to enhance imaging resolution. The outer boundaries of the GvpA molecules surrounding the unit cell and all layers of the substrate, except the top layer, were kept fixed. The AFM images were constructed from a collection of 273 tip-sample force curves constructed by approaching the sample with the AFM tip on a horizontal 13×21 grid, whereby the tip-sample force was calculated at each vertical position of the probe using the steered molecular dynamics tool in NAMD 2.6 [79] with a vertical speed of 0.00005 $\mathring{A}$ per time step and a timestep of 0.25 fs. The surface topography was calculated by selecting the vertical tip position at each grid point that corresponded to the desired cantilever deflection (or force) setpoint within the contact-mode (static) AFM scheme [90, 12]

3.3 Results and Discussion

GvpA secondary and tertiary structure

Before discussing our results, we will digress to clarify two important aspects regarding our methodology. First, since NPT simulations were carried out, one could rely on the Gibbs free energy to distinguish amongst different structures. However, this would require knowledge of the enthalpy and entropy. While the former can be easily calculated, the entropy is very difficult to estimate. While normal mode analysis has been used by some to estimate the vibrational entropy of molecules [91, 92], a recent study by Lee and coworkers [72] showed that the contribution of the entropic term to the free energy is insignificant for a similar system to ours. Therefore, entropic effects were not considered here. Second, many of the gas vesicle carrying organisms (e.g., Archaea) are extremophiles and maintain an isotonic condition with their exterior [93]. In Halobacterium, gas vesicles dwell in a hypersaline intracellular environment with a concentration up to 5-6 M NaCl [93]. In contrast, the proteins were solvated in pure water in our simulations. This approach can be justified by considering that gas vesicle integrity is not altered significantly in distilled water [12]. Additionally, modeling the gas vesicles in their native environment with current pair-wise force fields [94], which have not been developed to simulate extreme conditions, would be inadequate and may yield inaccurate conformations. However, the solution salinity will be an important aspect to be considered in further analyses, in particular when incorporating the protein-protein interactions in

future full gas vesicle models.

The MM-PBSA energy values shown in Table 3.1 and Figure 3.2 are based on the ensemble average of the last 1 ns, containing 250 frames 4 ps apart, of the production trajectories. The individual values of E_{MM} and ΔG_{solv} were calculated for each snapshot, and then averaged. The two highest ranked structures were 1_IT (the best I-TASSER structure) followed by 3_RC (the third Rosetta structure) with only 2% difference in energy between them. A t-test with a confidence level of 95% indicated statistical difference between the top two structures and the rest of the structures. 2_R, 3_IT, 2_RC, and 2_IT follow the first two structures in the ranking with a 17-23% difference in energy from the 1_IT structure. Afterwards follow the remaining structures with $\sim$26% to $\sim$70% difference in energy compared to 1_IT structure.

When closely inspecting the secondary structure features of the top two structures, we confirm agreement with the IR spectroscopy results by Jones and Jost [41], ATR and FTIR results by Strunk et al. [51], and our secondary structure prediction analysis (Figure 3.3). They possess α-helices ($\sim$39%) and β-conformations ($\sim$26%) as can be seen in Figure 3.3 and Table 3.1 (the latter provides the content of α-helices, β-sheets and random coils in each structure). Upon examining the remaining structures, one can note that they gradually deviate from the secondary structure prediction (the first 5 are shown in Figure 3.6). Moreover, the loss of the secondary domains is obvious as one continues to inspect lower and lower ranked structures.

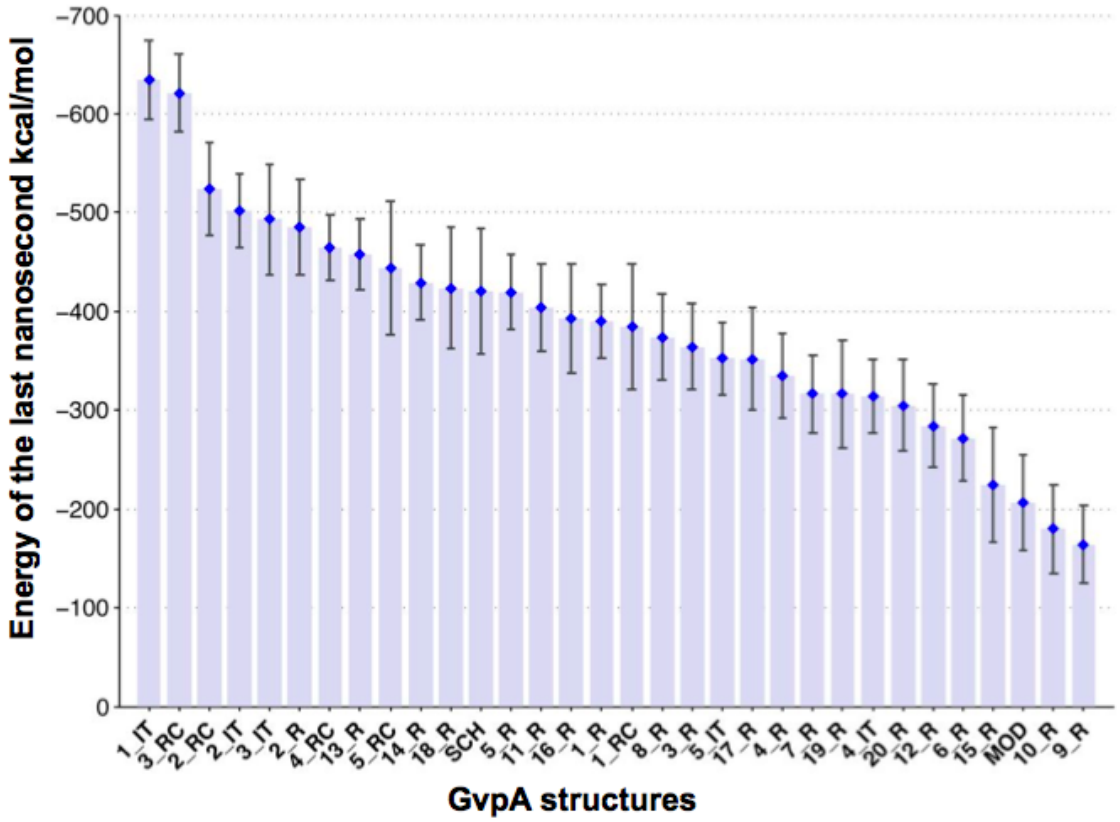

Figure 3.2: GvpA structures ranked according to the last nanosecond of the ensemble average values of the MM-PBSA energy. The y-axis values are reversed for better visualization. The vertical bars show the average energies and the error bars show the standard deviation from the mean, (IT stands for I-TASSER structures, RC stands for Rosetta cluster structures, R for Rosetta structures, SCH for the SCRATCH structure and MOD for the structure from MODELLER).

For example, structure 4_RC, ranked 7^{th} amongst all, did not exhibit most of the β-conformation and α-helix features as shown in Figure 3.6 (see also Table 3.1). The last structures in the ranking show a combination of random coils and helices, which support our conclusion that the native GvpA structure most probably complies with the predicted secondary structure folds depicted in the first row of Figure 3.3. We also point out that enzyme digestion experiments have showed that the C-terminus is

Table 3.1: Average MM-PBSA energy and standard deviation of the last nanosecond of the NPT molecular dynamics simulation for all GvpA structures predicted for *Halobacterium sp. NRC-1* (columns 3 and 4), and percentage of α-helices, β-sheets and coils (columns 5, 6, and 7). (IT stands for I-TASSER structures, RC stands for Rosetta cluster structures, R for Rosetta structures, SCH for the SCRATCH structure and MOD for the structure from MODELLER).

Rank	Structure ID	$\langle E \rangle$ [1] kcal/mol	σ [2] kcal/mol	β-Helices %	α-Sheets %	Coils %
1	1_IT	-634.87	66.01	39.5	26.3	21.1
2	3_RC	-621.20	51.06	39.5	26.3	14.5
3	2_RC	-524.33	48.09	43.4	26.3	13.2
4	2_IT	-502.34	48.56	39.5	22.4	25.0
5	3_IT	-493.09	52.72	39.5	31.6	17.1
6	2_R	-484.91	54.36	28.9	21.1	21.1
7	4_RC	-464.81	38.37	44.7	13.2	34.2
8	13_R	-457.51	52.31	26.3	13.2	30.3
9	5_RC	-444.01	54.52	38.2	15.8	30.3
10	14_R	-429.20	111.07	23.7	7.9	34.2
11	18_R	-423.70	53.53	34.2	13.2	25.0
12	SCH	-420.61	58.98	47.4	0	22.4
13	5_R	-419.68	39.28	50.0	11.8	22.4
14	11_R	-403.80	59.41	28.9	21.1	27.6
15	16_R	-392.46	54.23	36.8	23.7	36.8
16	1_R	-389.91	38.39	36.8	15.8	34.2
17	1_RC	-384.24	55.02	44.7	21.1	17.1
18	8_R	-374.09	55.74	47.4	13.2	22.4
19	3_R	-364.03	50.85	35.5	18.4	26.3
20	5_IT	-352.17	44.35	42.1	26.3	22.4
21	17_R	-351.68	59.22	42.1	0	28.9
22	4_R	-334.44	58.07	32.9	23.7	14.5
23	7_R	-316.46	47.77	23.7	25.0	19.8
24	19_R	-316.27	54.28	31.6	15.8	22.4
25	4_IT	-314.67	52.08	39.5	21.1	34.2
26	20_R	-304.89	48.38	22.4	28.9	17.1
27	12_R	-284.19	60.04	14.5	28.9	27.6
28	6_R	-271.83	78.48	34.2	23.7	19.7
29	15_R	-223.77	81.72	34.2	0	30.3
30	MOD	-206.74	56.96	26.3	0	42.1
31	10_R	-179.56	62.97	30.3	11.8	32.9
32	9_R	-164.02	41.07	40.8	7.9	28.9

exposed to the exterior at least in some subunits of GvpA in Halobacterium vesicles, which is also in agreement with our predicted structure, showing an exposed alanine C-terminus.

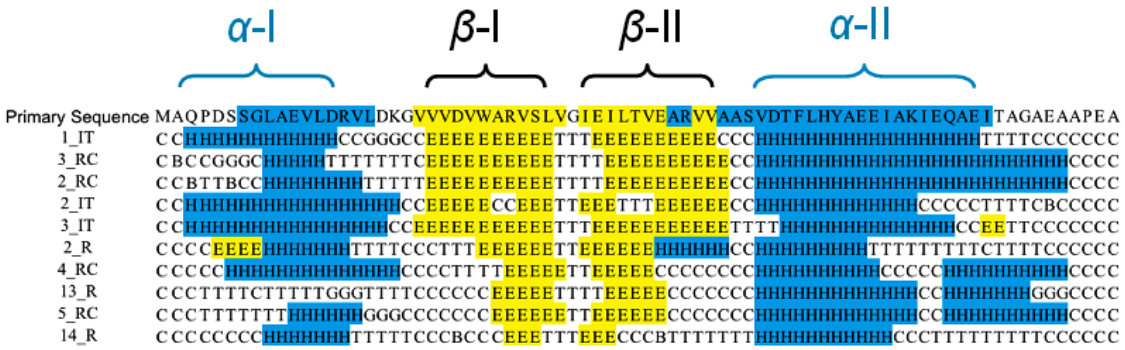

Figure 3.3: (First row) Primary sequence of GvpA from *Halobacterium sp. NRC-1* colored according to the secondary structure prediction consensus amongst the different algorithms described in the text; (rows 2-11) position-specific secondary structure for the top ten ranked structures as per Figure 3.2 and Table 3.1. "H" stands for α-helix (positions colored in blue), "E" stands for extended β-sheet (positions colored in yellow), "B" stands for isolated bridge, "C" stands for coil, "G" stands for 3-10 helix, and "T" stands for turn. The two part names on the left define (i) the rank of each structure among its family of decoys and (ii) the software used to predict this structure. For example, "1_IT" designates the top structure predicted with I-TASSER, "3_RC" means the third ranked structure in the center of the Rosetta cluster. The four secondary structure regions, α-I, β-I, β-II and α-II, are also indicated for the first row.

Another interesting observation is the amphiphilic nature of the top predicted structure, which, as shown in Figure 3.7, exhibits a highly polar face opposite to a highly nonpolar face, supporting the feasibility of the hypothesis that the inner

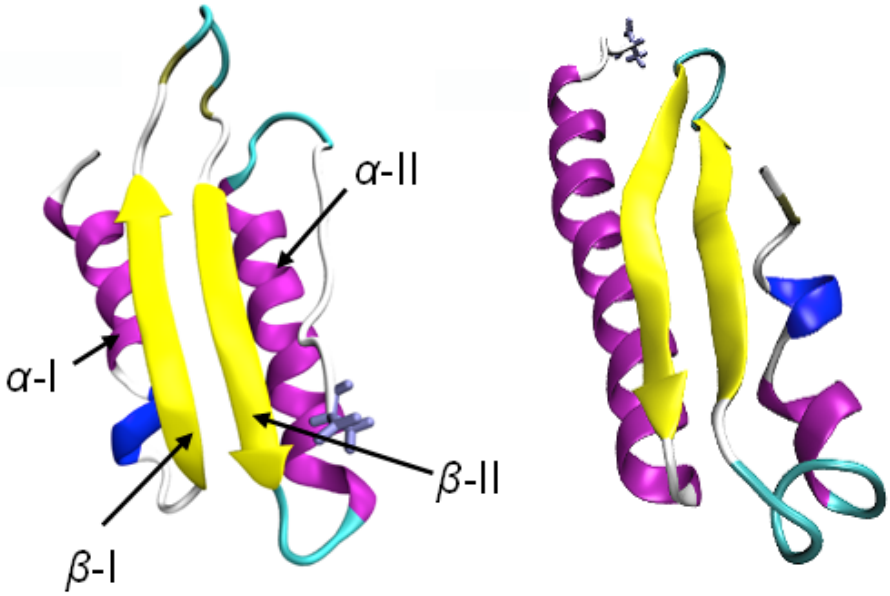

(a) (b)

Figure 3.4: Cartoon drawing representation of the top two structures according to the MM-PBSA ranking. (a) 1_IT structure; (b) 3_RC structure. β-sheets are shown in yellow, α-helices in purple and the C-terminus residue in ice blue. The helical regions and β strands are named α-I, β-I, β-II and α-II according to their position in the sequence with respect to the N-terminus.

surface of the vesicle is hydrophobic and the outer surface is hydrophilic [19]. While this result is promising, however, it must be treated as preliminary for two reasons. First, we did not observe the same behavior in lower-ranked structures. For example, the separation of polar and non-polar groups for the second ranked structure, 3_RC (results not shown), was not as sharp as shown in Figure 3.7 for structure 1_IT. Second, the amphiphilic nature of the vesicle wall cannot be explained through the properties of isolated molecules alone.

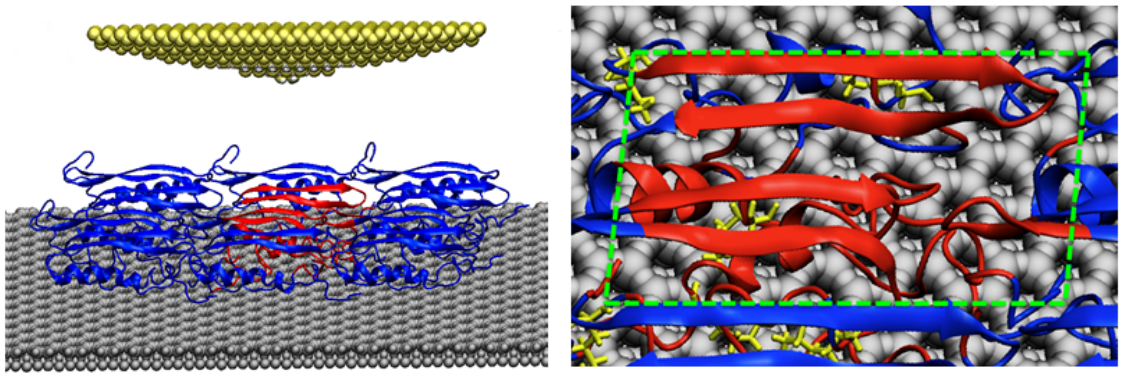

(a) (b)

Figure 3.5: Molecular dynamics model used in the AFM simulations. (a) Side view (note that the AFM probe is shown with a different tilt angle than the sample such that its apex is visible); (b) top view of the unit cell (depicted in red with lysine residues collared yellow for easier visualization). Note that the α-helix content of the GvpA molecules in the unit cell differs from that of the molecules on the edges of the model due to forcing the β-sheets in the unit cell to interact as proposed in [87]

We also compared our top ranked structure 1_IT (76 amino acids) with the model proposed by Strunk et al. [51] (78 amino acids). Despite belonging to different organisms, the two sequences possess 93% identity, differing primarily in that positions A2, V29 and I66 in our sequence are replaced with V2, I29 and L66 in the sequence analyzed by Strunk et al. [51]. One should not anticipate that these substitutions would alter the structure significantly since they preserve the hydrophobic nature of the respective sites. Indeed both structures are very similar with the model of Strunk et al. model having $\sim$23% β-sheet content and $\sim$39% α-helix compared to $\sim$26% and $\sim$40%, respectively, in our model. The highest similarity occurs at the conserved region where the β-I and β-II segments are located, with both models

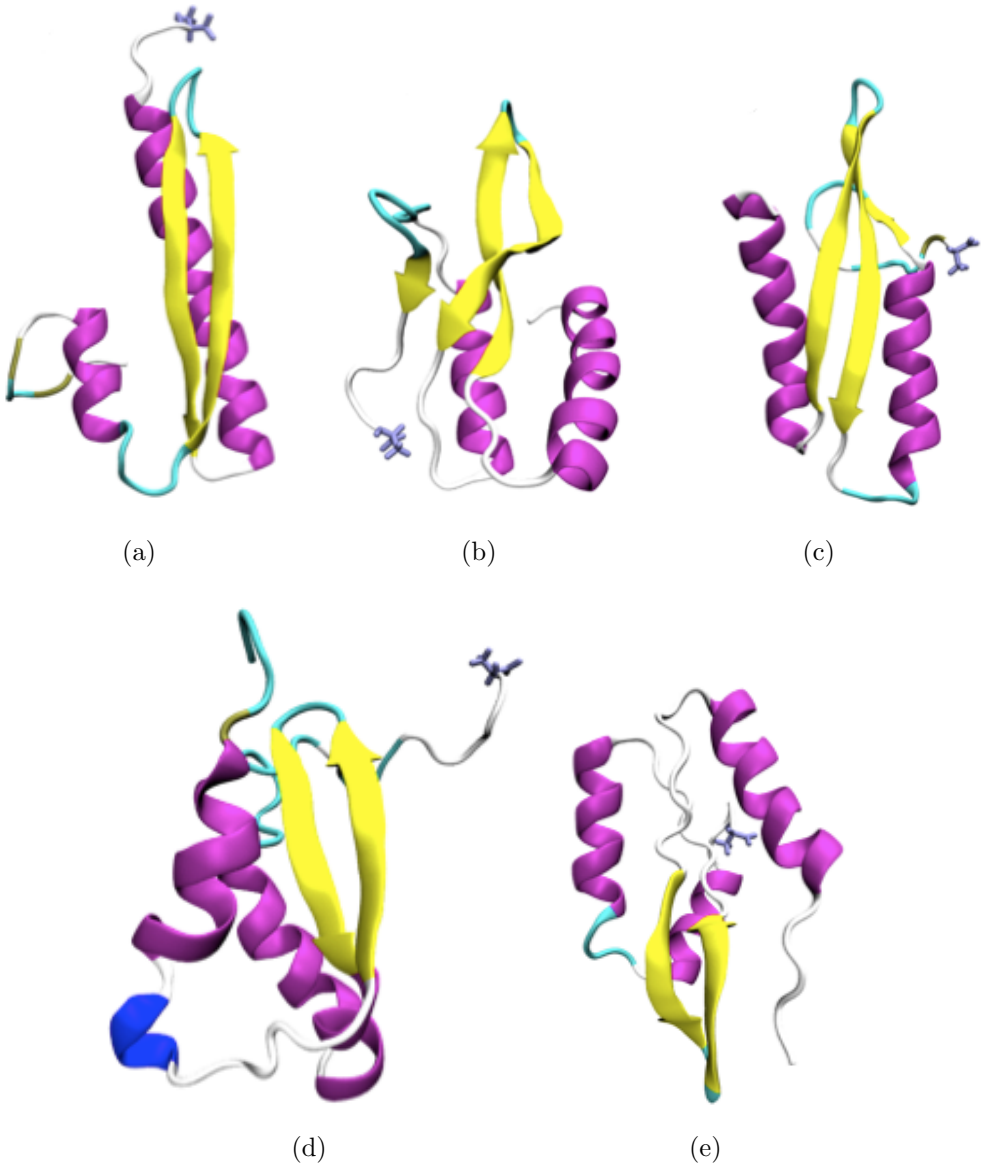

(a) (b) (c)

(d) (e)

Figure 3.6: Structures ranked 3^{rd} down to 7^{th}. (a) 2_RC; (b) 2_IT; (c) 3_IT; (d) 2_R; (e) 4_RC. β-sheets are shown in yellow, α-helices in purple and the C-terminus residue in ice blue.

having the exact β-turn at V32-I34. The difference in β-sheet content is related to the different in sequence length. The models differ slightly in the α regions, where the model of Strunk et al. [51] has a smaller helix and a more coiled N-terminus.

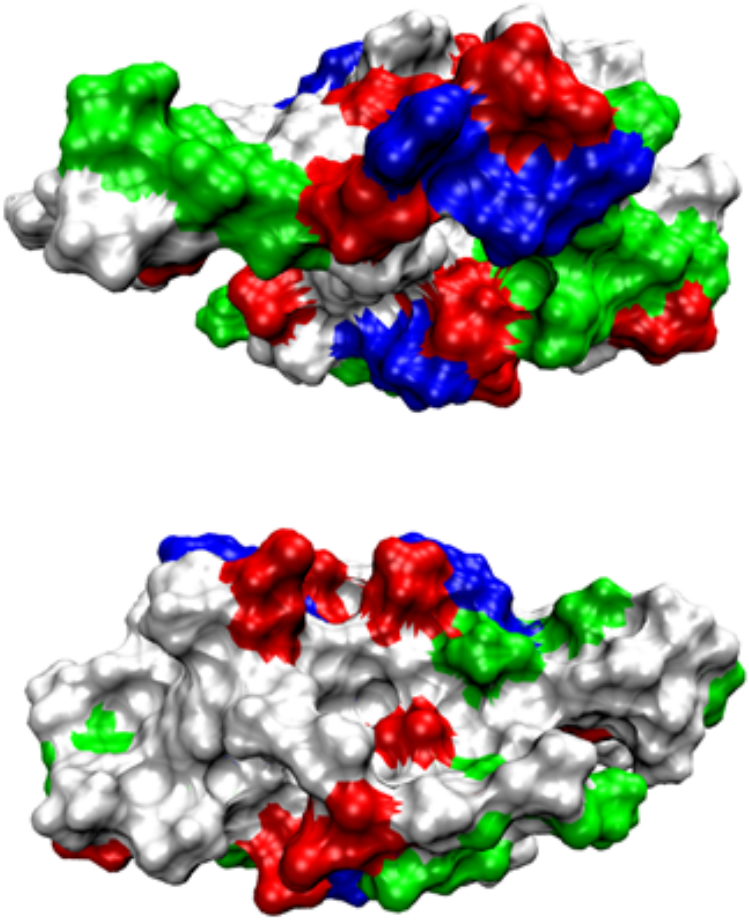

Figure 3.7: Two opposite surface views of structure 1_IT showing the distribution of non-polar and polar groups. Non-polar groups are colored white, polar non-charged groups are colored green, positively charged groups are colored blue, and negatively charged groups are colored red. The polarity and net charge of each residue was determined using VMD software [86], based on the force field atomic charges [73].

Furthermore, we note that the homology among the GvpA synthesized in six different organisms has previously been shown to be high [52], suggesting that similar structures can be expected in all cases. An alignment between GvpA from Halobacterium sp. NRC-1 and both cyanobacterium Anabaena flos-aquae and Calothrix sp. PCC 7601 performed using Needleman's algorithm [95, 96] is shown in Figures 3.8a

and 3.8b, respectively. The alignments aim to show the similarity amongst the GvpA sequences in the three organisms. The GvpA sequence from Halobacterium sp. NRC-1 has sequence identity of 51.9% and 50%, and sequence similarity of 65.8% and 64.1% with the GvpA sequences from Anabaena flos-aquae and Calothrix, respectively, as shown in Figure 3.8. Thus, as a simple verification, we attempted to predict the GvpA tertiary structure synthesized by *Anabaena flos aquae* and *Calothrix sp. PCC 7601* using the Rosetta suite 2.3 and I-TASSER server without further relaxation or equilibration. The top two clusters of the generated decoys from Rosetta are shown in Figure 3.6 and exhibit similar features to the 1_IT and 3_RC structures. Additionally, the 1_IT structure was aligned with the prediction for GvpA from *Calothrix sp. PCC 7601* and *Anabaena flos aquae* for visual inspection, as shown in Figure 3.9. In spite of comparing the raw structures predicted for the two without any refinement with respect to the 1_IT structure, the similarity between the three structures is evident. It is worth noting that the similarity between the tertiary structures is striking despite being only ∼50% homologous, and despite the fact that they were predicted using different techniques and algorithms.

Although, the homology of GvpA sequences of different organisms has been previously studied by Walker et al. [52] and Griffiths et al. [97], we performed a quantitative analysis to specifically evaluate the homology of the GvpA sequence from Halobacterium sp. NRC-1 with respect to that of other organisms, in order to assess the extent to which our structure prediction results can be generalized. Using BLASTP [68] with the scoring matrix BLOSUM62 we detected 65 sequences

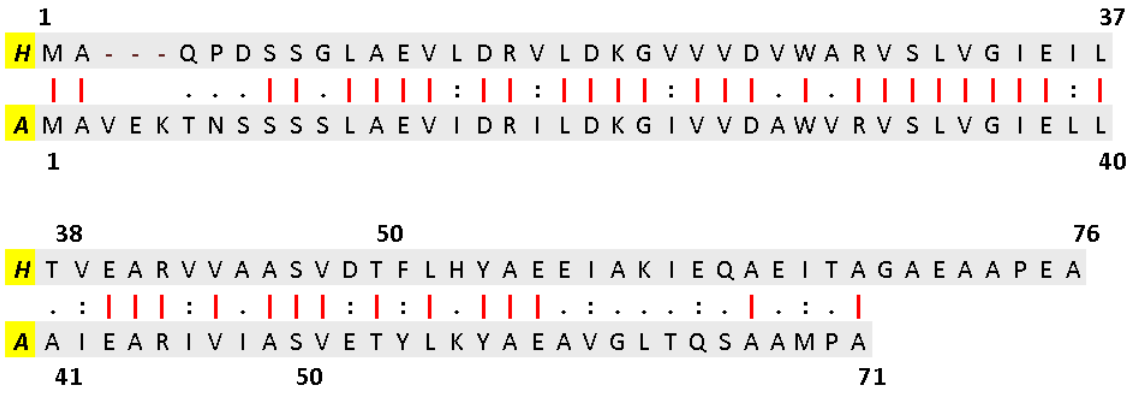

(a)

(b)

Figure 3.8: Alignment of the GvpA protein from three different organisms, halobacteria *Halobium sp. NRC-1* against cyanobacterium Anabaena *flos aquae* (a) and against *Calothrix PCC 7601* (b). (H in the yellow highlighted region stands for halobacteria *Halobium sp. NRC-1* GvpA, A for Anabaena *flos aquae* GvpA, and C for Calothrix GvpA. The red vertical lines "|" show conserved residues, the black colon ":" shows high similarity and the black dot "." indicates low similarity.)

from different strains with significant similarity to the GvpA from *Halobacterium sp. NRC-1*, having 35% sequence identity for the least homologous case, with more than 86% of the detected sequences having more than 50% sequence identity (see Appendix B for a list of these 65 sequences, along with their identity and similarity

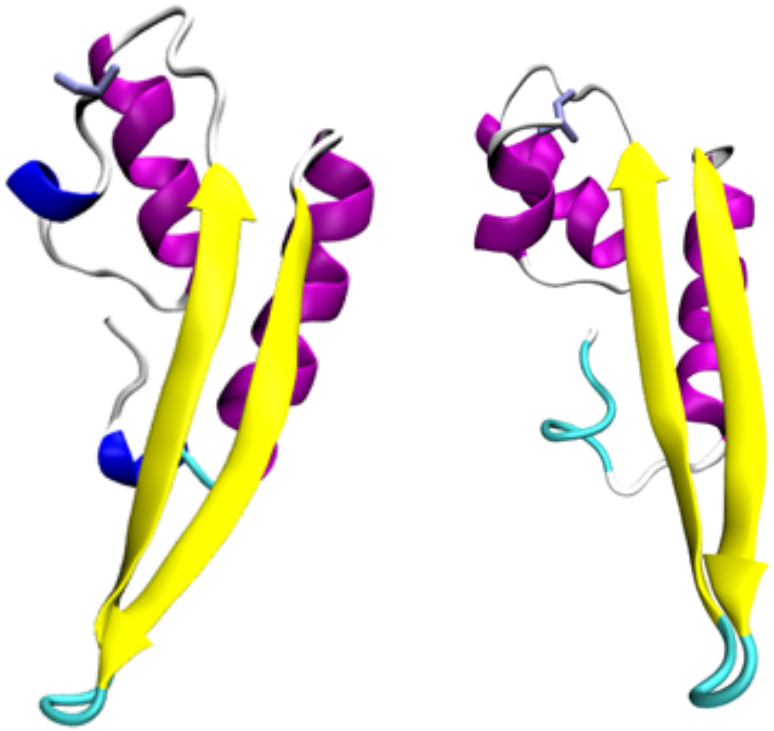

(a) (b)

Figure 3.9: Predicted GvpA structures for the organisms Calothrix (PCC 7601, 70 amino acids) (a) and cynobacterium Anabaena *flos-aquae* (71 amino acids) (b).

scores with respect to *Halobacterium sp. NRC-1*). Although accurate prediction of the tertiary structure of each of these sequences would require a full study similar to what we have presented here, the similarity between the structures predicted for GvpA from *Halobacterium sp. NRC-1* and the structures predicted for GvpA from *Calothrix sp. PCC 7601* and *Anabaena flos-aquae* suggests that most of the sequences identified in the BLASTP analysis should exhibit similar features to those of the structure shown in Figure 3.6.

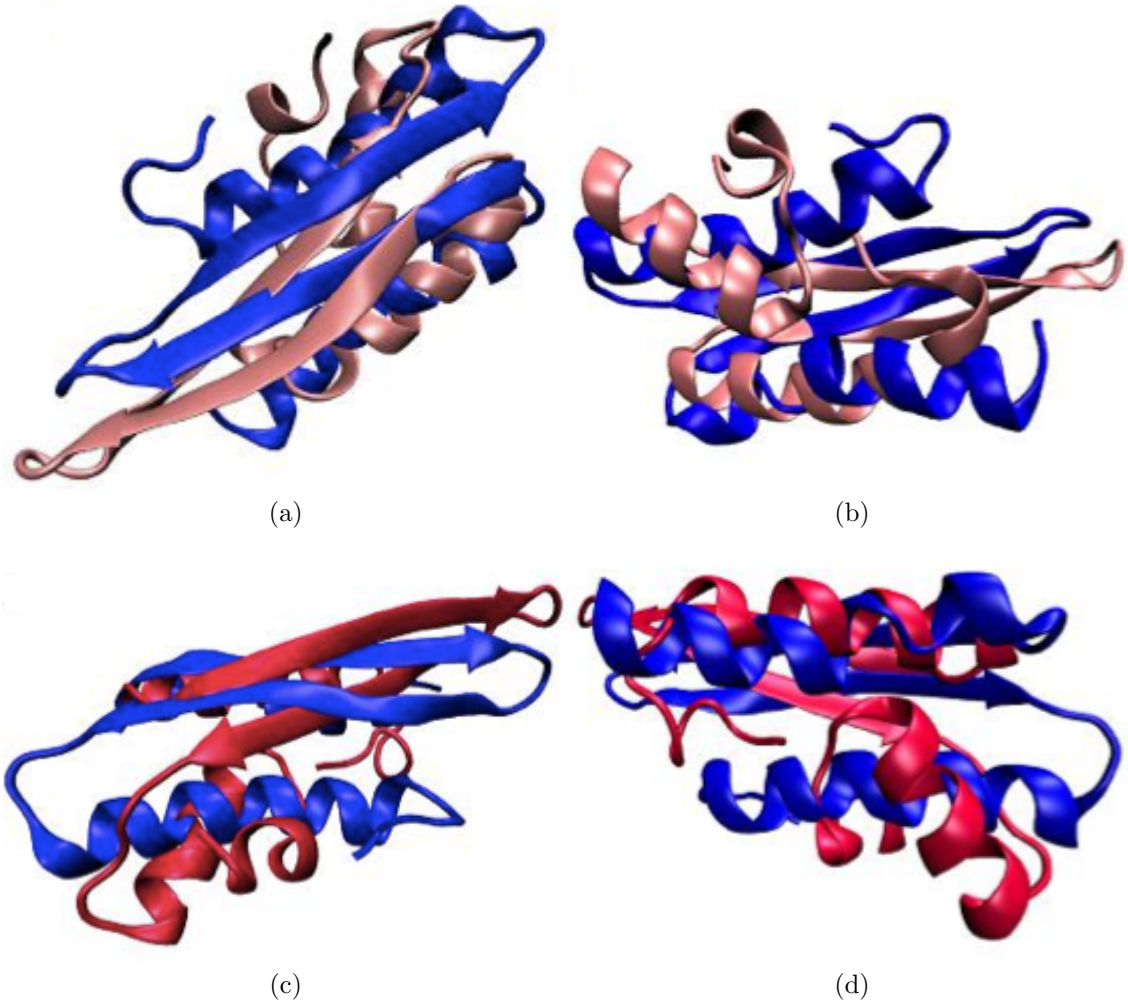

(a) (b)

(c) (d)

Figure 3.10: Predicted GvpA structures from the organisms Calothrix (PCC 7601, 70 amino acids) (a) & (b) and cynobacterium Anabaena flos-aquae (71 amino acids) (c) & (d) aligned with the 1_IT backbone for visual inspection. The 1_IT structure is shown in blue in all alignments. In (a) & (b), Calothrix is shown in pink. In (c) & (d) Anabanea flos-aquae is shown in red. Two views are presented for each alignment to illustrate the similarity in the α-helix and β-sheet regions. The structures were aligned using the "MultiSeq" plugin in VMD software [86].

Docking of GvpA units and their orientation within the vesicle membrane

According to the AFM images of Anabaena flos-aquae vesicles reported by McMaster and Walsby [12] (see Figure 3.11), the exposed structural features of GvpA

should exhibit relatively high contrast. Their images show regular elongated elements that form an angle of 36° with respect the vesicle axis. The measured distance between these elements was ∼4.57 nm, which is close to the 4.5 nm rib-to-rib spacing measured by X-ray diffraction [9]. If β-sheets were indeed exposed to the solvent (McMaster and Walsby imaged the outside surface of collapsed vesicles), they would need to be arranged in a similar pattern to what is observed in the AFM images. Since the infrared spectroscopy results reported in ([18]) predict anti-parallel β-sheet arrangement of dissimilar GvpA units, the exposed β-sheets would be required to closely interact with one another, such that the helices would be buried in the inside of the vesicle. However, this would disagree with both the MALDI-TOF work of Belenky et al. [98] and the solid-state NMR work of Sivertsen et al. [18], which suggested that the termini should be exposed (see Figure 3.11). In the latter work solvent accessibility was probed by deuterium (^2H_2O) exchange rates, where the three Lysine side chains in Anabaena flos-aque were found to be exposed to solvent. There are 2 Lysine residues in Halobacteria that match those probed in Anabaena, and they have the same location towards the ends of the helices, closer to the termini, suggesting that the helices have to be on the outside of the vesicle. Thus it is not possible to reconcile all available pieces of information for a structure in which the β-sheets are exposed to the solvent. Alternatively, one could propose that both the termini and β-sheets are exposed, but in this case the interactions of the β-sheets with one another would be hindered. Furthermore, inspection of the AFM images of McMaster and Walsby (Figure 10 ([12])) suggests a repeat pattern in the surface features rather than an alternating one, which is not compatible with

an anti-parallel β-sheet arrangement. Our simulated AFM image with the β-sheets towards the surface (Figure 3.11b) showed very little contrast and did not exhibit any features that had a strong resemblance to the images of McMaster and Walsby ([12]). In particular, they did not predict a clear tilt of the structural features with respect to the vesicle axis.

In contrast, although our simulated AFM image with exposed α-helices (Figure 3.11b) did not exactly match the result of McMaster and Walsby [12], it depicted structural features having a similar tilt angle magnitude with respect to the β-sheets axes, suggesting that the features imaged by McMaster and Walsby with AFM [12] may have been misinterpreted as the β-sheets corresponding to the second reflections that formed a 36° angle with respect to the vesicle axes in the work of Blaurock and Walsby [9]. We believe that the features in the AFM images represent α-helices, which in our model have a tilt angle with respect to the ribs of the membrane that is similar to that of the β-sheets (see Figure 3.11). There are number of reasons for the differences between the simulated and experimental images. First, the GvpA involved corresponds to two different organisms, which can have different size and orientation of α-helices with respect to the β-sheets (see Figure 3.11), especially upon docking. Second, the exact docking configuration is unknown. Assuming the incorrect docking configuration can have a significant effect, as illustrated by the differences in the helices of the docked molecules shown in Figure 3.11 (the helices of the molecules docked to only one unit differ from those of the molecules docked to two units). Third, it is not possible to model the exact probe-sample interactions

that took place during the experimental AFM imaging process. Specifically, the exact tip geometry, functionalization (silicon tips are covered with a layer of silicon oxide) and charge distribution, as well as the sample moisture distribution are all unknown. Finally, the simulated images have lower resolution than the experimental images. Nonetheless, close inspection of the actual features (Figure 3.11) shows that there is similarity between the experimental and simulation results, which supports the conclusion that the exposed surface contains α-helices. Furthermore, closely inspecting the β-strands of each subunit, it is clear that their backbones are not perfectly aligned, but rather they are shifted two residues every two subunits. This shift in subunits could be explained by the transmission electron microscopy results of the frozen-hydrated wild type gas vesicles images by Offner et al. [99], which showed that the walls of the gas vesicle consists of a low pitch helical structure instead of a stack of perfectly parallel hoops.

The above discussion discards the previous hypothesis that the vesicle membrane could be formed by only β-sheets [22] (this hypothesis is also discarded by Sivertsen et al. [87]). This is supported by the experimentally measured membrane thickness of 2.8-4 nm [17], which is greater than the thickness of a single β-sheet. Instead, this information, along with the structure prediction data, suggests that the sheets and helices must be folded onto one another. This is also in agreement with the X-ray data [9] and the experimental AFM images ([12]), which show a separation of 4.6 nm between vesicle rib centerlines, as shown in Figure 3.11, which is similar to the length of the β-strands in our predicted IT_1 structure of the GvpA unit. Finally,

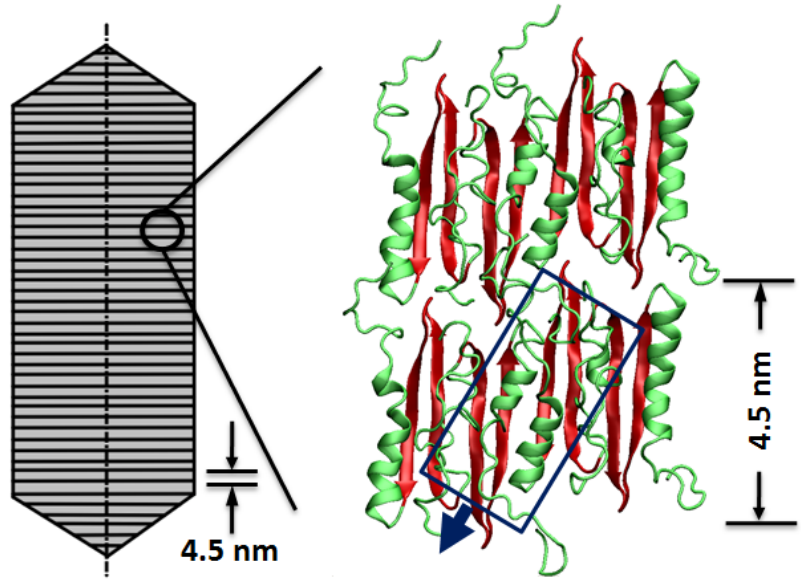

(a)

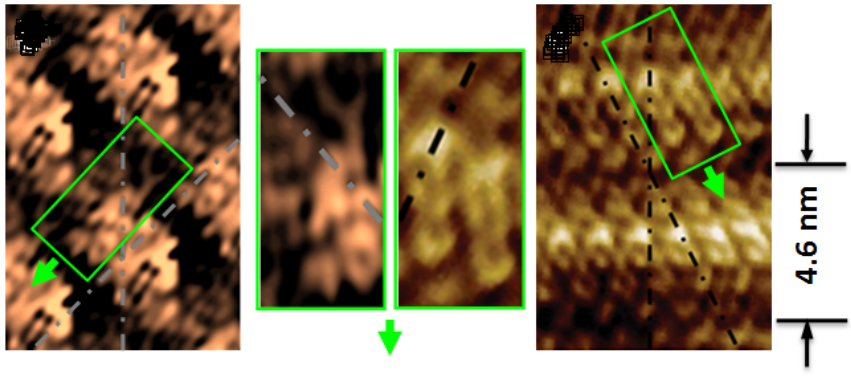

(b)

Figure 3.11: (a) Proposed orientation of GvpA units within the vesicle membrane; (b) simulated AFM image of the α-helix side of the dimer (left) and experimental AFM results of McMaster and Walsby for Anabaena flos-aquae [12] (reproduced with permission) (right). The rectangles and arrows in (a) and (b), and the dashed lines in (b) are provided for orientation purposes. The vertical dashed lines in (b) are aligned with the long vesicle axis in (a), while the tilted dashed lines are aligned with the observed features.

this agrees with the charge distribution and hydrophobicity characteristics of the docked structures used for simulating the AFM imaging process, which possessed

two surfaces of distinct hydrophobicity and charge distribution similar to Figure 3.7. The α-helices side has net negatively charged residues (colored red in Figure 3.7) and more polar residues (colored green), while the β-sheets side showed a more hydrophobic surface with non-polar residues (colored white), with less negatively charged residues and almost equal number of positively charged residues.

In light of the above discussion, we propose that (see Figure 3.11), (a) the ribs depicted by electron microscopy and confirmed by the X-ray experiments [9] result from the β-sheets interacting side by side, (b) the strands of β-sheets of the interacting subunits do exhibit a shift of two residues every two subunits, which explains the formation of the helix-like ribs instead of stack of hoops; and (c) the two helical regions flanking the conserved intermediate β-sheet region are responsible for the observed structural features forming an angle of $35 - 36^{\circ}$ with respect to the vesicle axis in the AFM images.

The deletion and point mutation experiments done by Strunk et al. [51] support not only their dimer model, but also agree with ours. Their deletion experiments show the unimportant role the C-terminus plays in the vesicle integrity, such that deletion of up to 7 amino acids (A70-A76) does not alter the production of gas vesicles. On the other hand, transformants with 11 amino acids deleted from the C-terminus lacked gas vesicles [51]. This suggests that amino acids upstream of A70 are the key for the integrity of the vesicle structure. In particular, our model suggests that E65 plays an important role in subunit-subunit interactions by forming

salt-bridges with R15 from the adjacent GvpA molecule, as shown in Figure 3.12. Deletion of 11 amino acids (I66-A76) destabilizes this region and results in weakening the GvpA-GvpA interactions and hindering vesicle formation. This is in agreement with the point mutation experiments carried out by Strunk et al. [51] for residue R15. Mutants with R15, on helical region-I, replaced by either A15 or K15 did not lead to gas vesicle production. Similarly, in our model residue K60 stabilizes the helical region II by salt bridging with residue E56 located on the same helix, in addition to its interaction with residue E56 from the adjacent subunit (Figure 3.12). In the work of Strunk et al. [51] replacement of K60 with L60 yielded transformants with very small gas vesicles.

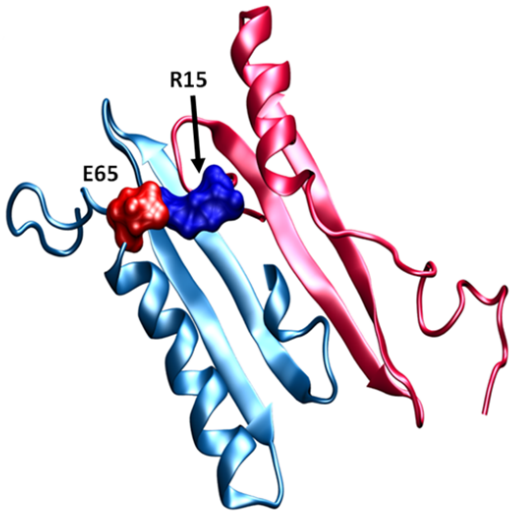

(a)

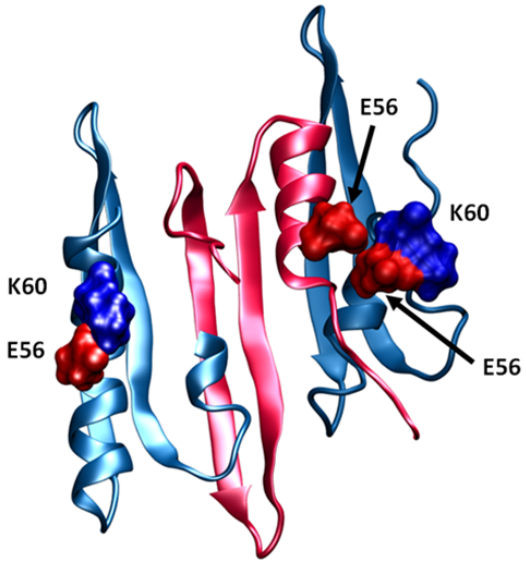

(b)

Figure 3.12: (a) Two GvpA subunits shown to depict the interactions between residue R15 (blue side chain) on one subunit and residue E65 (red side chain) on an adjacent subunit. The two subunits are shown in different colors and the N-termini are omitted for easier visualization of the interactions. (b) Three GvpA subunits showing the salt-bridge interaction between residues K60 and E56 on the same subunit and the adjacent one. GvpA is shown in "new cartoon" representation and the side chains in "surface" representation. E56 is colored red and K60 blue.

3.4 Conclusions and future work

A comprehensive study, using protein structure prediction and molecular simulation, has been conducted to elucidate the tertiary structure of GvpA, the 76-amino acid polypeptide comprising more than 90% of the gas vesicle membrane mass in Halobacterium sp. NRC-1. We have used state-of-the-art techniques in protein secondary and tertiary structure determination, which were implemented through multiple software packages and web servers, such as SCRATCH and MODELLER (homology modeling), I-TASSER (threading) and ROSETTA suite 3.2 (ab-initio modeling). The predicted structures were further refined through molecular dynamics equilibration with explicit solvent, followed by application of the MM-PBSA method, and ranked according to total energy. The highest ranked structures exhibited $\sim$40% α-helices and 26% β-conformations, in agreement with previous experimental data and with our own secondary structure predictions. Furthermore, the observed separation of polar and non-polar groups on the surface of the top structure was in agreement with the previously proposed hypothesis that the internal gas vesicle wall is hydrophobic, while the exterior is hydrophilic. In addition, the sequence identity analysis with GvpA sequences from various organisms and tertiary structure prediction for the GvpA synthesized by cyanobacterium Anabaena flos-aquae and Calothrix sp. PCC 7601 suggest that similar features can be expected be present in a large number of GvpA types. Our top ranked structure is highly homologous with the previous prediction of Strunk et al. [51]. The secondary struc-

ture content of both models is in exact agreement at the β-I , β-II and α-II regions, but our α-I region is shifted 4 positions upstream, such that a small coil region exists between α-I and β-I compared to a small β-turn in the model of Strunk et al. Although our predicted model is very similar to their top ranked structure, our docking approach yielded a more tightly packed assembly that is more consistent with a barrier between air and water at the vesicle interface. Finally, simulated atomic force microscopy images allowed us to reconcile our simulations with the available experimental data, such that a new hypothesis on the orientation of the GvpA unit within the vesicle and on the origin of the membrane structural features was proposed.

Chapter 4

Red Blood Cells and Hemolysis Processes

Motivation

Mortality rates due to cardiovascular diseases are the highest amongst all diseases in the U.S [100]. Therefore, nowadays more attention is drawn towards studying the causes of heart diseases, providing better solutions to enhance the quality of the treated patients and developing better bio-devices that can replace dysfunctional heart valves. The currently-available replacement valves are biological or mechanical, a schematic of each is shown in Figures 4.1a & 4.1b, respectively. The first type has less effect on the flow characteristics across the valve, however, it is not as reliable as mechanical valves. While the latter type, mechanical valves, is more reliable, it alters the flow field downstream of the valve. The change in the blood flow characteristics, either due to transitioning of the flow from laminar to turbulent or due to increasing the intensity of turbulence, is known to induce damage to the blood constituents [4]. Such damage known as *hemolysis*, has a significant effect on

the behavior of red blood cells and platelets [5]. Therefore, cardiovascular patients who have undergone heart valve replacement suffer from these risks, and are prone to thrombus, i.e., blood clotting, and have to consistently take de-coagulation therapy. Thus, improving the design of these prosthetic bio-devices demands understanding the behavior of blood components. In other words, it is necessary to understand how the blood micro-constituents are affected by implantation/application of these prosthetic devices. In addition, there is a need for mathematical frameworks that simulate this behavior to aid the development of better designs.

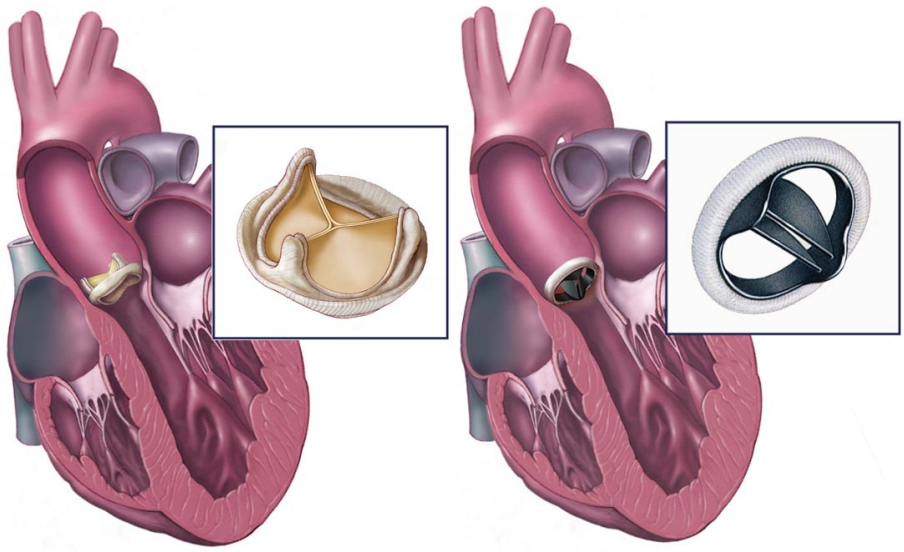

(a) Biological (b) Mechanical

Figure 4.1: Replacement aortic heart valves. Taken from (http://www.mayoclinic.org/heart-valve-surgery/types.html)

4.1 Background

4.1.1 Blood: components and properties

The main blood components are plasma, platelets, red blood cells (RBCs) and white blood cells (WBCs), as shown in Figure 4.2a. Plasma is the nutrients containing fluid, for example, electrolytes such as sodium, calcium, potassium, etc., and vital proteins such as albumin and immunoglobulins. Platelets are responsible for blood clotting. WBCs form the defense line of the body against infections and diseases. RBCs constitute about 45% of the blood volume and their main function is oxygen (O_2) delivery and carbon dioxide (CO_2) take up, to and from the body organs and tissues. Figure 4.2b shows the percentage of each blood component by volume.

4.1.2 Red blood cells

Mammalian red blood cells, known as erythrocytes, are non-nucleated cells that develop in the bone marrow. They carry oxygen from the lungs to the body organs via blood in the circulatory system. Oxygen delivery is carried out with the help of the metalloprotein, *hemoglobin*, the major non-membrane protein constituent of RBCs; each hemoglobin molecule binds four O_2 molecules with its heme group. In addition to carrying O_2 from the lungs, it also exchanges it with CO_2 at tissues of low O_2 and high CO_2 concentrations. The normal life span of RBCs is 122 ± 23

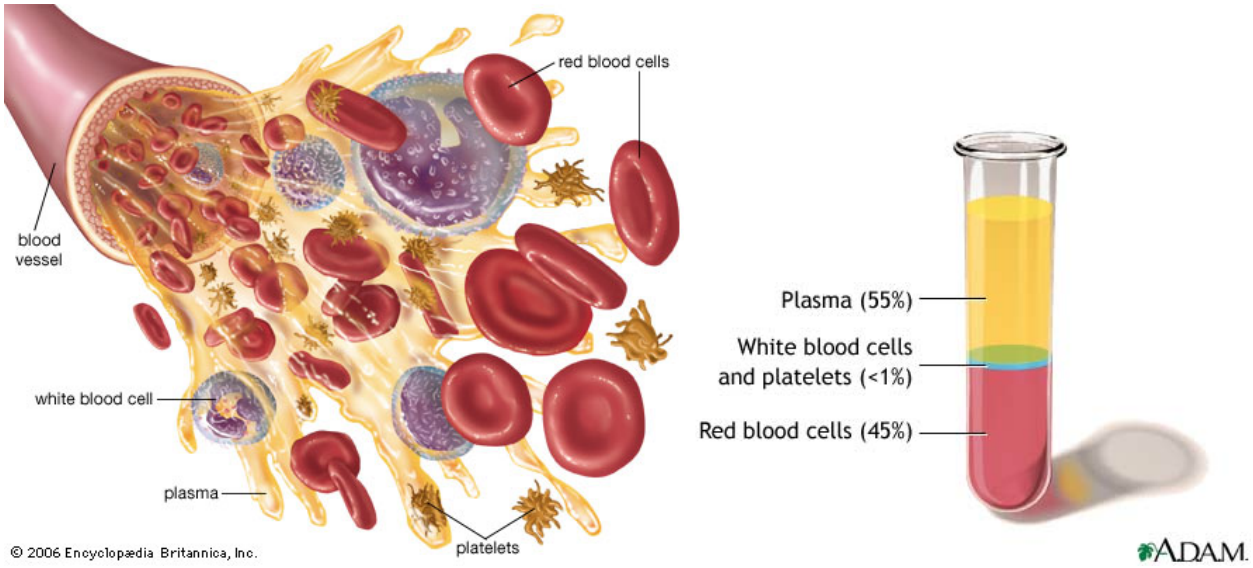

(a) (b)

Figure 4.2: Plasma, platelets, RBCs and WBCs are the main blood components. (a) A cartoon representation of blood components, taken from (http://homeworkteam71.wikispaces.com/Science+with+Mr.+Mullett). (b) Volume percentage of each blood component, taken from (http://mskrobinson.blogspot.com/2010_05_01_archive.html).

days; however, they can sometimes be damaged prematurely inside the blood vessels, i.e., intravascular, or outside the blood vessels, i.e., extravascular. For patients with heart valves replaced, the life span of RBCs drops to 103 ± 15 days for biological valves and even lower to 98.8 ± 23 days for mechanical valves.

As shown in figure (4.2a) RBCs assume a discoid (biconcave) shape under physiological conditions. However, other forms have been observed. These different states are systematically produced under a known set of parameters (see figure 4.3) [101]. For example, anionic amphipaths, high salt, high pH, ATP depletion and cholesterol enrichment produce the so-called echinocyte, where the RBC shrinks and star-like protrusions occur, producing sea-star shape cells. Under more severe conditions, irreversible buds and spicules take place, leaving behind a spherical like shape with extracellular vesicles (the spheroechinocyte). Under opposite polarity of loading, cationic amphipaths, low salt and low pH, cholesterol depletion induces a concave shape called stomatocyte. More severe conditions result in a spherical shape.

There are different RBC related diseases, for example, hereditary spherocytosis (HS), malaria, sickle-cell disease and others that affect the deformation characteristics of RBCs. Some of these diseases result in excessive RBC breakdown (hemolysis) leading to the loss of hemoglobin, where malfunctioning RBCs are left behind. This forces the heart to work harder to compensate for the oxygen deficiency in the circulatory system. While some of these diseases are genetically-related, oth-

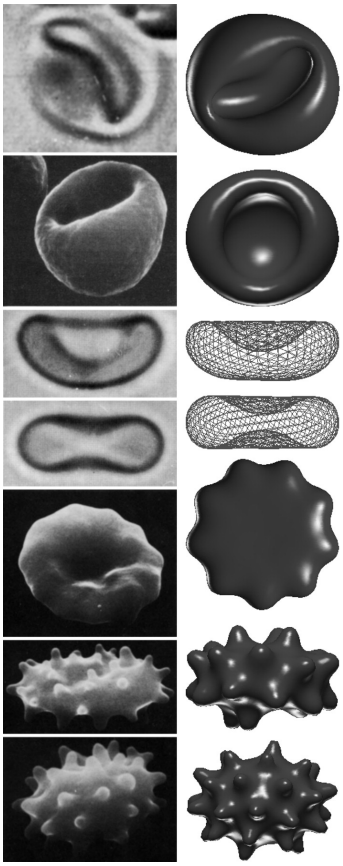

Figure 4.3: RBC states under different physiological conditions. From top to bottom, stomatocyte III, II and I, discocyte, echinocyte, I, II and III. Figure taken from ref [101].

ers are due to mechanical traumatization of blood, e.g., hemolytic anemia, which might be induced by the implantation of prosthetic heart valves in the human body or during dialysis for patients with chronic kidney failure. Since the latter is caused by flawed mechanical design, it can be partially eliminated by enhancing the shape and operation of heart valves and blood pumps [5].

RBCs' relatively simple structure provides a perfect platform for experimental, analytical and computational studies. Their simplicity enables analytical frameworks in which the dynamics and response of the RBCs can be accurately modeled. To date several models have been developed to mimic RBCs' behavior in many experiments, e.g. Discher et al. [102] simulated micropippette aspiration of

RBC experiments using Monte Carlo techniques, Dao et al. [103] formulated a finite element analysis of RBCs using a hyperelastic model and other different techniques were employed towards developing a rigorous model. These models will be discussed in section 4.2.

4.1.3 Hemolysis

Mechanical hemolysis is the damage to the RBCs under the influence of turbulent shear stresses that occur downstream of the mechanical valves or through the blood pumps. This turbulence might also occur due leakage in biological valves after structural deterioration, or due to paravalvular leak [104], where turbulent flows develop within the sewing ring and the native ring, shown in figure (4.4). The relation between turbulence and RBC damage can be explained by the energy cascades concept [105]. When turbulent eddies take place in the flow, the large scale, unstable, eddies breakdown and transfer their energy to the smaller scale eddies. Smaller eddies expand in number to fill the space that was occupied by the larger ones. At the small scale eddies, the viscous effects become more important and the smallest eddy has a characteristic length scale, known as Kolmogorov scale [105, 106]. If the smallest eddy length scale is on the order of the RBC size then the membrane exhibits both viscous and turbulent shear stresses as shown in equation (4.1), according to Boussinesq:

$$\tau_{turbulent} = (\mu_d + \eta)\frac{du}{dz} \tag{4.1}$$

where μ_d is the dynamic viscosity, η is the eddy viscosity, u is the flow velocity and z is the normal direction to the flow.

However, if the Kolmogorov scale is larger than the RBC size, then the RBC membrane only "feels" the viscous stresses due to the relative velocity between the RBC motion and the local flow velocity. In this case, the RBC is evicted from the turbulence regime, and what is known as shear thinning or Fahraeus effect is observed.

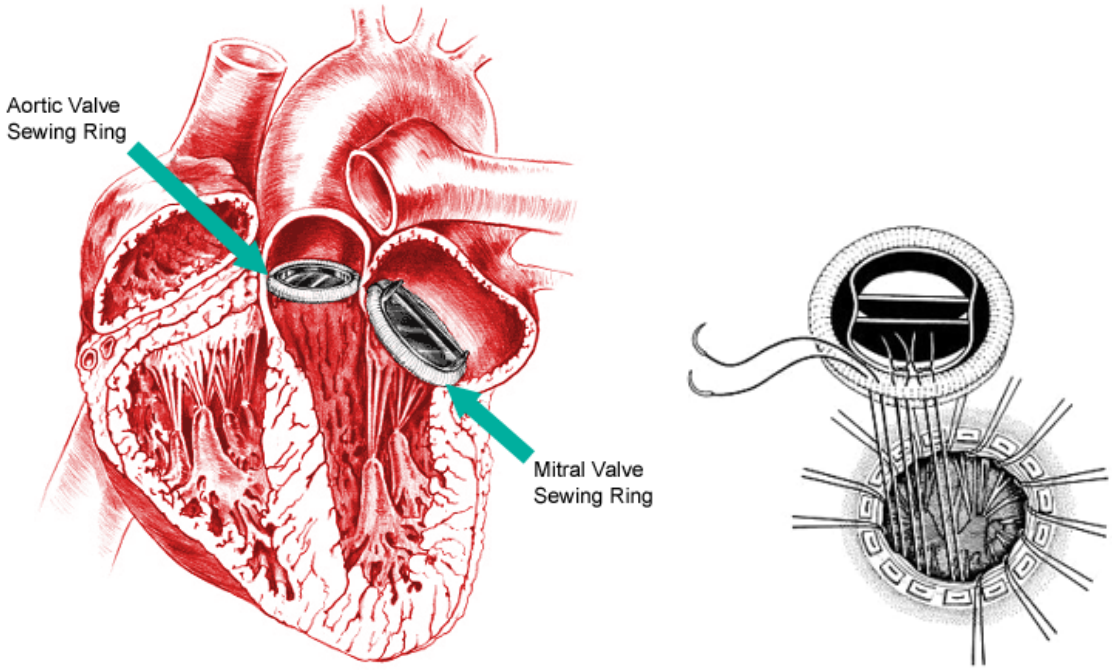

(a) (b)

Figure 4.4: (a) Location of paravalvular leak in aortic and mitral valves. Taken from (http://www.sjm.com/corporate/silzone/paravalvular-leak.aspx) (b) The sewing ring (top) and native ring (bottom) are shown for a mitral valve [107].

Hemolysis is quantified clinically by a standard test. A loop experimental setup, shown in figure (4.5), is used to measure it in blood pumps. The normalized

index of hemolysis, NIH [108], shown in equation (4.2) is used to express the amount of damage.

$$NIH(g/100L) = \Delta pfHb \times V \times \frac{100 - Hct}{100} \times \frac{100}{Q \times T}, \tag{4.2}$$

where $\Delta pfHb$ is the increase in plasma free hemoglobin concentration (amount of hemoglobin released from red blood cells into the plasma), Hct is the hematocrit of the blood (45% for healthy persons). Q is the flow rate (L/min), V is the circuit volume (L) and T is the sampling interval.

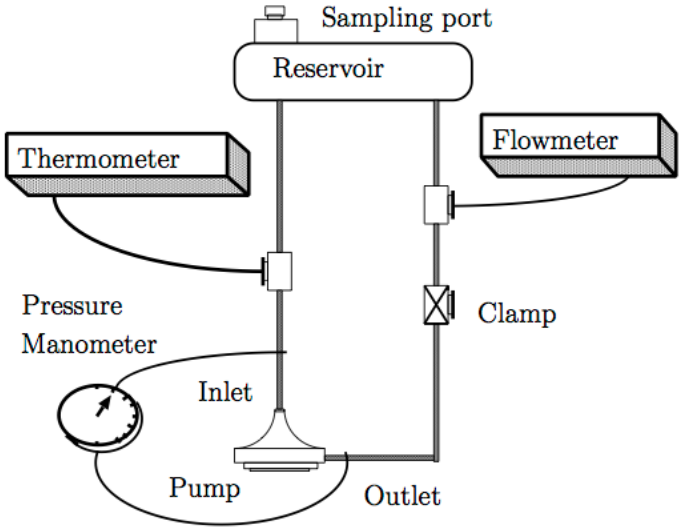

Figure 4.5: ASTM standard test-loop setup for measuring hemolysis in blood pumps [109].

Since hemolysis is a multi-scale process, it deals with two disparate spatio-temporal scales; on the RBC level, a mesoscopic approach should be employed, where neither the molecular nor the continuum scales are *appropriate*, to capture

the dynamics and kinematics behavior of the RBCs. On the blood flow rheology level, where the flow characteristics are the main interest and how they are affected by the collective behavior of the blood components, i.e., RBCs aggregation and dissociation, a continuum scale study will be more appropriate.

To date most of the hemolysis studies focus on the collective blood behavior. In fact, the widely used models, e.g., Giersiepen et al. [110], to detect hemolysis rely on steady one-dimensional analysis of the flow. In other words, they neglect the three dimensional nature of the flow and assume a single value for the shear stresses. Also, they only look at the steady state flows, ignoring the real flow conditions of blood in the circulatory system and the effect of loading history. The currently-available hemolysis models, also known as blood-damage models, will be discussed in detail in section 4.2.7.

In light of the above introduction, the next several sections will lay the foundation for the implemented work. Section 4.2 summarizes the literature on previous models and experiments. Section 4.3 discusses the methods and techniques used. Section 4.4 shows the results and discussions. Finally, section 4.5 presents the concluding remarks.

4.2 Literature Review

4.2.1 Red blood cells: *in vitro*

The mechanical properties of living cells, generally, and RBCs, specifically, have been probed using various experimental techniques such as atomic force microscopy, micropipette aspiration, magnetic twisting cytometry, optical traps and substrate deformations. These techniques provided different levels of spatial and force sensitivities. They aided in exploring the response of living cells under various hydrodynamical and physiological conditions [111]. Figure 4.6 shows a schematic drawing of the different experimental techniques.

Although RBCs' architecture is the simplest amongst all cell types due to its fewer components, they are still very complex to be studied at the atomistic level. Therefore, introducing approximations and reduced representations, i.e., coarse grained models for the cell constituents, is inevitable so that the system becomes computationally feasible.

The structure of the RBCs has been an interesting subject. The shape and dimensions of the RBCs were first investigated experimentally by Evans et al. [112]; the average diameter of the human discoidal RBC shape is 7.82 μm (Figure 4.7a),

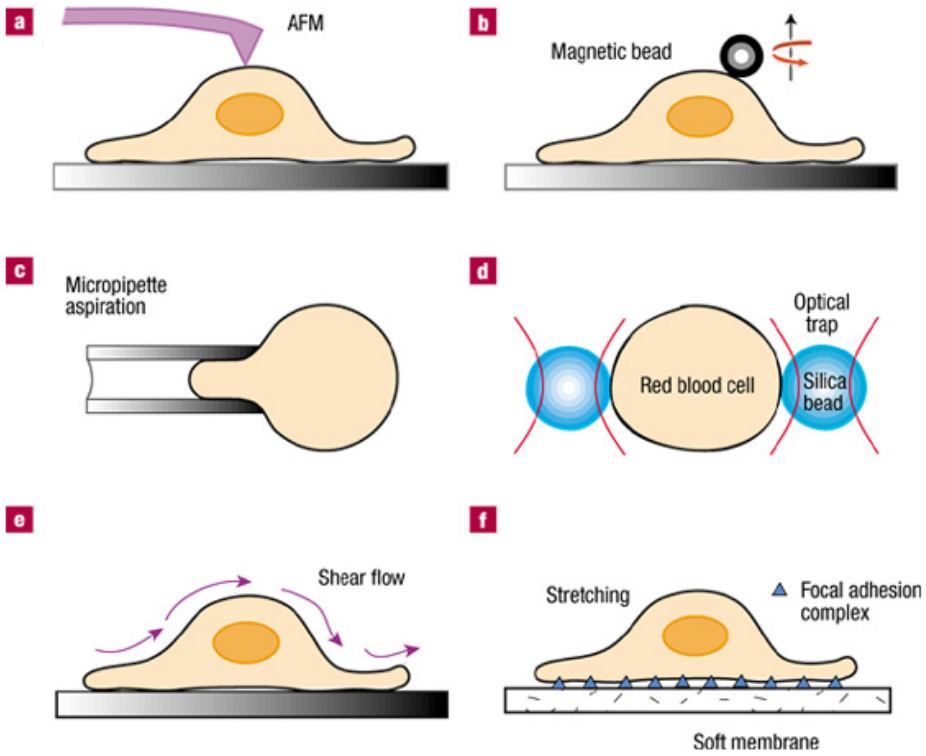

Figure 4.6: (a) Atomic force microscopy (AFM), (b) magnetic twisting cytometry (MTC), (c) micropipette aspiration (MA), (d) optical trapping (OT), (e) shear flow (f) and substrate stretching. The methods in a & b can probe cell components at a force resolution of 10^{-10} and 10^{-12} N, respectively. Techniques c & d can deform an entire cell at a force resolution of 10^{-10} and 10^{-11} N, respectively. Methods in e & f evaluate the behavior of a population of cells. Figure taken from [111].

which can be expressed analytically using equation (4.3), as shown in Figure 4.7b,

$$z = \pm D_o \sqrt{1 - \frac{4(x^2+y^2)}{D_o^2}} \left[a_o + a_1 \frac{x^2+y^2}{D_o^2} + a_2 \frac{(x^2+y^2)^2}{D_o^4} \right], \tag{4.3}$$

where $a_o = 0.0518$, $a_1 = 2.0026$, $a_2 = -4.491$ and D_o=7.82 μm is the average diameter. The above expression constructs a biconcave RBC shape with a surface area of 135 μm^2 and volume of 94 μm^3. The same set of parameters $(a_0, a_1, a_2) =$

$(1, 0, 0)$ will produce a spherical shape with a diameter D_o.

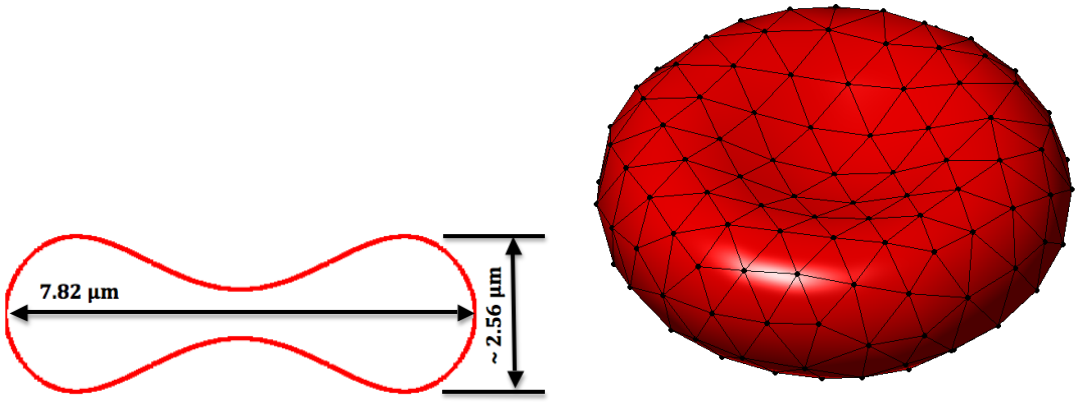

(a) (b)

Figure 4.7: (a) RBC cross-section and dimensions as determined experimentally [112]. (b) Discoidal RBC shape constructed from equation (4.3)

This chapter covers the research carried out thus far on RBCs experimentally and computationally. Over the last five decades, researchers have invested time and efforts to study RBC dynamics and response under different loading conditions. Various techniques were employed to characterize quantitatively the moduli of the cytoskeleton and lipid membrane, i.e., shear modulus μ and area compressibility modulus K. In addition, different models have been developed to predict the behavior of a single RBC, or a cluster of RBCs in blood flow [113, 114, 102, 115, 116, 117, 118].

4.2.2 Micropipette aspiration

Micropipette aspiration techniques have been employed extensively in cell studies, in particular RBCs, where the aspiration of living cells revealed information

about their elastic behavior. For RBCs it has allowed the observation of relaxation times for the spectrin network and recovery times from a deformed state to the original discocytic state. For example, Artmann et al. [119] studied the RBC recovery from enthinocyte to discocyte shape which was induced when the cells were held for 30 seconds by the micropipette and then released. Their experiments showed a recovery time of $\sim$ 10 minutes from enthinocyte I to discocyte shape, which was not changed under the effect of different temperatures, including 20.90 °C, 29.50 °C, and 37.40 °C.

Evans [120] studied the buckling of the RBC membrane under aspiration to evaluate its bending rigidity. He calculated the bending or curvature elastic modulus to be 1.8×10^{-12} dyn-cm. Engström and Meiselman [121] used a short duration ($\sim$ 3 s) peak loading to reproduce realistic values for the area dilation modulus K, for which they obtained a value of 215 dym/cm (0.215 N/m).

Utilizing the same technique, Discher et al. [122] used fluorescence-imaging to investigate the cytoskeleton deformation and the response of the different RBC membrane constituents over a wide range of time scales, i.e., seconds to 30 minutes. Changes of 40% up to 250% in the spectrin network area were detected by Discher et al. [122] without cell lysis. This is an interesting result because cell rupture occurs after only 6% increase in the membrane area.

The above mentioned experiments, revealed significant information about the macroscopic properties of the RBC membrane and spectrin network. These experimental characterizations are useful for the development and parameterization of accurate analytical models. They also illustrate how the loading time scales affect the behavior of the cells. Therefore, the assumptions made in the development of analytical models should not only account for the magnitude of the loads, but also for possible phase transitions corresponding to rate of loading.

4.2.3 Optical tweezers

As mentioned above, optical tweezers (OT), also called optical traps, is one of the techniques previously used to probe living cell mechanical properties. Dao et al. [103] and Lim et al. [123] investigated large deformation of individual RBC using optically trapped silica beads, as shown in Figure 4.8a. Two silica beads were attached, nonspecifically, to a RBC and trapped by two optical tweezers. Then the trapped cell was stretched by pulling one trap and keeping the second one stationary, as illustrated in Figure (4.8b). The application of forces in the range of 0-340 pN, using OT, provided insight into the elasticity of the cytoskeleton and how much elongation the spectrin network can withstand, which agrees with what Discher et al.'s [122] fluorescence studies found. While RBCs were stretched under the influence of an increasing force, the axial and transverse diameters, corresponding to the direction of the force application and perpendicular to it, were recorded. The behavior of the RBCs depicted the nonlinearity of the protein network, which also

justifies the need for a hyperelastic model in the finite element analysis by Dao et al. [103] to accurately reproduce the RBCs' response. In addition, the experiments explained how RBCs can undergo high deformations during events such as passing through capillaries that have a diameter (3 μm) less than half a single RBC size (7.82 μm) without rupture. Moreover, these OT stretching experiments obtained a range of 0.13-0.26 seconds as a characteristic time for RBC relaxation, compared to micropipette aspiration recovery studies that yielded relaxation times of 0.10-0.13 seconds.

Also, their experimentally calculated membrane shear modulus μ was found to be 11-18 μN/m at typical strain values. This value was higher than 6-9 μN/m extracted from micropipette aspiration experiments [124].

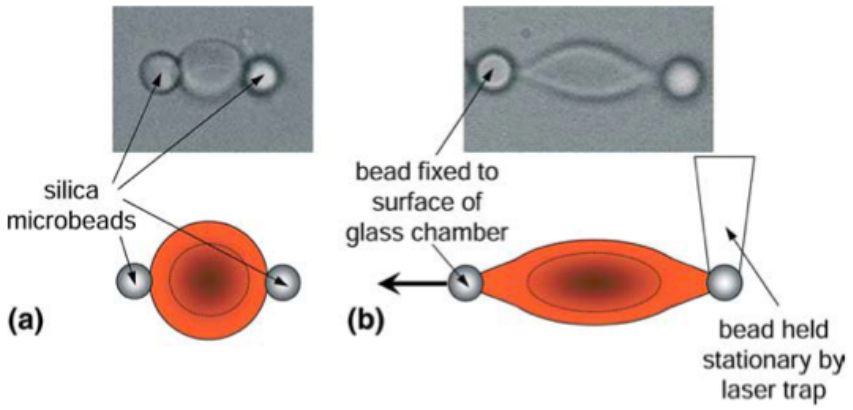

Figure 4.8: A red blood cell optically trapped, (a) before stretching, (b) after stretching. Figure taken from [123]

4.2.4 Microfluidics

An experimental technique that is gaining attention is the use of micro-fabricated models to replicate the real environment that the cells go through. For example, Shin et al. [125] studied the effect of shear rate $\dot{\gamma}$ on blood viscosity and RBCs' aggregability. They used backscattered light intensity and pressure measurements to determine the aggregability and stress-shear rate, respectively. The blood was sheared in micro-channels of size comparable to that of average blood vessels ($\sim$ 200 μm). Direct correlation was found between shear-thinning blood viscosity and the dependence of RBC aggregability on shear rates. Also, two critical shear rates were measured, *bottom critical shear rate* $\dot{\gamma}_{c,bot}$ and *top critical shear rate* $\dot{\gamma}_{c,top}$. The former value defines the shear stress under which RBCs completely aggregate, and the latter defines the limit of shear stress beyond which complete disaggregation of RBCs is observed, as shown in Figure 4.9 & 4.10. These two values provide insight into the shear-rate dependent behavior of RBCs, and define the region where further aggregation studies should focus.

Zhao et al. [126] performed a computational fluid dynamics (CFD) analysis combined with a microscopic experimental study to investigate the effect of exposing RBCs to high shear stresses for small time durations, and how these conditions affect the blood rheological properties and hemolysis in small artificial blood contacting devices (capillaries). A micro-fabricated channel was divided into 3 parts with the middle constriction dimension's $L \times W \times D$=2000 μm$\times$ 150 μm$\times$ 100 μm. The

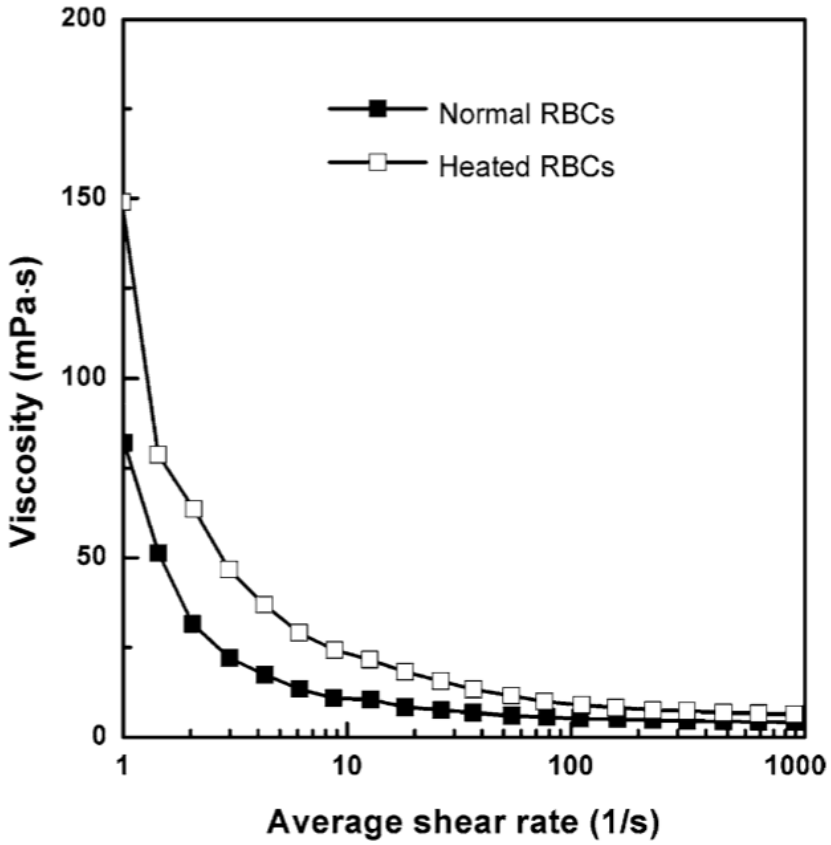

Figure 4.9: Blood viscosity of normal and heated RBCs for different shear rates (1/s). Figure taken from [125].

structural model of the fabricated channel which was used in the CFD analysis is shown in Figure 4.11a. This micro-channel was used to study the transient response of RBCs to high shear stress values up to 5000 Pa, as shown in Figure 4.11b. Also, they identified two phases for the deformation induced by shear stresses. The first phase showed EI=0-0.54 for stresses 0-123 Pa, where EI is the elongation index defined in equation (4.4), and a second phase with a plateau at EI=0.54 for stresses

above 123 Pa and up to 5170 Pa.

$$EI = \frac{L - W}{L + W}, \tag{4.4}$$

where L and W are the length of the major and minor axes of the elongated RBC.

It is worth mentioning that the elongation index (EI) is the same as the distortion parameter used in the strain-based hemolysis model which will be introduced

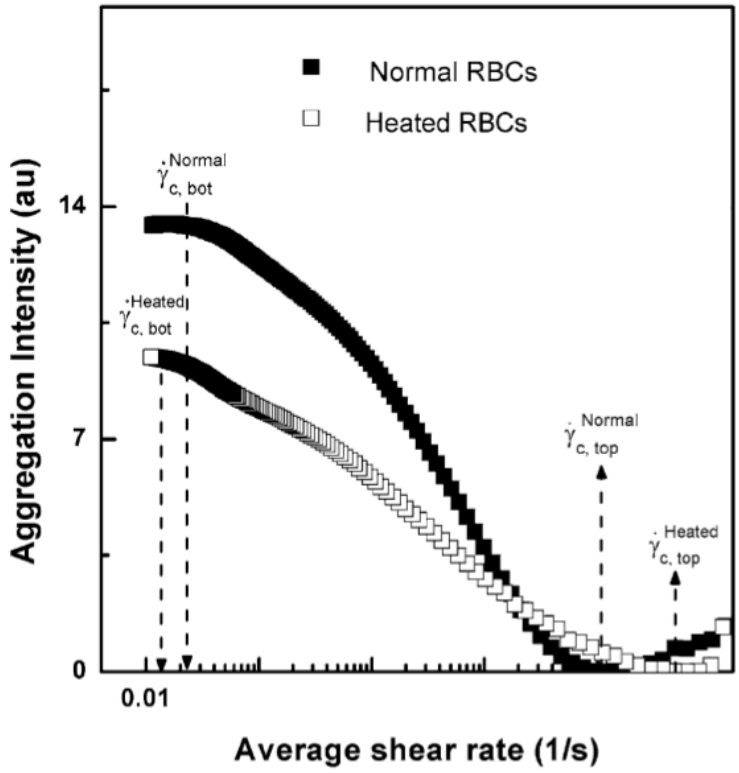

Figure 4.10: Aggregation intensity of normal and heated RBCs for different shear rates (1/s). $\dot{\gamma}_{c,bot}$ and $\dot{\gamma}_{c,top}$ are bottom and top critical shear stresses. Filled squares are for normal RBCs and open squares are for heated RBCs. Figure taken from [125].

in section 4.2.7. Therefore, this experimental data provides a useful reference for RBC response under transient loads, and can help in a qualitative sense the assessment of analytical models, since the RBCs used in the experiment were extracted from bovine blood, whose characteristics differ from that of human blood.

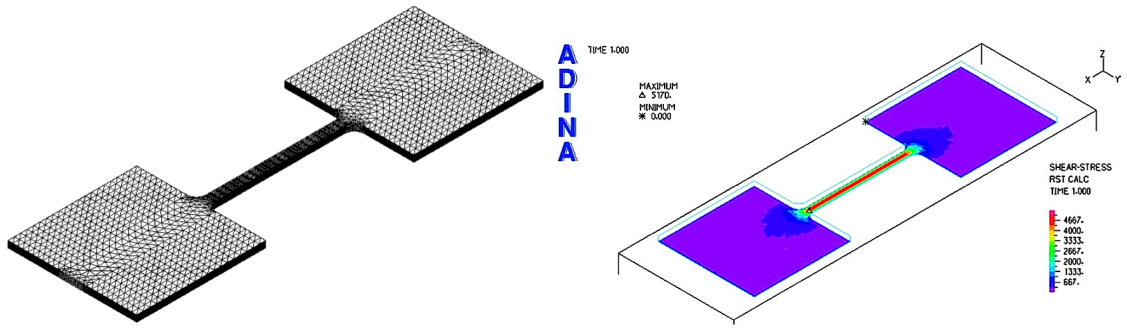

(a) (b)

Figure 4.11: (a) The structural model of the micro-fluidic channel used in the CFD analysis of Zhao et al.[126]. (b) The shear stresses observed throughout the channel. Figures taken from [126].

4.2.5 Red blood cells: *in silico*

Modeling RBCs atomistically, even though the simplest compared to other living cells, is impossible given the limited available computational resources. Mesoscopic modeling offers a coarser formulation of the molecular system wherein a less computationally expensive solution is implemented, yet some of the atomistic details can still be preserved. In some cases, where large systems are of interest, a continuum or a semi-continuum approach may be employed. Below we review some of the recently developed RBC models which extend from continuum-based models down to mesoscopic models.

Continuum scale models

Dao et al. [103] used finite element analysis (FEA) to study the mechanics of large RBC deformation under stretching via OT [123]. In their study, the cell membrane and the spectrin network were considered as an effective thin shell. They used several constitutive relations to model the RBC elasticity. However, a hyperelastic constitutive (material) model was assumed to accurately capture the large deformation response of the membrane and strain hardening effect at large strains. Figure 4.12 compares the deformation from experiments along with the FEA calculations. The axial/transverse diameters for various stretching forces for a shear modulus of 8 μN/m are plotted in Figure 4.13 with the experimental values and the results from the CG-MD analysis done by Dao et al. [127], showing good agreement. However, the values of the in-plane shear modulus assumed in their work was $\sim$ 19 μN/m, which is higher than that reported from the micropipette aspiration experiments [124]. The difference in the stress states and boundary conditions of the two techniques lend themselves to the discrepancy in the reported shear modulus values. The continuum approach by Dao et al. [103] revealed the importance of considering the internal fluid (cytosol) in the calculations, which ensures that unrealistic situations do not occur. For example, when no internal fluid was considered, different parts of the RBC membrane came into contact, specially at high pulling forces, which was not detected in the presence of the inner medium.

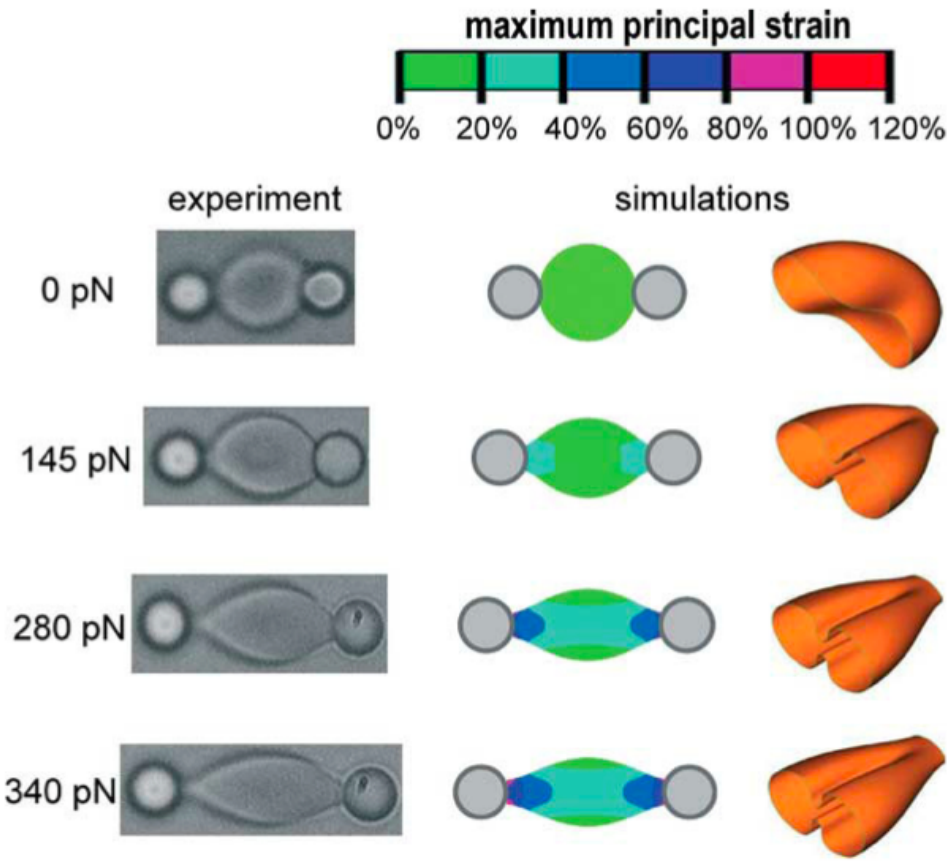

Figure 4.12: (left) Experimental deformation [123] under different stretching forces 0-340 pN; (middle) principal stress in the biconcave shell; (right) cross sections of the deformed RBC from the FEA model of Dao et al. [103].

Mesoscopic models

As an alternative to the continuum approach, coarse-graining (CG) has increasingly become the solution for many complex systems. CG's advantage stems from its capability to reduce the computational time many folds compared to fully atomistic models. However, this is usually at the expense of the level of detail that the simulations can provide. They can be used in cases where the detailed atomistic behavior of the system is not the main goal, rather its bulk characteristics. Typical

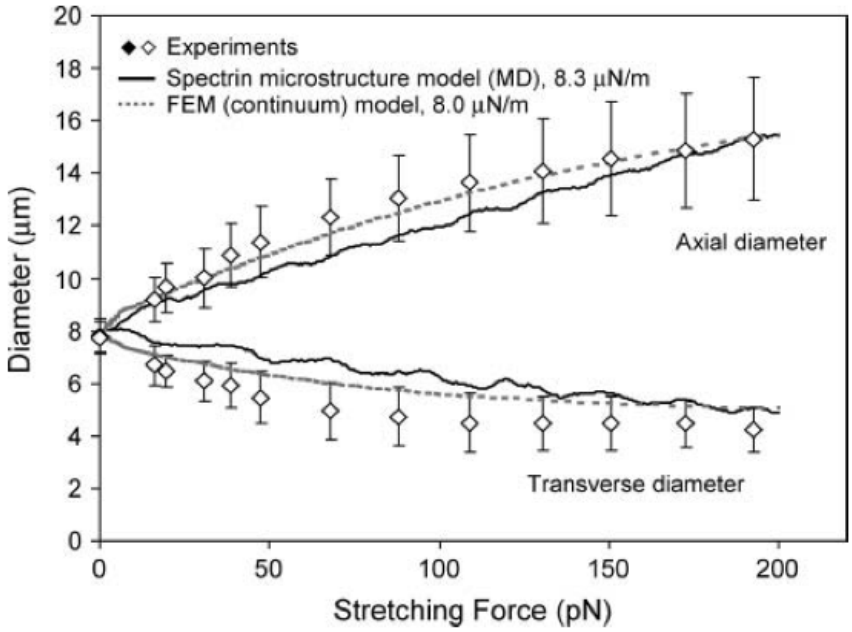

Figure 4.13: Axial and transverse diameters from experiments [103], FEA [103] and CG-MD [128]

coarse graining techniques eliminate high frequency motions, integrate a group of atoms into a particle, or implement an effective-type potential in which averaged spatio-temporal interactions are used instead of pair-wise interactions, much like typical molecular dynamics potentials.

Mesoscopic modeling of micropipette aspiration

As a mesoscopic modeling approach, Discher et al. [102] performed Monte Carlo simulations for micropipette aspiration of RBCs, as shown in Figure 4.14, using a mean effective network force field [114]. Their force field parameters were fitted to mimic the macroscopic properties of RBCs. The development of this potential opened a whole new area for modeling RBC dynamics and blood rheology

on that scale. In addition, they introduced the first discrete computational model that deals with a more realistic model for the RBCs, compared to the ellipsoidal approximations used before by Keller and Skalak [129]. They also investigated the effect of the network reference state on the response of the model. Three network models were inspected: free-stress, pre-stressed and condensed. Two out of the three examined models underpredicted the cap density (the membrane density at the cap of the aspirated part), however, the third model, the prestressed model correctly predicted the network density at the cap. Interestingly, these results were explained by the difference in the area compression modulus K, which has a larger value for the prestressed model, about double that of the stress-free and the condensed models. As will be discussed in the next sections, the success of the DPD model over others is the result of a more correct calculation of the area compression modulus K.

Dissipative Particle Dynamics

Dissipative particle dynamics (DPD), one of the emerging mesoscopic modeling techniques, is a coarse graining method proposed by Hoogerbrugge and Koelman [130] in 1992. Following its introduction, Español and Warren [131] set the relation between the dissipative and random weighting factors to statistically reproduce correct thermal equilibrium states. In DPD, two coarsening approaches are considered. First, a group of atoms is represented by an individual particle where a drastic re-

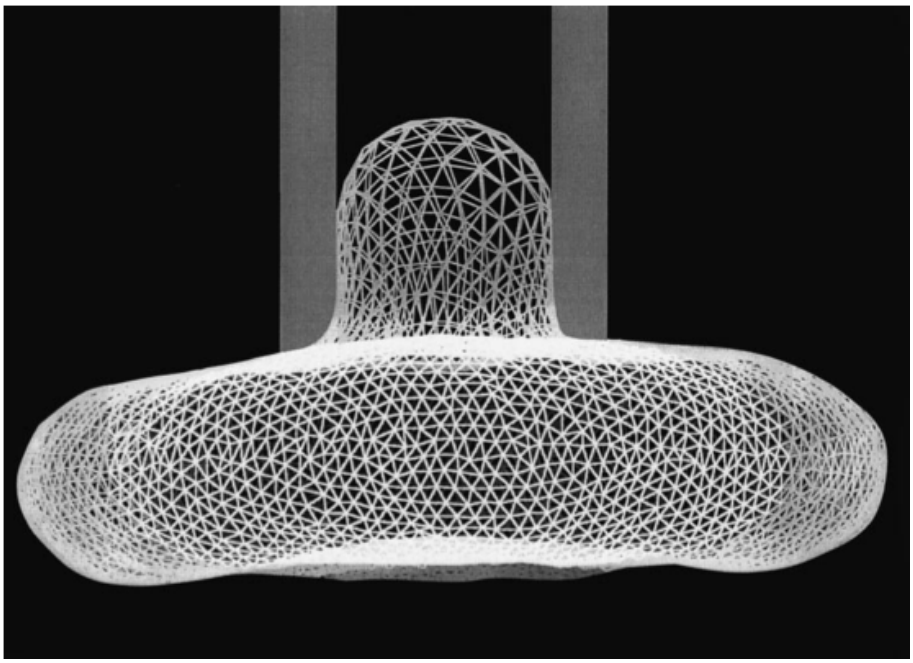

Figure 4.14: Simulations of a red blood cell under aspiration using Monte Carlo technique [102].

duction in degrees of freedom is achieved. Second, the interactions between groups of particles are described by a soft repulsion potential that replaces the hard core potential between molecular bodies. Thus, integration of the equations of motion can be performed at time steps that are orders of magnitude larger when compared with atomistic simulations.

Pivkin et al. [132] presented a RBC-CG model using DPD that reproduced accurately the non-linear behavior of the RBCs. They used a similar force field to that initially proposed by Discher et al. [102], which was also adopted by Dao et al. [127] with some changes. Also, Pivkin et al. [132] introduced minor changes in the area, volume and bending stiffnesses. Dao et al. [127] and later Pivkin et al.

[132] mapped the macroscopic properties of the spectrin network to the microscopic model parameter by studying the shear stresses experienced by a hexagonal network of triangles under a small engineering shear strain. Pivkin et al. [132] were able to reproduce, with good agreement, the stretching experiments performed using OT [103]. Afterwards, Fedosov et al. [116, 133, 115] enriched the model by investigating different potentials for the in-plane energy and the hydrostatic area. In addition, Fedosov et al. [116, 133, 115] compared their results with most of the experimentally available data on RBCs, for example, stretching [103], tumbling and tank treading [134, 135], structure recovery and thermal fluctuations [136, 137], and illustrated the ability of this CG-model to accurately reproduce the results. The wide range of experiments that were reproduced with that RBC-CG model demonstrate its strength in modeling either single RBCs under different loads, or the behavior of RBC clusters. Therefore, we have selected this model to be our starting point, which we will modify to study our cases of interest.

Multi-particle dynamics

Dzwinel et al. [118] modeled RBCs as a volume of solid elastic material having an inner skeleton. The model operates on scales within 0.001 and 100 μm. However, this model does not take into account the main structural features of a RBC (a membrane filled with a fluid), and therefore it cannot capture the proper dynamics of RBCs in shear flows, e.g. the tumbling and tank-treading behavior in shear flow [138].

Bagchi [113] used an immersed boundary-type method to model deformable single and multiple RBCs in a 2-D flow field. The cells were modeled as elastic capsules filled with viscous fluid [139]. This simple model was able to reproduce some of the RBC dynamic phenomena such as tank treading and tumbling in shear flow. Although Bagchi's studies covered a wide range of systems, from isolated RBCs to large ensembles of deformable RBCs, this model is limited due to its two dimensionality.

Coarse-grained molecular dynamics

Dao et al. [127] performed a set of spectrin level coarse-grained molecular dynamics (CG-MD) simulations to model the OT stretching experiments [103]. Their simulations studied the effect of the reference shape of the RBC triangulation on the equilibrium state of the RBC. Their work illustrated that the RBC biconcave shape stability is dependent on the geometrical frame of reference. Moreover, they studied the fluidity of the spectrin network using a flexible-bonds molecular dynamics, during which the connectivities amongst all vertices were allowed to change via an intermolecular potential, such as Lennard-Jones or Stillinger-Weber. Random networks with vertices of variable degrees from 2 to 10 were constructed. Then, these networks were equilibrated using coarse-grained molecular dynamics with a potential similar to that used by Discher et al. [102]. However, the Young's modulus clearly deviated from the experimental values, and that was manifested in the different slopes between the simulation force-elongation curve and the experimental one.

Moreover, the discoidal equilibrium shape was not achieved in simulations except by ramping up the bending rigidity κ_c orders of magnitude from the experimentally deduced value. The behavior of the MD-CG model, despite its properties matching the experimental values, deviates from the actual RBC response, i.e., in stretching experiments as shown in Figure 4.13. Fedosov et al. [116] revisited the derivation by Dao et al. [127] and reported that it is mathematically correct, although, physically it lacks the global area and volume contributions. When Fedosov et al. [116] incorporated these effects in the analysis, a more realistic Poisson ratio (ν=1) was deduced for a 2D area conserving network, besides the excellent agreement with the experimental data.

4.2.6 RBC-RBC interaction

Blood rheology studies depend on several different, although related factors, such as vessel geometry, cell deformability, wall compliance, flow shear rates, and many micro-scale chemical, physiological, and biological factors [140]. Therefore, in large scale simulations where myriads of RBCs are explicitly considered in the computational domain, accurate modeling of blood flow requires not only the modeling of a single RBC, but also accounting for the mutual interaction amongst RBCs, e.g., RBC aggregation and disaggregation. RBCs are known to form one-dimensional aggregates, similar to stacks of coins, called *Rouleaux*. These one-dimensional aggregates grow to form two and three-dimensional networks of RBCs as shown in Figure 4.15. These aggregations are a major determinant of blood viscosity in mi-

crocirculation under physiological and pathological conditions [141]. Increased RBC aggregability has been observed in various diseases, such as diabetes, thrombosis, myocardial infarction, vascular diseases, and hematological pathology [142]. When analyzing the association/dissociation of RBCs down to its fundamentals, one finds that the interactions between two biological membranes are either attractive (i.e., van der Waals, adhesion, electrostatic attraction, hydrophobic and bridging), or repulsive (i.e., electrostatic repulsion, steric repulsion and hydration) [143]. Therefore, it can be safely assumed that the effective cell-cell interaction is of a repulsive-attractive type potential. The parameterization of this potential is to be determined by fitting the experimental data. In next section, we discuss the models that have been proposed to simulate such cell-cell interaction.

Depletion-mediated aggregation model

The two main models proposed for RBC aggregation are bridging and depletion models, both of which consider the same repulsive interaction. However, they differ in the attractive component. The first model relates the RBC aggregation to adsorbing of the extracellular macromolecules onto adjacent cells surfaces, i.e. bridging the two surfaces via extracellular macromolecules [144]. The second model, proposes that RBC cell aggregation occurs as a result of osmotic attractive forces due to polymer depletion, lower localized protein or polymer concentration near the RBC surface.

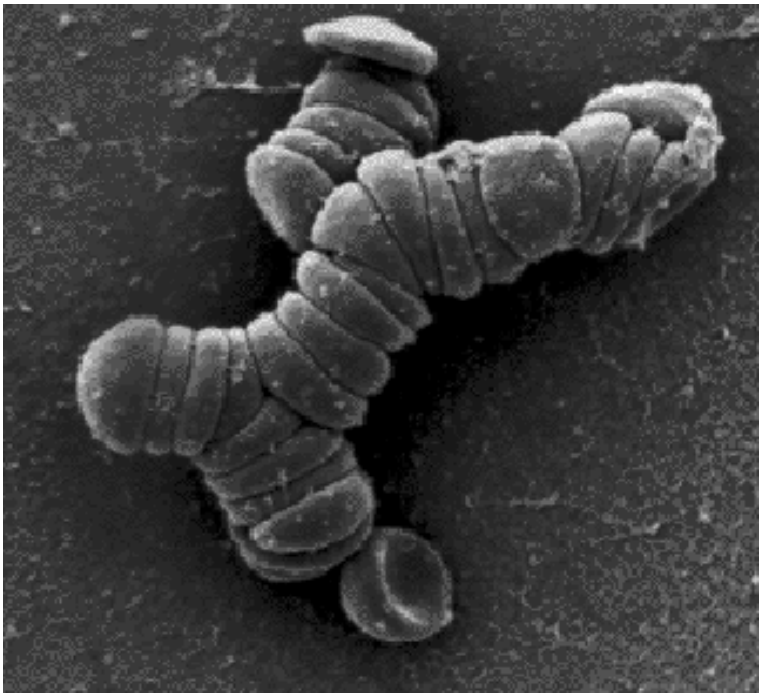

Figure 4.15: Rouleaux-aggregates of red blood cells. This picture has been taken from R. de Roeck and M.R. Mackley, Department of Chemical Engineering, University of Cambridge (available at:http://www.de-roeck.co.uk/Research.htm)

Neu and Meiselman [145] proposed a theoretical model for depletion-mediated RBC aggregation in polymer solutions. In their formulation, the total interaction energy ϕ per unit area of cell surface is given by the summation of the depletion interaction energy, w_D, and the electrostatic interaction energy, w_E, as:

$$\phi = w_D + w_E \tag{4.5}$$

The effects of different polymers, such as Dextran and poly ethylene glycol, concentrations and physicochemical properties of polymers on the depletion layer thickness and on polymer penetration into the RBC glycocalyx were studied. The

calculated interaction energies were in excellent agreement with literature data for cell-cell affinities [146] and with RBC aggregation-polymer concentration relations [145].

While Neu and Meilselman [145] focused on the mechanism of aggregation, Liu et al. [140] were interested in the aggregation related rheological effect. Therefore, they studied blood rheology using the immersed finite element method (IFEM), which is an extension of the immersed boundary method developed by Peskin [147], to solve the interactions between both the RBC structural domain and the fluid domain. In this scheme both the solid and the fluid domains are modeled through finite element methods (FEM). In IFEM, the deformable structure is modeled by a Lagrangian mesh that moves on top of an Eulerian fluid grid that defines the entire computational domain [148]. The IFEM method proves promising for the solution of many complex fluid-structure interaction problems encountered in many physical systems spanning multi-scale flows, such as flow in organs, e.g., heart; in blood vessels, e.g., arteries and veins; around cells, e.g., RBCs aggregation, as shown in Figure 4.16.

To complement their studies, Liu et al. [140] had to look at the effect of aggregation, in which Liu and Liu [149] made use of the theoretical depletion-mediated model proposed by Neu and Meilselman [145], and fitted the interaction potential curves from [145] using a Morse potential type of curve. They introduced an expression for the interaction energy and force as a function of the RBC-RBC separation,

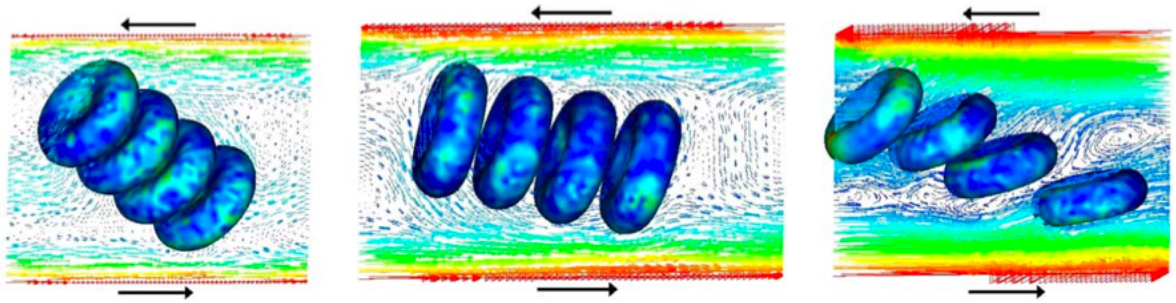

Figure 4.16: Cluster of four RBCs under different shear rates, 0.25, 0.5 and 3.0 s^{-1} [140]

r, as shown in Figure 4.17. In addition, Liu and Liu [149] validated their computational results with well-known phenomena, such as the shear rate dependence of blood viscosity, the influence of cell rigidity on blood viscosity, and the *Fahraeus-Lindqvist* effect. Also, they looked at the change in adhesion energy with shear rate, and how this explains the disaggregation mechanism of RBCs rouleaux under high shear rates. The success achieved by this technique demonstrates the capability of the depletion-mediated model [145], and consequently, the mathematical expression representing it, to simulate RBC clusters' behavior and study their effect on hemorheological properties.

4.2.7 Blood-damage prediction models

After shedding light on the different RBC components, as well as the experimental work and techniques used in their studies, it is time to move on to the core of our proposed work, which is the investigation and prediction of hemolysis. The understanding of the hemolysis process itself is still ambiguous. The mainstream

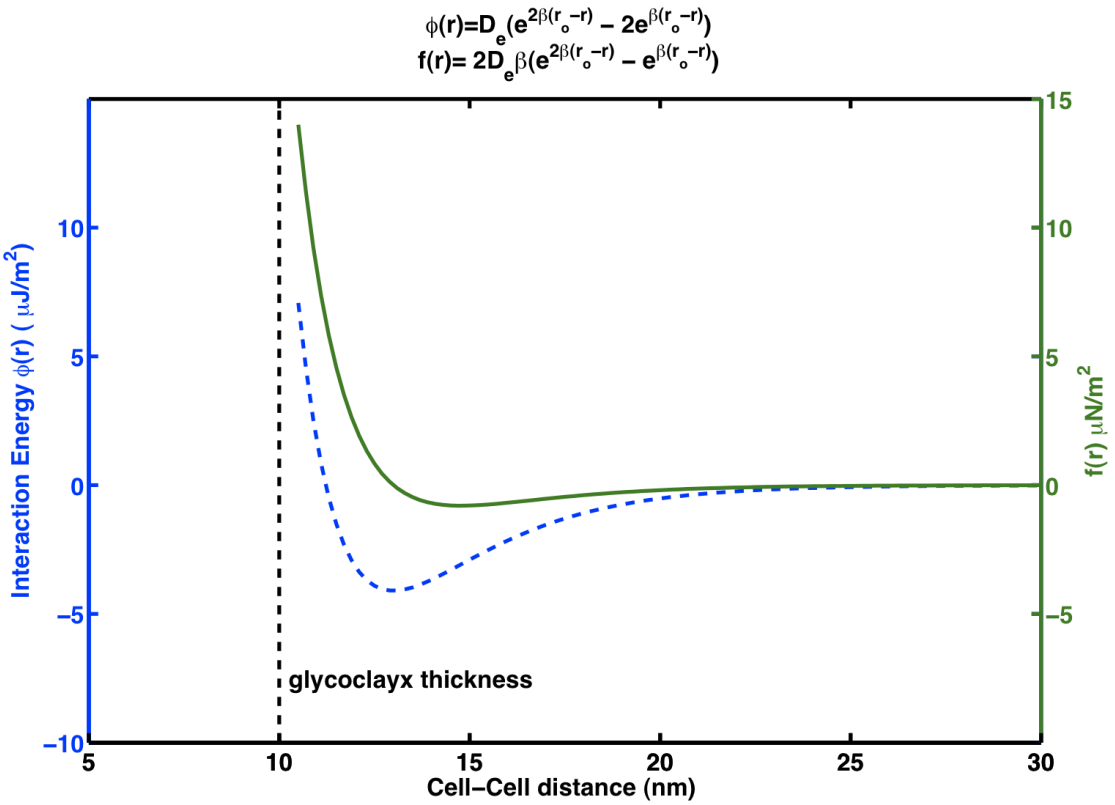

Figure 4.17: Cell-cell interaction potential and force. (left axis) Interaction potential $\phi(r)$ per unit area, where r is the separation distance between the two cell surfaces. (right axis) Interaction force $f(r)$, between the cell surfaces, per unit area. $D_e = 4.1\mu J$, $r_o = 13$ nm, $\beta = 0.39nm^{-1}$ [149]

research on this topic focuses on the macroscopic behavior of blood under loading conditions. For example, Li et al. [128] proposed a quasi-coarse grained model to detect RBC bond breakage/formation. They approached the phenomenon from the molecular point of view, and developed a framework that describes the behavior of the spectrin network and the lipid membrane. They represented the behavior of the cytoskeleton both as an inert structure, as well as a bio-chemically activated system. In addition, their model investigated the two temperatures concept [150],

where the thermodynamic temperature (k_BT) is responsible for the general degrees of freedom, and the effective temperature determines the structural evolution. Their model could provide significant insight into the microscopic-hemolysis process if incorporated into a complete RBC model rather than simulating a 2D-rectangular sheet of spectrin links.

On the macroscopic level, hemolysis studies are dated to more than four decades ago. Giersiepen et al. [110] proposed the most popular model, one of the stress-based models as will be illustrated in the next section, where the amount of hemolysis and its rate of change are related to the shear stress values and the exposure times as indicated in equation (4.6) & (4.7), respectively (these equations are explained below).

While it is known that shear stresses cause deformation and possibly damage of RBCs, not only the magnitude of the shear, but also the duration of exposure affect greatly the response of the cell. Experiments have shown different response to different combinations of shear values and exposure time. Low shear stresses at low exposure times cause reversible elastic deformations (viscoelastic solid behavior). At longer exposure times the same low shear stresses produce irreversible shape changes (semi-solid behavior). At high shear stresses, the RBC structure might undergo lethal damage [7]. Therefore, over the last four decades, experimental work targeted quantifying the amount of shear-induced blood-damage. Grigioni et al. [8] tabulated the experiments done using different setups, including turbulent jets,

oscillating wires and bubbles, capillary flows and concentric cylinders, while varying the exposure times and the lethal shear stresses. Inspection of these experiments highlights the need for more rigorous mathematical models that can predict such blood behavior over this wide range of shear stresses and exposure times. Accordingly, models were proposed to provide mathematical formulas that can be used to predict blood-damage in artificial organs [8].

Current blood-damage models can be categorized into stress-based and strain-based models [109]. As can be inferred from their names, the former rely on the stresses to quantify hemolysis, while the latter use the strain to produce the same results. Regardless of the measures used to predict hemolysis, any model should consider all the factors that affect this phenomenon. Arora [109] listed the ideal set of characteristics that an accurate blood-damage model would have to possess. A summary of these characteristics is listed below, complemented with other aspects mentioned by Griogioni et al. [7] for developing a generalized rigorous blood-damage model:

a. The model parameters should be optimized for the sample under study, since blood properties change from one species to another, i.e., human blood compared to bovine blood. Also, it should account for the physical phenomena associated with blood flow, e.g., tank treading and tumbling.

b. Physiological blood flow conditions may affect hemolysis significantly, e.g., blood-contacting surfaces, blood-air contact, thermal hemolysis, etc., therefore

the model should eliminate these effects if it doesn't account for them.

c. The model must agree with both steady and unsteady simple-shear hemolysis data (not accurately obtained yet).

d. The model should span the complete spatial domain. Since the phenomenon is inherently a three-dimensional problem, then the model should be of the same construction. This means that the rate-of-strain tensor and the vorticity tensor should represent the full spatial domain and should not be abstracted to scalar values ignoring the problem's original characteristics.

e. The model integration with a continuum CFD solver should be simple to implement. In addition, the model should be numerically mapped to the clinical metric of hemolysis that is, to the normalized index of hemolysis (NIH). [108]

In addition, Grigioni et al. [7] add two important characteristics of a rigorous model,

a. It must satisfy the principle of causality, thus the model should not reduce the accumulated damage, even if the mechanical load present is decreased.

b. The model must account for loading history, allowing for two RBCs to behave differently to the same load, if they have different reference deformation states.

Stress-based hemolysis models

Blackshear et al. [151] were the first to express, using a power-law relation, the hemolytic effect of hydrodynamical shear on RBCs using a Couètte viscometer. Afterwards, Giersiepen et al. [110] correlated the amount of hemolysis and its rate of change to the turbulent shear stress and exposure time as shown in equations (4.6) & (4.7), also known as blood damage index (BDI), through a power-law formulation,

$$\frac{\Delta Hb}{Hb} = 3.62 \times 10^{-7} \ \tau^{2.416} \ \Delta t^{0.785} 100\%, \tag{4.6}$$

$$\frac{d}{dt}\left(\frac{\Delta Hb}{Hb}\right) = 2.8417 \times 10^{-7} \ \tau^{2.416} \ \Delta t^{-0.215}, \tag{4.7}$$

where τ is the steady shear stress in *(Pa)* and Δt is the exposure time in (*seconds*). However, this model lacks some traits that weaken its rigorousness and generality. For example, it accounts only for the uniform shear stress. However, RBCs are subjected to time-varying, pulsatile in nature, loading [8, 152]. Moreover, the model does not account for loading history. Therefore, Grigioni et al. [8] emphasized the need for developing prediction models that account for all the factors that affect the hemolysis process.

Afterwards, Girgioni et al. [7] proposed a new model, whose blood damage index (BDI) expression is shown in equation (4.8), which includes the desired characteristics. However, the difficulty of collecting experimental data to validate this

model renders it unverified .

$$BDI = \sum_{i=1}^{N} C\ a \left[\sum_{j=1}^{i} \tau(t_j)^{b/a} \Delta t_j + D(t_0) \right]^{a-1} \tau(t_i)^{b/a} \Delta t_i, \tag{4.8}$$

where N is the number of observation time intervals (number of time steps) along the fluid pathline. C, a and b are constants. $D(t_0)$ is the *mechanical dose* (damage) at t_0. The j^{th} observation step is the time step that precedes i^{th} step, meaning $j = i - 1$.

Additionally, Grigioni et al. [153] and Lu et al. [154] reevaluated a long-cited publication by Sallam and Hwang [155] which predicted that the shear-induced hemolysis threshold is 400 N/m^2. Discussions from both papers [153, 154] point to the incompleteness of the approach taken in the above mentioned publication [155] and illustrated that 400 N/m^2 was an underestimated shear stress threshold.

Strain-based hemolysis models

In addition to the stress-based models, there also exist strain-based models. The area tensor approach, equivalent to the interfacial tensor introduced by Doi and Otha [156], was used to investigate the evolution of a fluid-like droplet in a flow field by Maffettone and Minale [157]. Similarly, Wetzel and Tucker [158] used this approach to model microstructures in laminar mixing of immiscible fluids. The temporal behavior of the area tensor is deduced from the solution of the flow field. The area morphology tensor contains significant information about the size, shape,

and orientation of the local morphology of the discrete-phase in a continuous domain. Arora et al. [6] modified the equation of change introduced by Maffettone and Minale [157] to account for the physical characteristics of RBCs, i.e. *tank treading*.

As mentioned above the area morphology tensor holds useful information about the dispersed phase. When rotated to its principal axes system, i.e., when the tensor is diagonalized, the principal directions (which represent the eigenvectors of the tensor) are indications of the most and least likely orientation of the morphology and the proportions of interfacial area are indicated by the area tensor eigenvalues λ_i, $i = 1, 2$, *up to* d, where d is the spatial dimension [158].

Arora et al. [6] proposed a modification to the evolution equation of the morphology tensor $\mathbf{S}$ previously proposed by Maffettone and Minale [157]. Arora et al. [6] modeled the physical phenomenon of RBCs, i.e. tank treading, via a rotating frame of reference with respect to the fixed one. However, for this model to be correct, the RBCs are assumed to have ellipsoidal shape, and remain ellipsoidal. However, Fedosov et al. [115] simulations show that the tank treading phenomena exhibits RBC membrane rotation combined with structural deformation.

In the strain-based model proposed by Arora er al. [6] the morphology tensor is evolved along path-lines to simulate RBC trajectories. The calculations for the morphology tensor are done off-line (post-processing) and along fictitious path-lines. Smaller time steps are used for the integration of the tensor-evolution equa-

tion. When the tensor is available over the whole simulation time, the distortion parameter ϕ, expressed in equation (4.9), can be calculated. Hence, the strain-based hemolysis equation could be used to predict hemolysis.

$$\phi = (L - B)/(L + B) \tag{4.9}$$

where L and B are the axial lengths of RBCs, which are the eigenvalues of the morphology tensor $\mathbf{S}$.

The aforementioned hemolysis models, either stress based or strain-based, emphasize the need for advancements in measurement techniques and instruments, which can enhance the accuracy of hemolysis measurements and potentially provide experimental data for hemolysis under unsteady shear loading. Before this can be done, the only verified models available would be the ones that can be compared with uniform shear stress experimental data.

4.3 Methods and techniques

4.3.1 RBC coarse-grained model

Below are the methods and techniques that were employed to accomplish our work. First, the CG-RBC model will be discussed. Second, the modified membrane viscous model will be illustrated. Third, the current hemolysis models used in our study, then we introduce the coarse-grained hemolysis model. Finally, we present the RBC-RBC interaction model.

CG-RBC model: The model presented by Pivkin et al. [132] and further enhanced by Fedosov et al. [116] will be our starting point. It was initially developed by Discher et al. [102]. The model abstracts the whole RBC structure to a two-dimensional network, mimicking the spectrin network which underlies the lipid membrane. However, this network possesses the mechanical characteristics of the whole RBC architecture. Thus, the free energy expression, equation (4.10)), accounts for the elastic energy in the spectrin network, area conservation and bending energies due to the lipid-bilayer membrane and volume conservation energy due to the incompressible content, i.e. *the cytosol*.

Fedosov et al. [116] revisited the previous analysis done by Dao et al. [159] for the stresses on the hexagonal network. They realized that it lacks the full definition of the contributing forces. Hence, they complemented this analysis by accounting for

the global and local area effects which improved the accuracy of the model-deduced properties, namely the shear modulus μ_o and the modulus of area compressibility K. For a detailed derivation of the mechanics refer to [116].

The free energy expression for the RBC can be viewed as the sum of the free energies of the different RBC architecture components.

$$E_{RBC} = E_{in-plane} + E_{bending} + E_{volume} + E_{area}, \tag{4.10}$$

$$E_{in-plane} = \sum_{i \in links} V_{WLC}(L_i) + \sum_{j \in triangles} C_q/A_j, \tag{4.11}$$

$$V_{WLC}(L) = \frac{k_B T L_{max}}{4p} \frac{3x^2 - 2x^3}{1 - x}, \tag{4.12}$$

where $x = L/L_{max} \in (0, 1)$, L_{max} is the maximum length of the network links, p is the persistence length (m), k_B is the Boltzmann constant and T is the thermodynamic temperature (K).

$$C_q = \frac{3\sqrt{3} k_B T L_{max}^3 x_o^4}{64p} \frac{4x_o - 9x_o + 6}{(1 - x_o)^2}, \tag{4.13}$$

$$E_{bending} = \sum_{kl \ Adjacent \ triangles} k_{bend} \ [\ 1 - cos(\theta_{kl} - \theta_o) \ ], \tag{4.14}$$

$$E_{area} = \frac{k_a(A - A_o^{tot})^2}{2A_o^{tot}} + \sum_{j \in 1...N_t} \frac{k_d(A_j - A_o)^2}{2A_o}, \tag{4.15}$$

$$E_{volume} = \frac{k_v(V - V_o^{tot})^2}{2V_o^{tot}}, \tag{4.16}$$

where k_a, k_d and k_v are the global area, local area and volume constraint constants, respectively. $A_o = \sqrt{3}l_o^2/4$, A_j is the area of the triangle j, A_o^{tot} and V_o^{tot} are the reference total area and volume, respectively, and they are set equal to the total area and volume after the RBC triangulation.

From the above energy formulation, the exact nodal forces can be obtained analytically. For every node i the force f_i is calculated.

$$f_{i,\ bonded} = \frac{\partial E_{RBC}(x_i)}{\partial x_i}, \tag{4.17}$$

where x_i are the Cartesian coordinates x, y *and* z for *i=1, 2 and 3*, respectively.

The forces obtained from equation (4.17), by taking the spatial derivative of the RBC free energy, equation 4.10, define the interactions among the RBC nodes. These interactions can be divided into three classes: two-node interactions, calculated for all the links on each RBC surface, e.g., forces due to in-plane bond energy; three-node interactions, calculated for all the elements (triangles) on the RBC surface, e.g., forces due to area and volume constraints; four-nodes interactions, these involve adjacent elements, e.g., forces due to bending energy.

While the above forces define the intra-RBC interactions, i.e., *bonded* interactions, governing the behavior of the RBC structure, the interactions of the RBC nodes with the internal/external fluid particles, i.e., *non-bonded* interactions, are governed by the general potential defined by Hoogerbrugge and Koelman [130], a pairwise interaction potential, where the forces between two particles i and j comprise three components; conservative, dissipative and stochastic, as shown in equation (4.18). The last two components act as a thermostat to keep the mean temperature of the system constant, while the first term defines the chemical identity of the particles.

$$f_{i,\ non-bonded} = \sum_{j=1, j\neq i}^{N} (F_{ij}^{C} + F_{ij}^{D} + F_{ij}^{R}), \tag{4.18}$$

where each term of the above expression is generally composed of a weight function multiplied by the unit vector from particle i to particle j, as shown in equation (4.19).

$$F_{ij}^{C} = a_{ij}\omega_C(r_{ij})\hat{r}_{ij} \quad (r_{ij} < 1), \tag{4.19}$$

$$F_{ij}^{D} = -\gamma\omega_D(r_{ij})(r_{ij}\dot{v}_{ij})\hat{r}_{ij} \quad (r_{ij} < 1), \tag{4.20}$$

$$F_{ij}^{R} = \sigma\omega_R(r_{ij})\hat{r}_{ij}\xi_{ij}/\sqrt{\Delta t} \quad (r_{ij} < 1), \tag{4.21}$$

where a_{ij} defines the amplitude of the repulsive force between the two particles, σ and γ are interpreted as the amplitude of the noise and the friction coefficient, respectively. ω_C, ω_D and ω_R are weight functions that provide the range of interaction for the conservative, dissipative and random forces. The choice of ω_C is arbitrary

as long as it satisfies the condition of diminishing force at increasing separation $r_{ij} \geq r_c$. Español and Warren [131] defined the relation between ω_D and ω_R, as shown in equations (4.22) & (4.23), for the system to reproduce correct statistical equilibrium states.

$$\omega_R(r_{ij}) = \sqrt{\omega_D(r_{ij})}, \tag{4.22}$$

$$\sigma = \sqrt{(2k_B T\gamma)}. \tag{4.23}$$

The above bonded and non-bonded forces provide the complete force field under which the system of DPD and RBC particles can evolve following Newton's equations of motion, namely,

$$\frac{dx_i}{dt} = v_i \tag{4.24}$$

$$\frac{dv_i}{dt} = f_i \qquad where \quad m = 1 \tag{4.25}$$

The progression of the particles is achieved by numerically integrating equation 4.24 & 4.25. Many techniques has been used to perform this temporal integration. The modified verlet scheme, equations (4.26) to (4.29), will be used in this work. In this integration scheme, the velocities of the particles are updated twice each time step, while the forces, which are the most time consuming computations, are only calculated once. Since the DPD force field relies on the relative velocities, as opposed to MD where forces depend only on coordinates, this integration scheme

calculates the velocity of the system at $t + \Delta t$:

$$r_i(t + \Delta t) = r_i + \Delta t v_i(t) + \frac{1}{2}(\Delta t)^2 f_i(t), \tag{4.26}$$

$$\widetilde{v_i}(t + \lambda \Delta t) = v_i(t) + \lambda \Delta t f_i(t), \tag{4.27}$$

$$f_i(t + \Delta t) = f(v_i(r(t + \Delta t), \widetilde{v_i}(t + \Delta t))), \tag{4.28}$$

$$v_i(t + \Delta t) = v_i(t) + \frac{1}{2}\Delta t(f_i + f_i(t + \Delta t)), \tag{4.29}$$

where λ is a weighting factor that determines the step at which the intermediate velocity correction takes place. Usually λ is taken equal to 0.5 to update the velocities at half the time step Δt.

4.3.2 Membrane visco-elasticity

The free energy expression introduced above, in equation (4.10), deals with the RBC structure as a pure elastic material. This is acceptable for certain problems, for example, if the dynamics of the RBC are not important, such as in the stretching experiments by Fedosov et al. [116]. Realistically, this is not true as it neglects the dissipative nature of the lipid membrane. Therefore, we will follow the fluid particle model introduced by Español [160] and implemented by Fedosov et al. [115] in the CG-RBC model to incorporate the viscoelastic effects into the intra-RBC forces. The model modifies the forces due to the in-plane energy from only having an elastic behavior, attractive and repulsive components, and adds dissipative and random forces that satisfy the dissipation-fluctuation theorem. The following equations de-

fine the dissipative and stochastic forces acting along the inter-particle separation vector $\hat{r}_{ij}$ in order to model accurately the visco-elastic properties of the RBCs.

$$\mathbf{F}_{ij}^{D} = -\mathbf{T}_{ij} \cdot \mathbf{v}_{ij}, \quad \mathbf{T}_{ij} = A(r_{ij})\mathbf{1} + B(r_{ij})\mathbf{e}_{ij}\mathbf{e}_{ij}, \tag{4.30}$$

$$\mathbf{F}_{ij}^{R} = \sqrt{2k_BT}\left(\tilde{A}(r_{ij})d\overline{\mathbf{W}_{ij}^{s}} + \tilde{B}(r_{ij}\frac{tr[d\mathbf{W}_{ij}]}{3}\mathbf{1} + \tilde{C}(r_{ij})d\mathbf{W}_{ij}^{A}\right) \cdot \mathbf{e}_{ij}, \tag{4.31}$$

where $\mathbf{e}_{ij} = \hat{r}_{ij}/r_{ij}$ is the unit vector between the particles i and j, r_{ij} is the magnitude of the vector $\hat{r}_{ij}$.

$$A(r) = \frac{1}{2}\left[\tilde{A}^2(r) + \tilde{C}^2(r)\right], \tag{4.32}$$

$$B(r) = \frac{1}{2}\left[\tilde{A}^2(r) - \tilde{C}^2(r)\right] + \frac{1}{3}\left[\tilde{B}^2(r) - \tilde{A}^2(r)\right], \tag{4.33}$$

A(r) and B(r) are set to γ^T and γ^C, respectively. Then, $\mathbf{T}_{ij} = \gamma^T\mathbf{1} + \gamma^C\mathbf{e}_{ij}\mathbf{e}_{ij}$, where γ^T and γ^C are the dissipative coefficients. Now, the dissipative interactions can be rewritten as,

$$\mathbf{F}_{ij}^{D} = -[\gamma^T\mathbf{1} + \gamma^C\mathbf{e}_{ij}\mathbf{e}_{ij}] \cdot \mathbf{v}_{ij} = -\gamma^T\mathbf{v}_{ij} - \gamma^C(\mathbf{v}_{ij} \cdot \mathbf{e}_{ij})\mathbf{e}_{ij}, \tag{4.34}$$

$$\mathbf{F}_{ij}^{R} = \sqrt{2K_BT}\left(\sqrt{2\gamma^T}d\overline{\mathbf{W}_{ij}^{s}} + \sqrt{3\gamma^C - \gamma^T}\frac{tr[d\mathbf{W}_{ij}]}{3}\mathbf{1}\right) \cdot \mathbf{e}_{ij}, \tag{4.35}$$

where $tr[\mathbf{W}_{ij}]$ is the trace of the random matrix of Wiener increments $d\mathbf{W}_{ij}$, and the $d\overline{\mathbf{W}_{ij}^{s}}$ is the traceless symmetric part, with $d\mathbf{W}_{ij}^{s} = \frac{1}{2}[\mathbf{W}_{ij} + \mathbf{W}_{ij}^{T}]$.

The above defined dissipative and random forces combined with the elastic spring (due to in-plane energy) forces resemble a viscoelastic spring with a constant equilibrium temperature equal to $k_B T$.

Finally, the membrane shear viscosity is related to the dissipative coefficients γ^T and γ^C as in equation (4.36), by applying a constant shear rate $\dot{\gamma}$ to the hexagonal network of triangles. Then, the shear stress τ_{xy} is proportional to the shear rate $\dot{\gamma}$ via the membrane viscosity η_m.

$$\eta_m = \sqrt{3}\gamma^T + \frac{\sqrt{3}\gamma^C}{4} \tag{4.36}$$

4.3.3 Application of the Pathlines to the coarse-grain RBC model

The hydrodynamic loading results in local forces f_i that are transmitted from the fluid to every element i on the RBC surface by the dot product of $\mathbf{T}$, the stress tensor (due to the hydrodynamic load), and n_i the normal to each triangular plaquette. The stress tensor $\mathbf{T}$ applied to the RBC was calculated from the velocity gradient

tensor ∇u by the following relation:

$$\mathbf{T} = -p\mathbf{I} + \boldsymbol{\tau}, \quad \text{where} \quad \boldsymbol{\tau} = \mu(\nabla u + \nabla u^T), \tag{4.37}$$

where p is the pressure, $\mathbf{I}$ is identity matrix, τ is the deviatoric stress tensor and μ is the fluid viscosity. The resultant forces act on the centers of the triangular elements. Afterwards, they are divided equally across the participating nodes of each element to compute the nodal forces.

4.3.4 The hemolysis models considered

Since one of our goals in this work is to fill the gap between the collective hemolysis models, either stress-based or strain-based, and the proposed molecular model in hand, we first compare the calculated blood damage using the deformation of an actual RBC model [116, 115] to the damage predicted by the droplet model proposed by Arora et al. [6]. This comparison is very beneficial, because it tests how accurate the droplet model in simulating the dynamics of the RBCs. Additionally, we show how this compares to the widely used stress-based model by Griepsen et al. [110] shown in equation (4.38) and its modified version by Grigioni et al. [7], equation (4.39) .

$$\Delta H_i = \alpha C t_i^{\alpha-1} \tau(t_i)^{\beta} \Delta t_i \tag{4.38}$$

$$\Delta H_i = \alpha C \left[\sum_{j=1}^{i} \tau(t_j)^{\beta/\alpha} \Delta t_j + HI(t_o) \right]^{\alpha-1} \tau(t_i)^{\beta/\alpha} \Delta t_i \tag{4.39}$$

Note that the strain-based model by Arora et al. [6] use the same functional form, shown in equation (4.38), to predict the blood damage as the one proposed by Griepsen et al. [110]. However, both differ in how the scalar measure of the hydrodynamic stress is defined. The first computes τ, in equation (4.38), as a function of the distortion parameter ϕ as a measure of the strain in the RBC, shown in equation (4.40). While the latter uses $\tau = \sqrt{\frac{1}{2}\boldsymbol{\tau} : \boldsymbol{\tau}}$, as the instantaneous measure of the shear stresses.

$$\tau = \mu \frac{(\phi f_1)}{(\sqrt{1-\phi^2} f_2)}, \tag{4.40}$$

where ϕ=$(\lambda_{max} - \lambda_{min})/(\lambda_{max} + \lambda_{min})$ is the instantaneous shape distortion parameter introduced by Arora et al. [6], λ_{max} and λ_{max} are the maximum and minimum eigenvalues of the morphology tensor $\mathbf{S}$) of the droplet. In our simulations, we calculated the distortion parameter, ϕ from the eigenvalues of the inertia tensor $\mathbf{I}$ of the RBC coordinates produced by our simulations.

4.3.5 Coarse-Gained Hemolysis Models

Now we introduce how hemolysis is explored locally on the RBC surface. In other words, instead of studying the overall deformation of the RBC, a more detailed information was used to explore how hemolysis happens on the microscale. Before

being able to apply Evans et al. [161] hypothesis to our simulations, we need to calculate locally at every node on the RBC surface the tension, area expansion and bending. Additionally, since the failure of the membrane is rate dependent, the rate of loading also has to be calculated at each time step. Finally, we need a method to calculate the statistical probability of failure, because of all the uncertainties in the process including the model, assumptions to simplify the flow characteristics, etc.

To use the relations deduced by Evans at al. [161], we needed a method to calculate the surface tension map on the discretized RBC surface. Therefore, a constitutive relation between the forces acting on the nodes and the resultant surface tension is obtained is required. We started from the analysis carried by Dao et al. [127] and extended by Fedosov et al.[116, 115] for a hexagonal network of equilateral triangles, then we tailored the analysis to a more generalized case. From the arbitrary hexagonal network shown in figure 4.18, we can divide the forces sensed at the vertices of this triangular network into in-plane and out-of-plane forces. Only the in-plane forces are relevant in this analysis because they induce changes in the area of the triangular plaquettes. Each vertex in the network is associated with cn links (where cn_i is the coordination number of vertex i), however, each link is shared by two vertices. Therefore, each vertex is virtually affected by $cn_i/2$ links. Similarly, each vertex participates in cn_i elements. While every element is shared by three vertices, consequently, each vertex is affected by $cn_i/3$ triangular elements. The Cauchy stress tensor $\tau_{\alpha\beta}$ can be calculated from the Virial (See chapter 2 in [162]) for the pairwise interaction between the vertices. In addition, the forces from

the area constraints can be obtained from the differentiation of the energy terms,

$$\tau_{\alpha\beta}|_{springs} = -\frac{1}{S}\left[\frac{1}{2}\sum_{i=1}^{cn}\frac{f(r_i)}{r_i}r_i^{\alpha}r_i^{\beta}\right], \tag{4.41}$$

where $f(:)$ is the spring-like force between two vertices, r_i are the coordinates of neighboring vertices where $i = 1, 2, \ldots cn$, and cn is the coordination number of each vertex. α and β can be x or y. $S = cn/3\sum_i^{cn} A_i/cn$ is the representative area element (RAE) associated with the node v.

$$\tau_{\alpha\beta}|_{area} = -\left[\frac{1}{3}\sum_{i=1}^{cn}\frac{k_a(A_{oi} - A_i)}{A_{oi}}\right]\delta_{\alpha\beta}, \tag{4.42}$$

where k_a is the global area constrain coefficient, A_{oi} is the initial area of the triangular plaquette i, A_i is the current area of the plaquette after deformation. The summation of equations (4.41) and (4.42) gives the surface tension γ experienced at the node v. The coefficient of one third accounts for the share of the cn participating neighboring vertices.

4.3.6 Loading Rate Calculation and Accumulated Damage

Following Evans et al. [161] the loading rate for every element throughout the trajectory is determined directly from the change in calculated tension between successive simulation steps. Therefore, for every element at each time step, one of the equations (4.45b) or (4.45a) is used to obtain the rupture surface tension depending on the loading rate value. The rapid loading regime equation is straight forward to

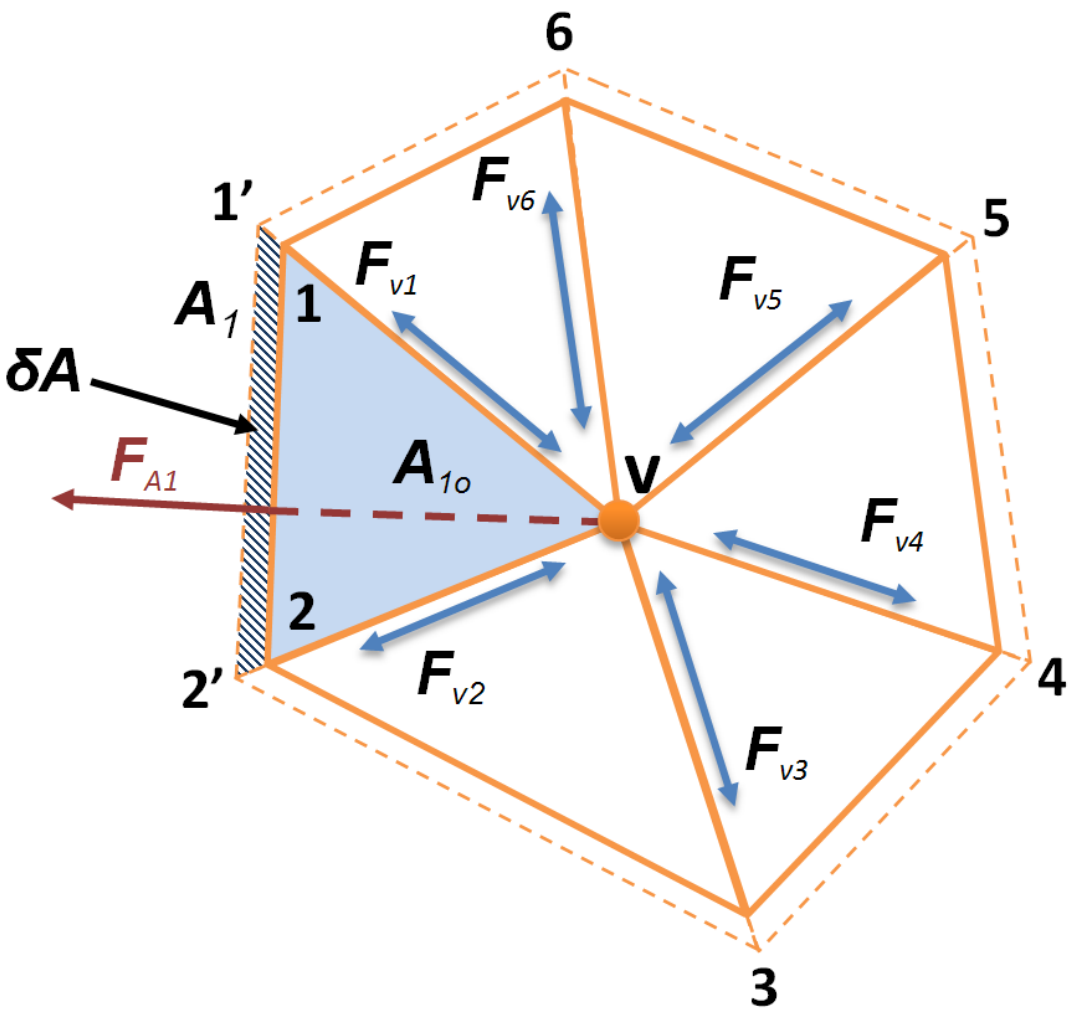

Figure 4.18: A schematic diagram for a general case where vertex v is associated with 6, inequivalent triangular, elements depicting the forces acting on vertex v, 1) due to pairwise interaction between the network vertices i.e., $F_{v1}, F_{v2}, ..., F_{v6}$, 2) resultant forces of the local and global area constraints, i.e. F_{A1}, due to an expansion area δA=$A_1 - A_{1o}$.

use, while the slow rate equation is more complex. Therefore the slow rate regime data was fitted with a 4^{th} order polynomial to simplify the process of obtaining the rupture tension corresponding to a certain loading rate. It is important to note that due to the discrete nature of the RBC model not all the nodes will undergo the

same loading state nor behave the same. Every node will be affected by the state of the neighboring nodes. This means that at each time step a fraction of the nodes is subjected to tension and another will be either compressed or experiencing no loading. Thus, inspecting the local tension allover the membrane surface is using the following procedure. First, by calculating the surface tension $\gamma(t)$ at each node, only the nodes that has positive tension are considered (nodes under compression are ignored). Second, for the nodes of interest the loading rate $\Re_\sigma$ is calculated, using equation (4.43), by finding the difference in tension divided by the difference in time between current and previous time steps.

$$\Re_\sigma = \frac{\gamma(t_i) - \gamma(t_{i-1})}{t_i - t_{i-1}}, \tag{4.43}$$

where i and $i-1$ refer to current and previous instances in time, respectively.

A new measure for accumulated damage D_{M-tot}, equation (4.44), is introduced here. It is based on the fractional damage D_{M-i}, where D is the ratio between the increment in tension $\Delta\gamma$ over the time step i divided by the rupture tension γ_r calculated for the same time interval i.

$$D_{tot} = \Sigma_{i=1}^{N} \frac{\Delta\gamma}{\gamma_r} \tag{4.44}$$

Defect-limit (high loading rate):

$$\frac{\gamma}{\gamma_\delta} \approx \mathrm{Log_e}\left(\frac{\Re_\gamma}{\upsilon_{0\delta}\gamma_\delta}\right) \tag{4.45a}$$

Cavitation-limit (slow loading rate:

$$-\frac{\gamma_c}{\gamma} + \mathrm{Log_e}\left[\frac{(\gamma/\gamma_c)^{5/2}}{(1+\gamma/2\gamma_c)}\right] \approx \mathrm{Log_e}(\frac{\Re_\gamma}{\nu_{\delta c}\gamma_c}) \tag{4.45b}$$

4.3.7 Local Curvature Calculation

The local mean Gaussian curvature κ at each vertex was calculated using a quadric fitting method in detailed in Petitjean [163]. Briefly, at each point of interest a local frame is positioned with the z-coordinate aligned with the normal at this point. Afterwards, the points in the local neighborhood of the point of interest were fitted using a quadric. Then, the curvature of that quadric is taken to be the estimate of the curvature for the nodes forming this discrete surface. The local Gaussian mean curvatures were calculated by post-processing the coordinates of RBC at specified points in time along the trajectory (see Appendix C).

4.3.8 RBC-RBC interaction

Neu and Meiselman [145] proposed a theoretical model to calculate the interaction energy ϕ_I between two cells using the depletion-mediated model. In their model only the depletion and electrostatic forces are considered. The exterior surface of RBC,

termed glycocalyx, is a complex layer of proteins and glycoproteins as shown in figure (4.19) and bears a net negative charge. Thus any two approaching RBCs sterically repel each other at a distance equal to twice the glycocalyx layer thickness $\sim$ 10 nm where a single layer of glycocalyx is $\sim$ 5 nm thick. Thus, the maximum affinity between two cells, minimal interaction energy, occurs at a distance more than twice the glycocalyx layer as shown in figure (4.17). As already stated, Neu and Meiselman [145] considered the total interaction energy as the summation of the depletion and electrostatic energies, namely;

$$\phi_I = w_{Dep} + w_E \tag{4.46}$$

$$w_{Dep} = -2\Pi \left(\Delta - \frac{d}{2} + \delta - p \right), \tag{4.47}$$

$$w_E = \frac{\sigma^2}{\delta^2 \varepsilon \varepsilon_o \kappa^3} \begin{cases} sinh(\kappa\delta)(e^{k\delta - \kappa d} - e^{-\kappa d}) & d \geq 2\delta \\ (2\kappa\delta - \kappa d) - (e^{-\kappa\delta} + 1)sinh(\kappa\delta - \kappa d) - sinh(\kappa\delta)e^{\kappa d} & d < 2\delta \end{cases} \tag{4.48}$$

where Π is the osmotic pressure, Δ is the depletion thickness layer, d separation between adjacent surfaces, δ is the thickness of attached polymer layer. κ^{-1} is the Debye-Hückel length.

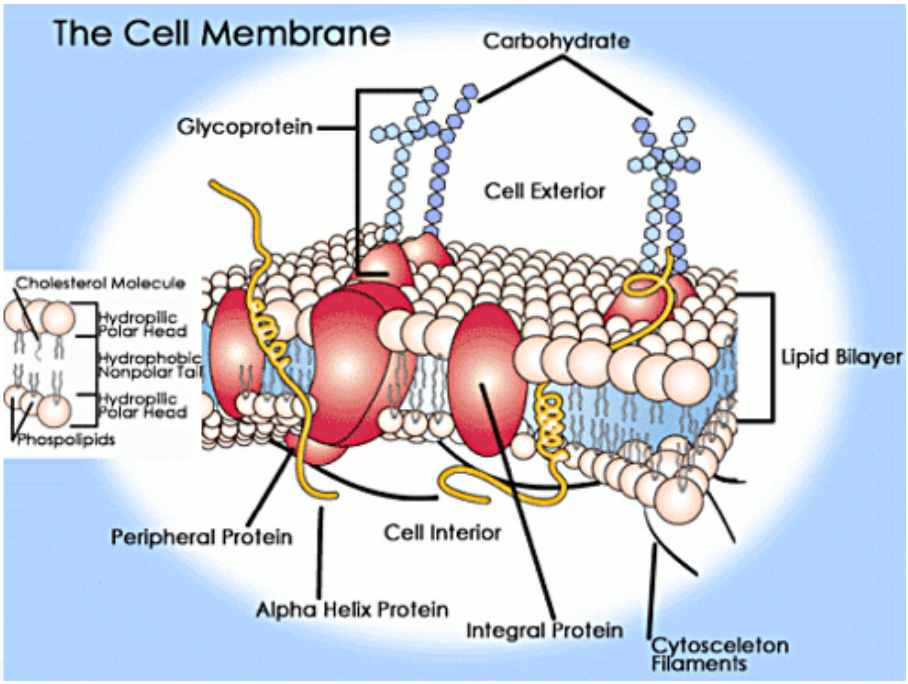

Figure 4.19: Glycocalyx, the cell coat, consisting of glycoproteins and oligosaccharides. Taken from (http://www.sparknotes.com/biology/cellstructure/cellmembranes/section2.rhtml

Neu and Meiselman [145] compared their theoretical model with cell-cell affinities experimental data. Good agreement with the experiments was found.

A similar approach will adopted in this work, although, the cell-cell interactions will be discretized in our simulations. Therefore, in the event of two approaching cells, a threshold distance is set for the proximal points belonging to different cells before they can interact. In other words, if two nodes from adjacent surfaces lie within the preset distance, an additional force is added to each of the interacting nodes. The magnitude of the force is correlated to the average area each node occupies on the RBC surface. This average area is determined at the beginning

of the simulation, where the total surface area is distributed amongst the number of nodes in the RBC model. The simplicity of this approach constrains us to use a single model for the RBCs in our simulation. This means that in the case of considering both healthy and diseased RBCs together in one system, a different approach for detecting contact should be employed. However, this discretization approach will not affect the implementation of a variable connectivity simulation, in which the number of springs in a network might change, while its vertices remain the same. In this case the area per vertex would not change.

In our approach the threshold will be set as the summation of the glycocalyx thickness (10 nm) and the diameter of one RBC node, which is the diameter of a circle that has an area equal to the area occupied by each RBC node. An illustration is shown in figure (4.20), where the point on the top RBC is close (within the threshold) to another two nodes on the bottom RBC. Then, for example, the node on the top RBC, would experience two forces, each one acting along the vectors connecting it with the two bottom nodes. The value of each force depends on the distance between the two nodes. When the separation distance is known, the interaction energy and hence the force can be obtained the equations (4.49) & 4.50, provided by Neu and Meiselman [145], namely;

$$\phi_I(r) = D_e(e^{2\beta(r_o - r)} - 2e^{\beta(r_o - r)}), \tag{4.49}$$

$$f(r) = 2D_e\beta(e^{2\beta(r_o-r)} - e^{\beta(r_o-r)}), \tag{4.50}$$

where $\phi_I(r)$ and $f(r)$ are the interaction energy and interaction force per unit area, respectively. D_e is the energy at the zero force distance r_o, r is the RBC-RBC separation distance and β is a scaling factor.

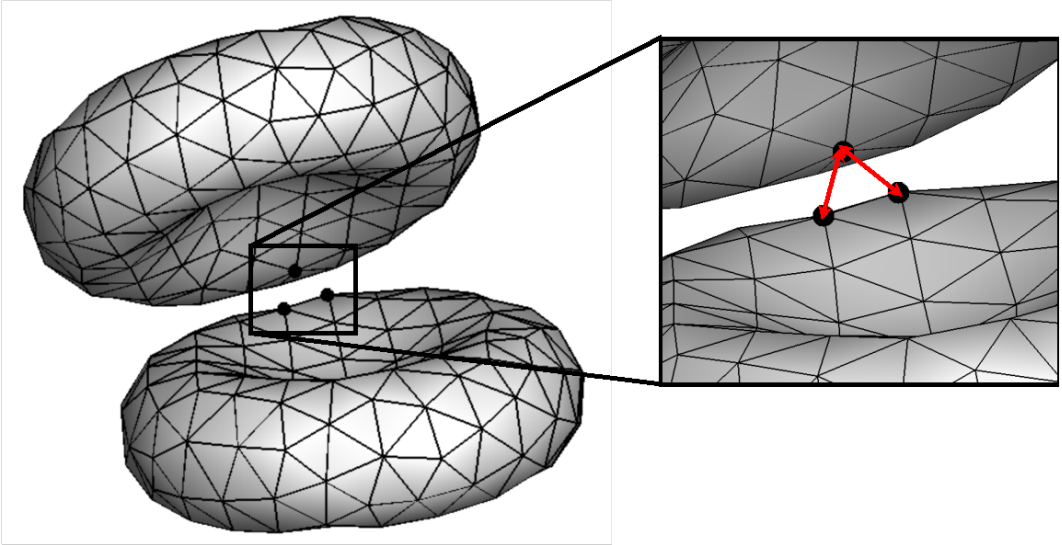

Figure 4.20: Schematic drawing of two RBCs in close proximity. The node on the top RBC lies within the threshold distance with respect to the two nodes on the bottom RBC.

4.4 Results

In this section, we start by presenting the verification for the DPD-RBC model through the stretching and recovery experiments. Then, we discuss the underlying physics of RBC deformation and hemolysis by the means of a set of numerical experiments. Finally, we conclude with the simulations of the RBCs through PHVs and the interpretation.

4.4.1 Stretching experiments

In the stretching experiments, the axial and transverse diameters are plotted against the stretching forces as shown in Figure 4.21. Also, the quality of the mesh is reflected in the local anomalies observed in the stretched RBC structure as shown in Figure 4.22 where buckling can be observed in the stretched mesh. Even though the axial diameter agrees with the experiments and Fedosov et al. [116] simulations, the topology of the stretched cell is not smooth as shown in [116].

4.4.2 RBC Relaxation

Another way verify the dynamics of RBC model we used in our work, we studied the RBC recovery through applying a stretching force and then observing the relaxation of the RBC after the release of the external force. The relaxation of the RBC was monitored under the application of the stretching force f, analogously to

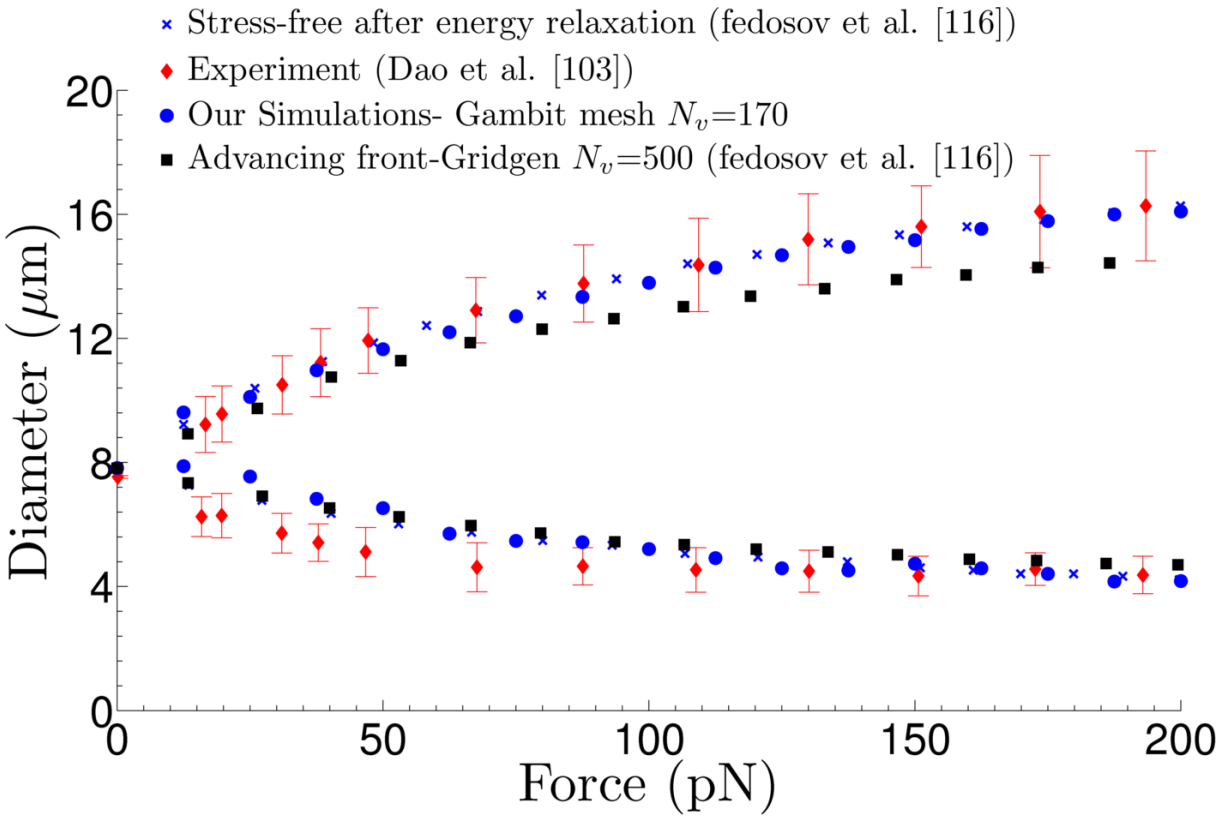

Figure 4.21: Stretching results from our code using the mesh generated by Gambit, $N_v = 170$, without energy relaxation, plotted together with the advancing front Gridgen mesh [116], $N_v = 500$, the same mesh with energy relaxation and the results obtained through OT [103] experiments

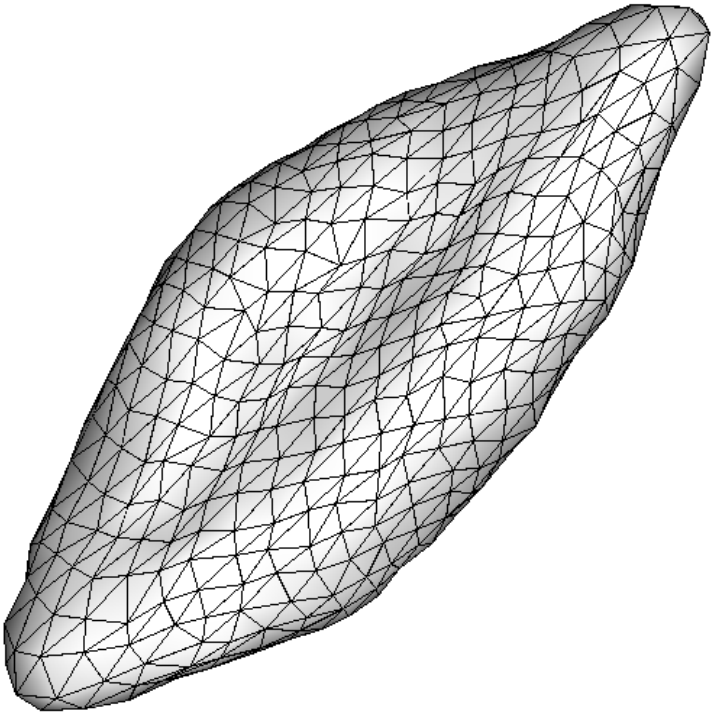

Figure 4.22: A RBC under a stretching force of 100 pN using a N_v=600 mesh. Image produced from our stretching experiment

that index introduced in ([164]), the time-dependent elongation index, $e(t)$ used as follows:

$$e(t) = \frac{(\lambda - \lambda_{\text{inf}})(\lambda_0 + \lambda_{\text{inf}})}{(\lambda + \lambda_{\text{inf}})(\lambda_0 - \lambda_{\text{inf}})} = \exp\left[-(\frac{t}{t_c})^{\delta}\right], \tag{4.51}$$

where $\lambda = D_A/D_T$, λ_0 and λ_{inf} correspond to the ratios at times $t = 0.0$ and $t = \text{inf}$, t_c is the characteristic time (known to be $\approx 0.1 \sim sec$ for RBCs, and δ is the exponent (Note that in ([164]) $\delta = 1$, and thus equation (4.51) is a generalization of the equation (11) in ([164]). In these recovery experiments the time scale exponent α was set to 0.75. Figure 4.23 shows the recovery of a RBC after deformation by a force of 7 pN with membrane viscosity $\mu_m = 0.022$ Pa.s. Different fits for a range of α and δ were explored (only the best two are shown).

4.4.3 Analysis of the Underlying Physics

As mentioned earlier, hemolysis is a multi-scale multi-dimensional process. It involves events spanning from a sub-second to days on the time scale and from nano-meters to centimeters on the length scale. Therefore, when studying hemolysis processes the length and time scale determine the methods that can be used and assumptions to be made. In this work, we are exploring the events taking place on the RBC length scale. As for the time scale, hemolytic processes can be divided into two phases, short-term and long term hemolysis. Since our main goal to enhance the design of heart assisted devices, specially PHVs, we are dealing with a

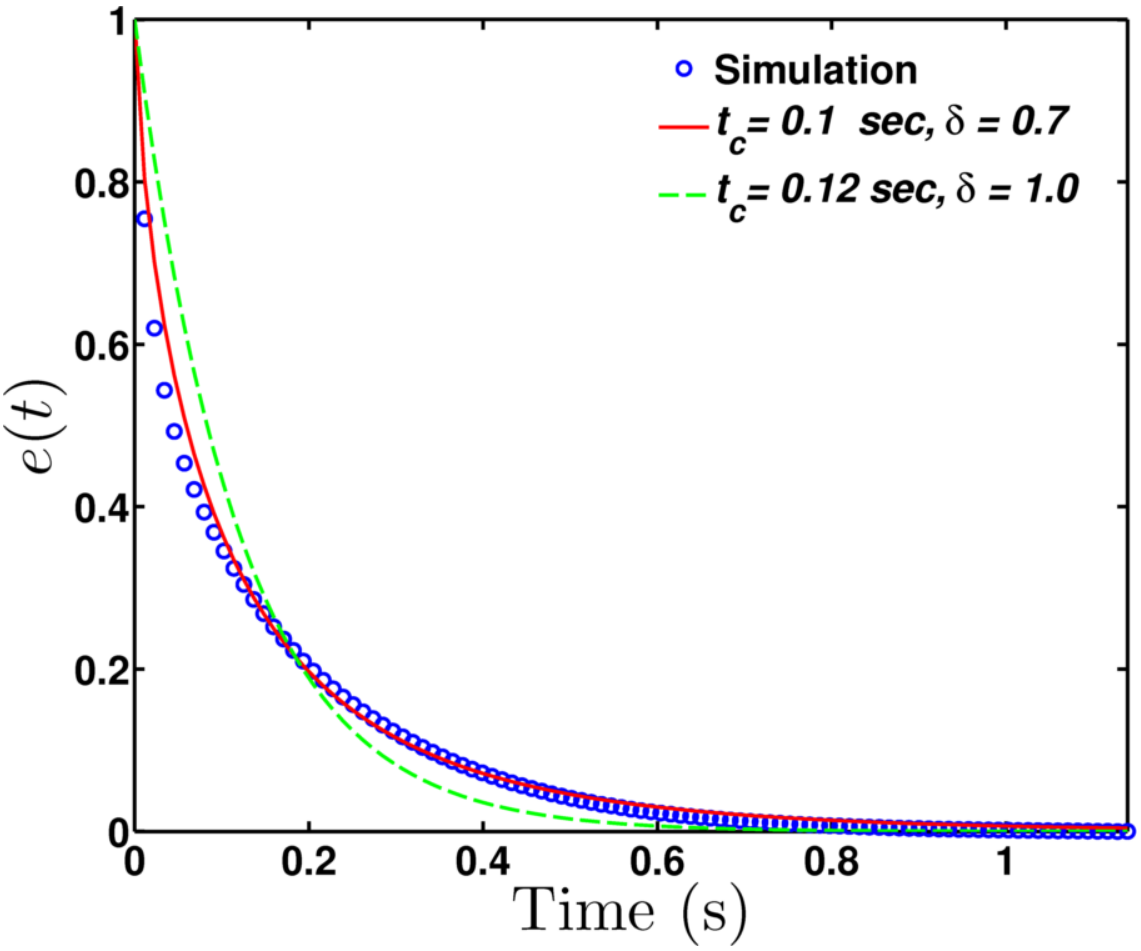

Figure 4.23: The elongation index $e(t)$ is plotted with time. Two fits are shown for different values of t_c and δ.

few cardiac cycles, which can be considered as the short-term hemolysis. At this phase, the damage is attributed to the surface tension magnitudes across the membrane, which differ from one location on the surface to another causing some areas to feel tension and others to experience compression, as illustrated by Figure 4.24 the surface tension average and standard deviation along one of the pathlines that we be discussed later in section 4.4.7. The applied tension cause the spontaneous pre-pores [161, 165] to evolve and create holes in the membrane. These holes consequently result in loss of the hemoglobin. Due to the complex composition of the RBC membrane, the exact magnitudes at which the membrane forms these holes is unknown. The complexity is compounded further by the dependence of the rupture tension on the rate of loading. This level of detailed information is not yet available for the RBC membrane. However, it is expected to be about half or less than the rupture tension of the pure lipid bilayers [161]. It worth mentioning that at a larger time scale ∼days, i.e. long-term hemolysis, another factor contributes to the damage, which is the cyclic nature of the load imposed on the RBCs during its life in the circulation. This cyclic nature of the load, i.e. *fatigue*, eventually leads to the damage of the spectrin network, which is referred to as aging [166]. The RBCs aging is manifested as the change in their material properties affecting their deformability and strength, however, these properties are assumed to be constant during the short-term hemolysis. Such assumption is supported by Discher et al. [122] fluorescence-imaged micro-deformation (FIMD) experiments that illustrated the solid-like behavior of the spectrin network, even when the RBC is under tension for a long periods of time (∼30 minutes).

Another important point to consider is the complexity of the flow field. All the hemolysis experiments, upon which the hemolysis models were based on, applied one-dimensional simple shear stresses. However, when breaking down a sample pathline, illustrating the trajectory of a RBC through a PHV, we can see the complexity of the flow field represented by the unequal magnitudes and frequencies of the different components of the velocity gradient tensor, as shown in Figure 4.25.

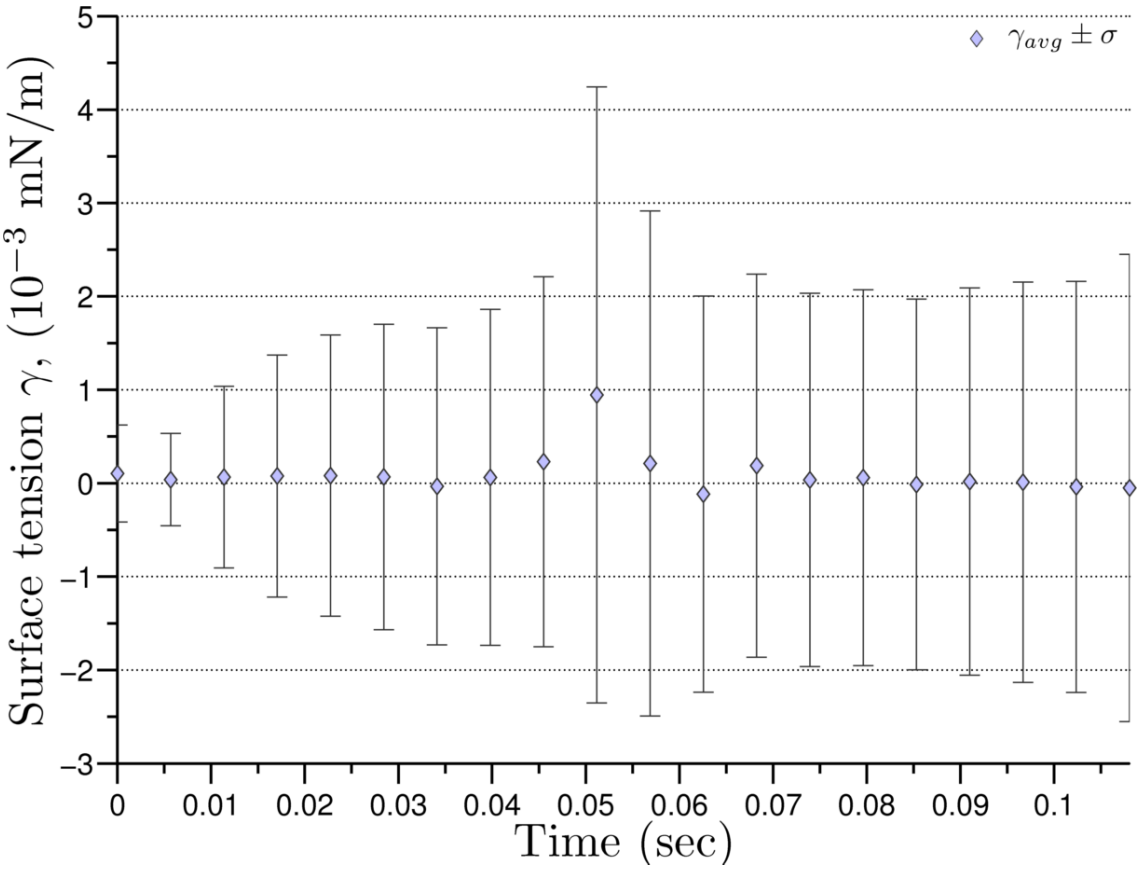

Figure 4.24: A box plot illustrating the distribution of surface tension magnitude and their standard deviation along one of the pathlines studied in section 4.4.7.

In the following sections, we analyze through a set of designed numerical experiments (see Table 4.1) the drawbacks of current hemolysis prediction models,

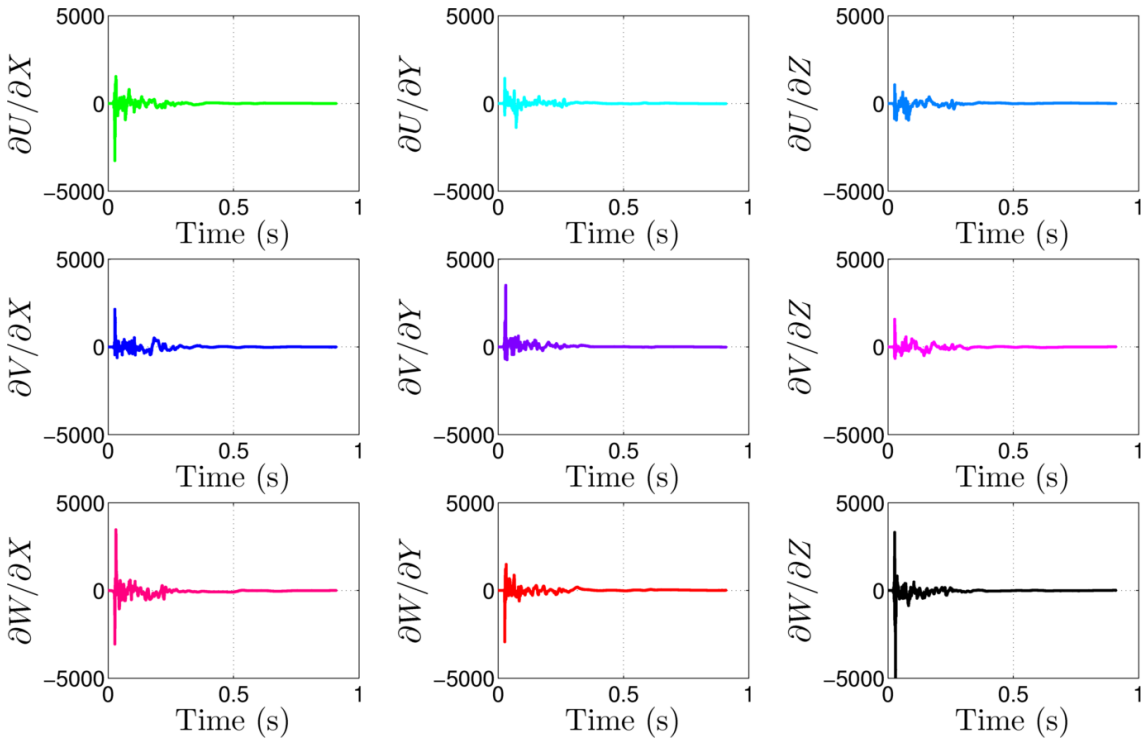

Figure 4.25: A plot of the velocity gradient tensor components for pathline C as discussed later in section 4.4.7

for example, which is more appropriate for predicting damage the stress-based or strain-based models. Also, the goal of these experiments to understand the difference between the macroscopic and microscopic models in predicting hemolysis and whether is there any advantages of using one over the other.

The loading conditions were altered through the velocity gradient tensor, ∇u, components. In each case, one or two components were set to non-zero value. In most of the cases the load has a sinusoidal form, $\partial u_i/\partial x_j = A_o sin(\omega t)$, where A_o is the magnitude of the shear rate, ω is the frequency, in rad/sec of the sinusoidal load, i and j could be x,y, or z. But, also in case no.5 the load is a step function. Table 4.1 gives a description for the non-zero components of the velocity gradient tensor in each case along with the values of their parameters.

Table 4.1: A description for the loading conditions for each case and the parameters defining each.

Case no.	Non-zero term(s)	Parameters
1	$\partial w/\partial x = A_o sin(wt)$	A_o=2000, $\omega = 10$ rad/s & $0 \leq t \leq 0.2$ sec
2	$\partial w/\partial x = A_o sin(wt)$	A_o=2000, $\omega = 100$ rad/s & $0 \leq t \leq 0.2$ sec
3	$\partial w/\partial x = A_o sin(wt)$	A_o=2000, $\omega = 1000$ rad/s & $0 \leq t \leq 0.2$ sec
4	$\partial v/\partial z = A_o sin(wt)$	A_o=2000, $\omega = 100$ rad/s & $0 \leq t \leq 0.2$ sec
5	$\partial w/\partial x = A_o$	A_o=0 & $0 \leq t \leq 0.05$sec A_o=0 & $0.05 \leq t \leq 0.2$ sec
6	$\partial u/\partial y = \frac{2}{3}A_o sin(wt)$ $\partial v/\partial x = \frac{1}{3}A_o sin(wt)$	A_o=2000, $\omega = 100$ rad/s & $0 \leq t \leq 0.2$sec A_o=2000, $\omega = 100$ rad/s & $0 \leq t \leq 0.2$sec

4.4.4 Fundamental Driving Force for Hemolysis

The main question is, what is the real driver of hemolysis? Is it a reasonable to assume that stresses cause damage instantaneously even if no strain has yet taken

place? The stress-based models relate the damage inflected on the RBCs to the imposed stresses, rather than the resultant strain. However, the visco-elasticity of the RBC membrane articulates the difference between the two approaches.

In this section, we examine the validity of the assumptions made in the stress-based models: 1) relating the damage of the RBC to the stress rather than the strain, in other words, whether stress is the correct indicator of damage, 2) abstracting the complex three-dimensional stress field into an effective scalar stress value (see appendix D). Hemolysis is quantified by the amount of hemoglobin released from the RBCs into the blood stream that is the result of the pores opening when the RBC membrane is under strain.

Therefore, in order to determine what is the accurate of indicator of damage, we examine the stress-strain relation of the RBCs. We start by comparing cases no.2 and case no.6. Shown in Figures 4.26a & 4.26b are the equivalent stresses used in the stress based models [110, 7], red curve, and the effective stresses (calculated from equation 4.40) used in the DPD-RBC model, blue curve. The equivalent stresses, τ_{eq}, are equal in both cases, but the strains are different, consequently the damage as shown in Figures 4.27a & 4.27b. This comparison shows how the stress-based models fail to determine the effect of the three-dimensional nature of the flow field. Additionally, we carried out a similar test between case no.2 and case no.4, where the same equivalent stresses were applied by different components of the velocity gradient tensor, however, the difference between this test and the previous one is

that the applied load was a simple one-dimensional shear. Interestingly, the damage in cases no. 2 and 4 are almost the same is

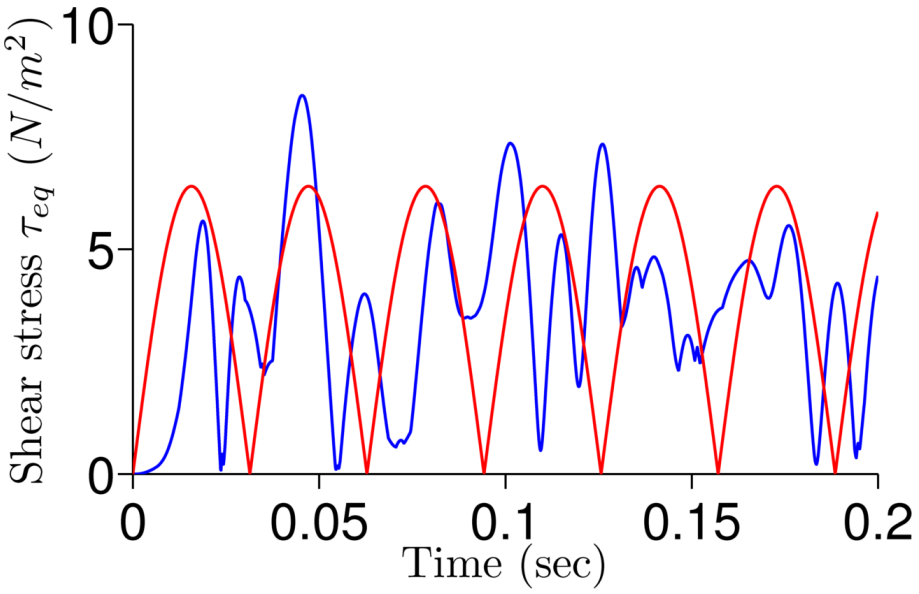

(a)

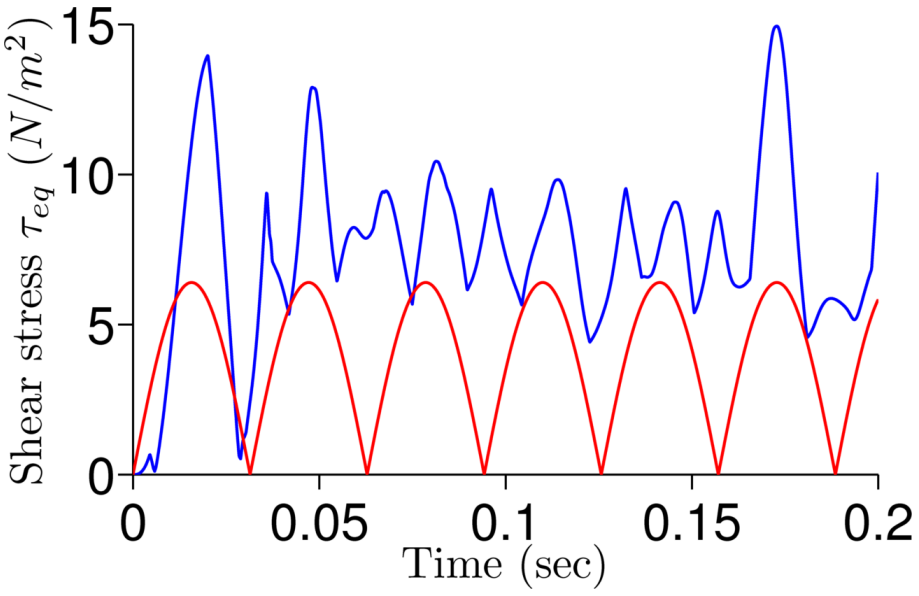

(b)

Figure 4.26: The effective stresses for two different sinusoidal loads, a) $\partial w/\partial x = 2000sin(100t)$, b) $\partial u/\partial y = \frac{2}{3}2000sin(100t)$, $\partial v/\partial x = \frac{1}{3}2000sin(100t)$. The equivalent stresses used in the stress-based are the solid-red curve, while the solid-blue curve represents the equivalent stresses for the DPD-RBC strain-based model.

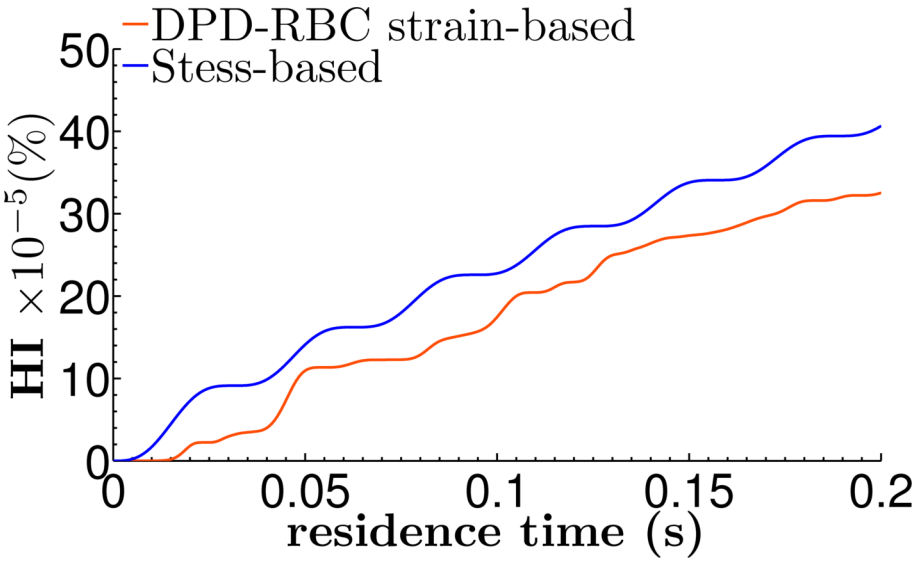

(a)

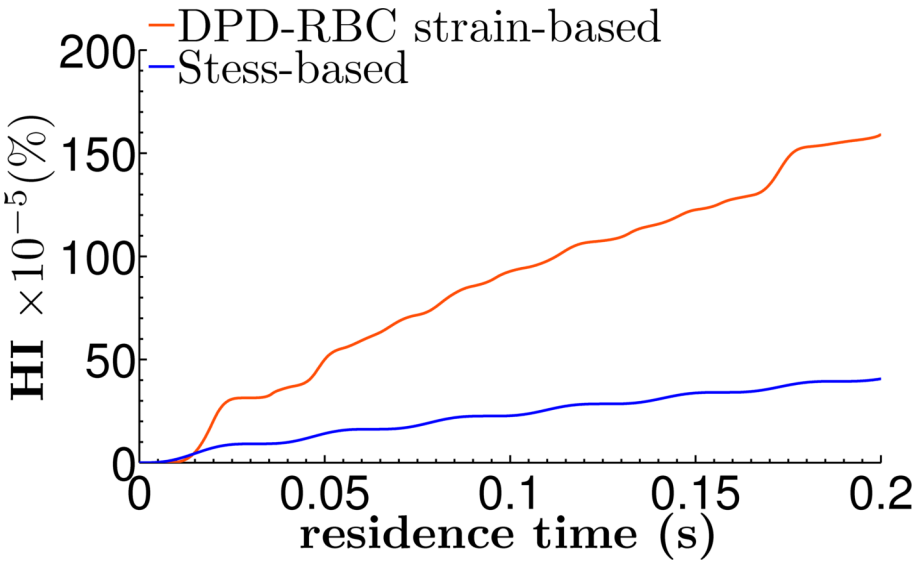

(b)

Figure 4.27: The blood damage index, BDI for cases no.2 and no.7. a) $\partial w/\partial x = 2000sin(100t)$, b) $\partial u/\partial y = \frac{2}{3}2000sin(100t)$, $\partial v/\partial x = \frac{1}{3}2000sin(100t)$. The damage predicted from the stress-based models is represented by the blue line, while the damage predicted by the DPD-RBC model is the orange line.

This is a test for the sensitivity of the stress-based models with regards to one-dimensional shear stresses. In this test two loading conditions produce the same equivalent stresses (used in the stress-based models [110]) and also the same effective stress (using the DPD-RBC model with equation (4.40)). The magnitude and frequency in both cases are equal, the difference is the non-zero component was $\partial w/\partial x$ in case no.3, shown in Figure 4.28a and $\partial v/\partial z$ in case no.4, shown in Figure 4.28b.

A second test, which emphasizes the importance of considering the rate of loading in the hemolysis model, was carried out to illustrate one of the major setbacks of the stress-based models [110]. Figure 4.29 shows the equivalent and effective stresses for cases no. 2 and 3, while Figure 4.30 shows the damage accumulated in both cases. The difference between the two cases is the frequency of the applied stresses. In case no.2 ω=100 rad/s, while in case no.3 ω=1000 rad/s. As shown in Figures 4.29a & 4.30b, the rate of loading has a significant effect on the RBC deformation and hence damage. The results of this test agree with the DTS experiments by Evans et al. [161], which showed that at higher frequencies of loading the magnitude of stresses required to cause damage also increases. Consequently, this test points to the weakness of the stress based models which extremely overestimates the damage in case no.3, while in fact almost no damage occurred as shown in Figures 4.30a & 4.30b.

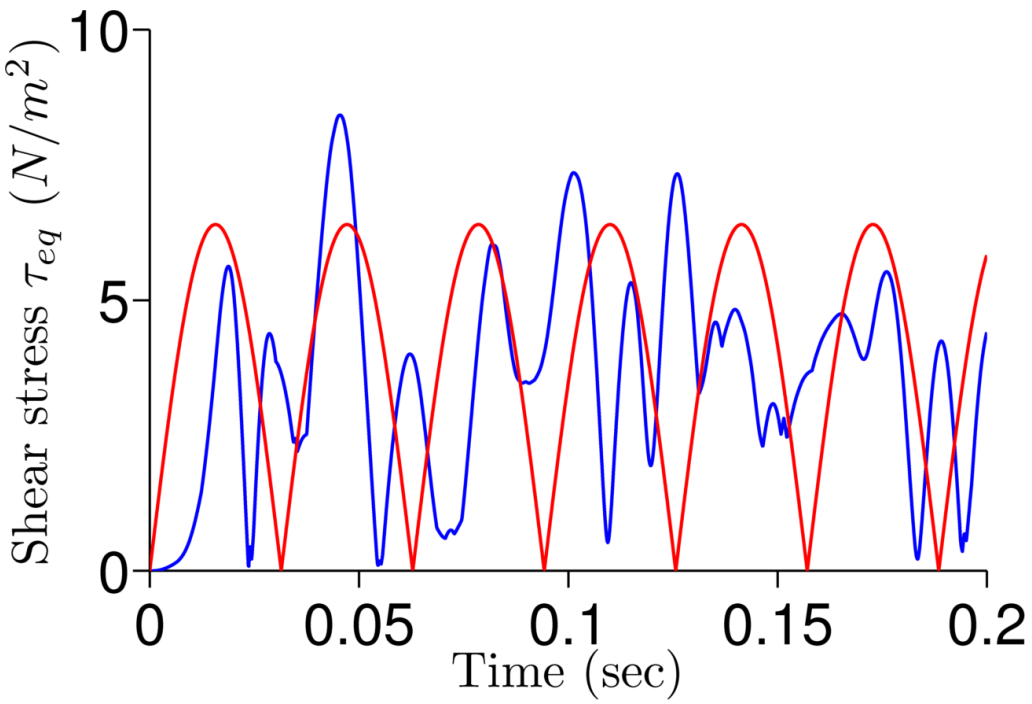

(a)

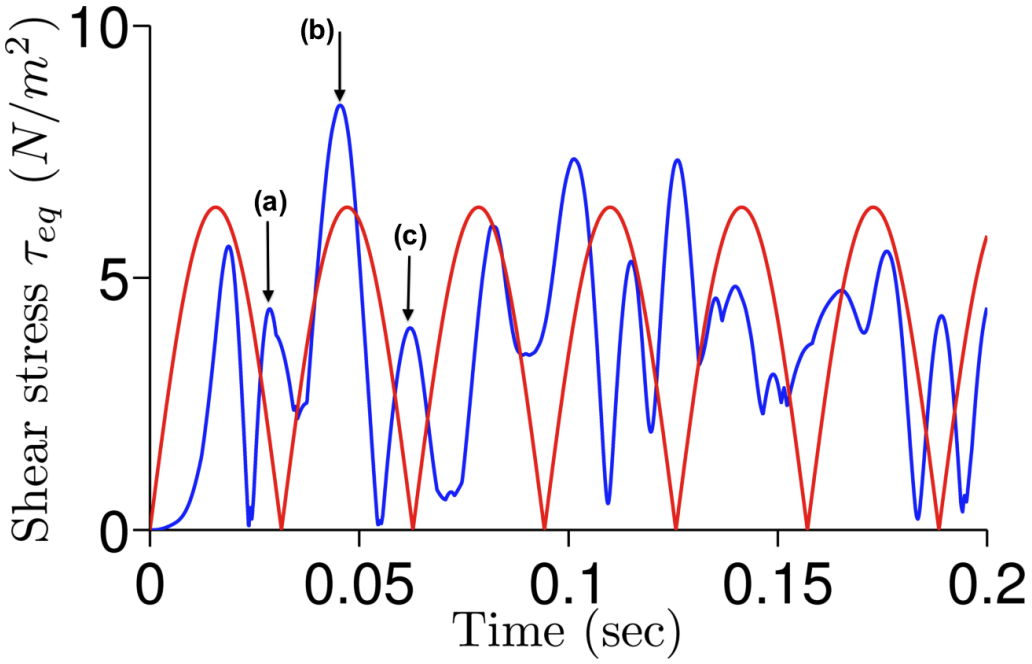

(b)

Figure 4.28: The effective stresses for two different sinusoidal loads representing cases no.2 and 6, a) $\partial w/\partial x = 2000sin(100t)$, b) $\partial v/\partial z = 2000sin(100t)$. The equivalent stresses used in the stress-based are the solid-red curve, while the solid-blue curve represents the equivalent stresses for the DPD-RBC strain-based model.

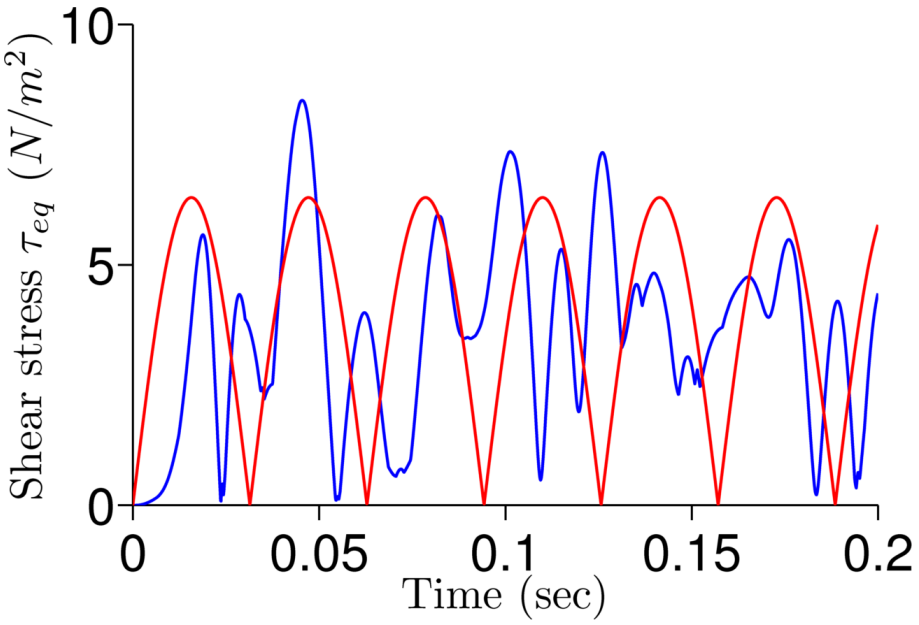

(a)

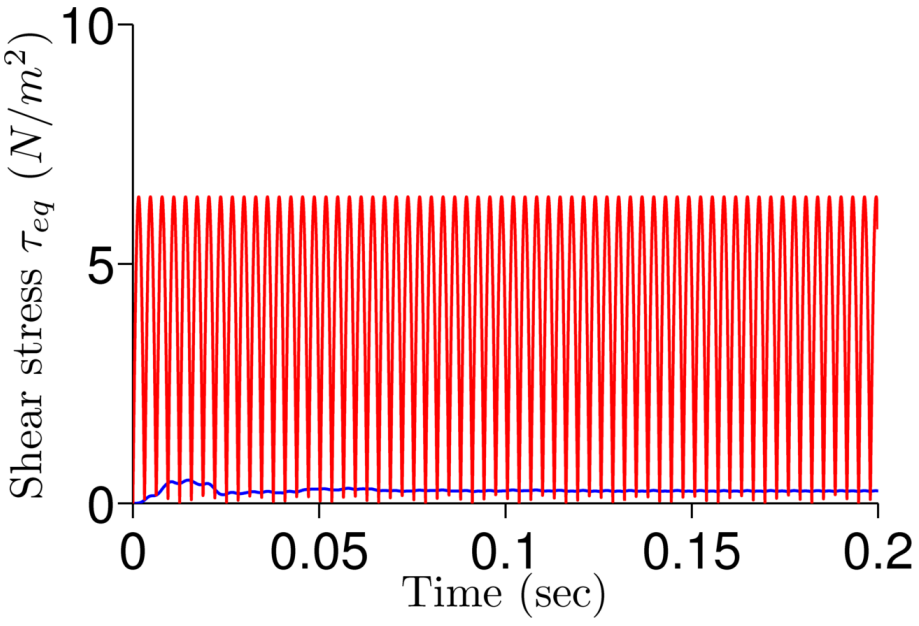

(b)

Figure 4.29: The effective stresses for two different sinusoidal loads, a) $\partial w/\partial x = 2000sin(100t)$, b) $\partial w/\partial x = 2000sin(1000t)$. The red curve represents the equivalent stresses used in the stress-based, while the blue curve represents the equivalent stresses for the DPD-RBC strain-based model.

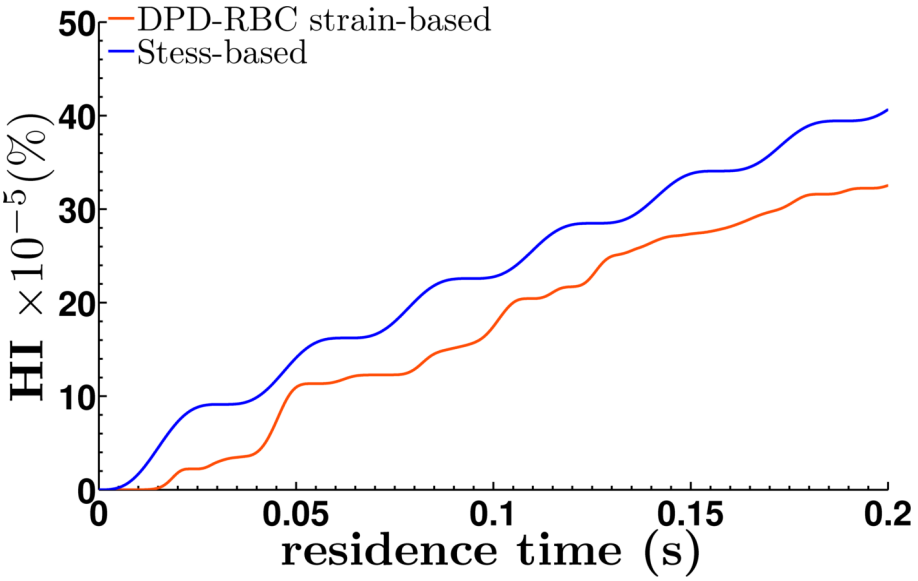

(a)

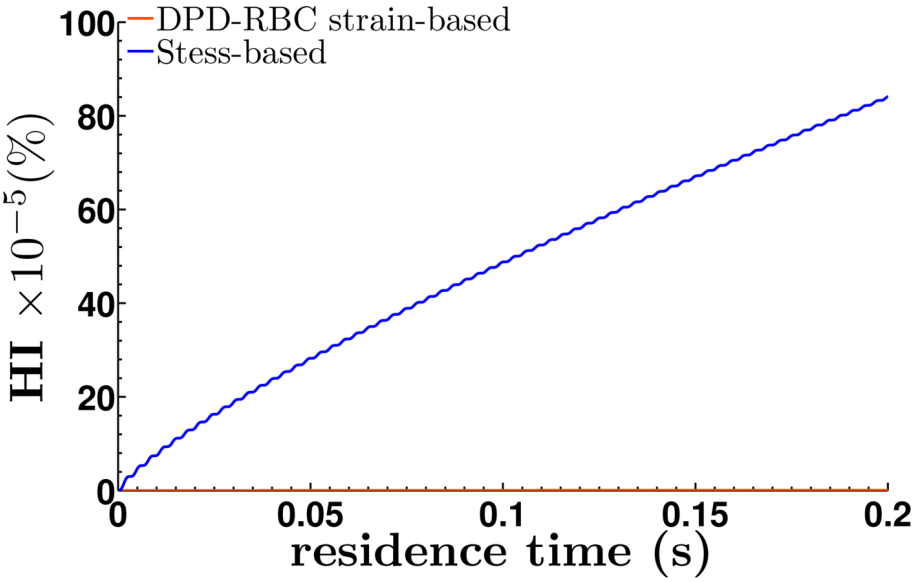

(b)

Figure 4.30: The blood damage index, BDI for cases no.2 and no.3. a) $\partial w/\partial x = 2000sin(100t)$, b) $\partial w/\partial x = 2000sin(1000t)$. The damage predicted from the stress-based models is represented by the blue line, while the damage predicted by the DPD-RBC model is the orange line.

The third test examines an important question regarding the orientation of the RBC with respect to the flow field. Two simulations we performed using the same loading conditions as in case no.2, but in one simulation the RBC was rotated 90° at the entrance. Figures 4.31a & 4.31b show the accumulated damage in the two cases is almost equal

4.4.5 Global versus Local Indicators of RBC Damage

In this section, we are exploring an important aspects of this study, which is whether damage predicted originates form the local damage and whether the global indicator such as ϕ, is the correct measure for damage. We will investigate this by analyzing the damage accumulated at different location across the membrane. This was achieved finding the locations of the maximum, minimum and maximum accumulated damage. For example, Figure 4.32, illustrates the change in surface tension along the trajectory of case no.2 for two locations on the RBC surface, the minimum and maximum accumulated damage in Figure 4.32a & 4.32b. It is clear from Figure 4.32 that the damage caused by the positive surface tension represented by the red shaded area increases in the right plot (location with maximum damage) compared to the left plot (location with minimum damage). Afterwards, the integral of the surface tension trajectory for each node is calculated, where the node with the largest integral resembles the location of maximum damage, as shown in Figure 4.33, where nodes are sorted by the integral that indicates the accumulated damage. In order to investigate the local deformation and consequently the damage, we used

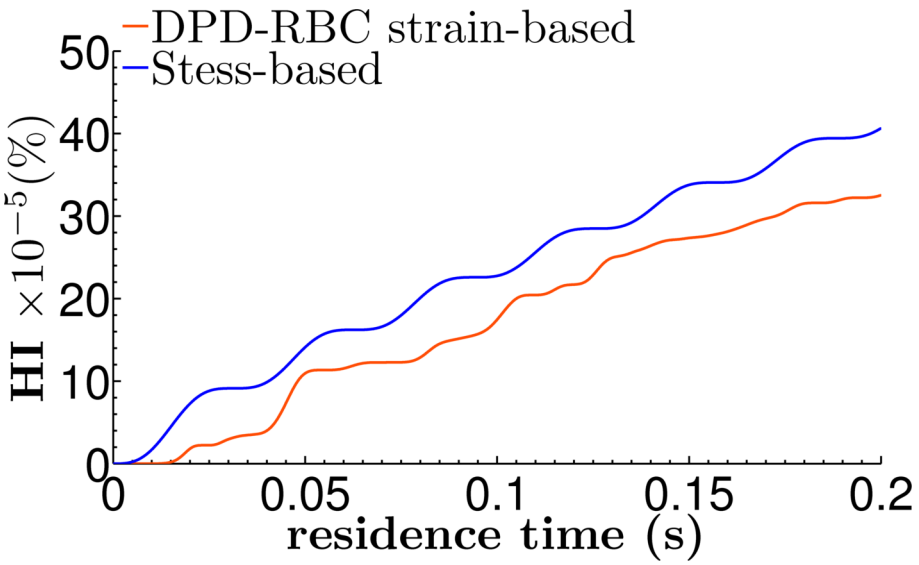

(a)

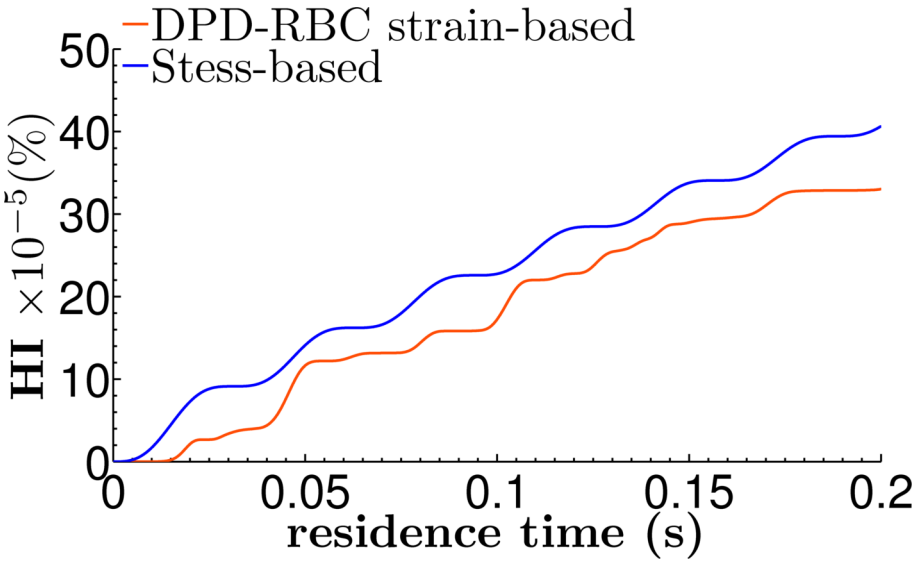

(b)

Figure 4.31: The blood damage index, BDI for case no.2, where $\partial w/\partial x = 2000sin(100t)$, for two RBCs with a orientations at the entrance.

the local distortion parameter, ϕ_L, as a local indicator for damage. Where each node has its own damage indicator, which is calculated from the nearest-neighbors forming a patch on the membrane. Therefore, the 1st nearest-neighbors of each individual node were used to obtain a local inertia tensor, which was then solved to obtain the eigenvalues for that specific area of the membrane. The average of the local deformation is expected to correspond to the global distortion ϕ_g.

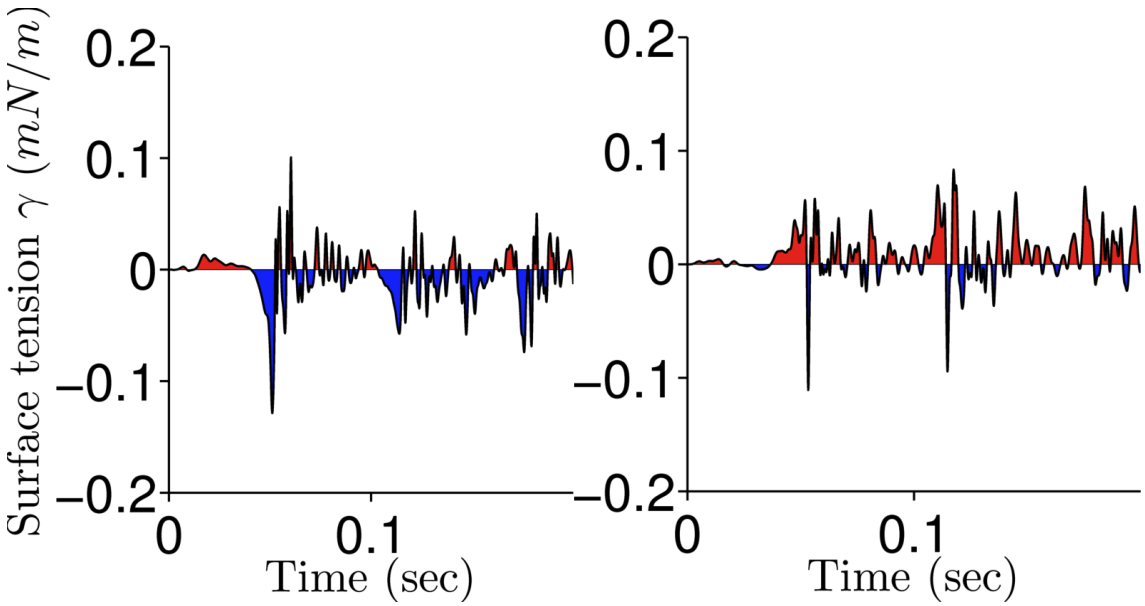

Figure 4.32: The surface tension trajectory for the locations of accumulated minimum damage (a) and maximum damage (b).

Shown in Figure 4.35 are the local distortion ϕ_{L-max} for maximum (blue curve) and ϕ_{L-avg} average accumulated damage (black curve) and the global distortion parameter ϕ_g (red curve). The Figure depicts that the average local distortion is greater than the global distortion parameter. First, we address the question whether we should inspect local damage indicators or the global measures are enough. To

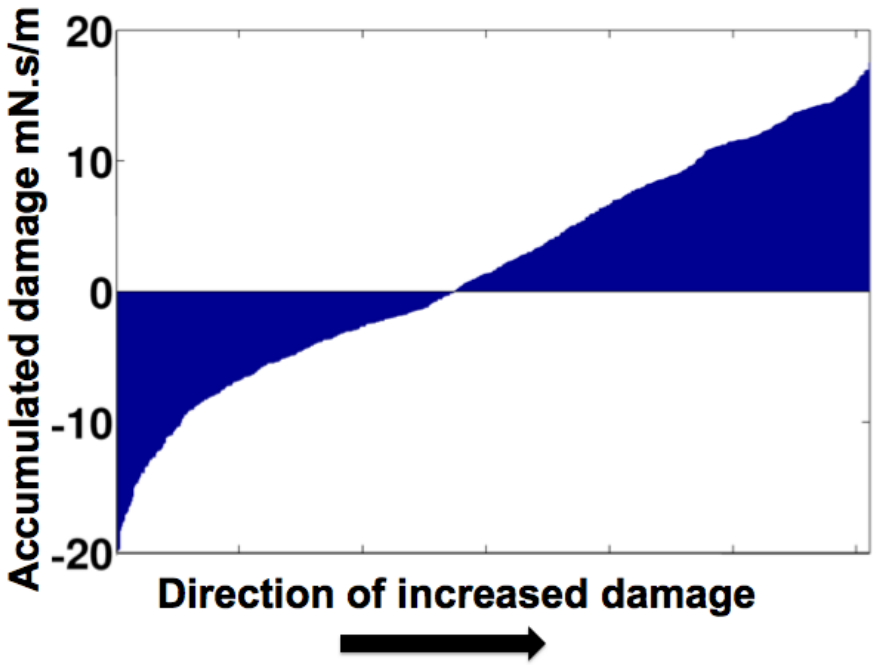

Figure 4.33: The accumulated damage (mN.s/m) for all the nodes representing the RBC surface (611 nodes).

answer this question, we check back the assumptions made in the first place to use the global distortion parameter, ϕ_g. Arora et al. [6] relied on the assumption that the RBC becomes ellipsoid and remains ellipsoid under shear stresses. Under this assumption two degrees of freedom were enough to represent the deformation of the RBC, which by the length of the axes of the ellipsoid. However, as shown in Figure 4.34 the RBC structure is not exactly an ellipsoid. It can be seen in Figure 4.34c, that the ellipsoid has dents in the sides. The distortion parameter ϕ_g is this case does not provide an accurate measure of the local strains on the RBC surface. In this case the local distortion parameter ϕ_L, like shown in Figure 4.36a & 4.36b, gives a better measure for the deformation of the RBC because it does not only consider the areal strain but also it accounts for the local curvature. Therefore, the defor-

mation and hence the damage predicted using the local distortion parameter will be more representative than just using the global distortion parameter. Nevertheless, the main challenge here is the lack of accurate experimental data that quantifies hemolysis, which we can use to validate the accuracy of the localized strain-based model approach presented above.

4.4.6 Physics of Hemolysis

The properties and hemolysis mechanisms of RBCs have been studied using a variety of experimental techniques, such as micropipette aspiration [167, 168, 169], flow through micropore membranes [170, 171], ultrasonic fragility studies [172] and osmotic shocks [173]. The results have led to various theories regarding hemolysis pathways, including colloid osmotic lysis, erythrophagocytosis, perforation of the membrane and fragmentation of corpuscles [174]. In this study, we focus on mechanically induced hemolysis in the context of prosthetic heart valves. We therefore do not consider colloid osmotic lysis, which is caused by cation disturbances across the membrane, nor erythrophagocytosis, which is caused by macrophages extracting coated RBCs from the blood stream.

In order to explore the most likely hemolysis pathway for RBC flowing through PHVs. we make use of the experimental findings [161, 170, 175, 165] to theorize whether hemolysis in PHVs is due to the perforation of the membrane or the fragmentation of the RBCs. To answer this question the local surface tension magnitudes

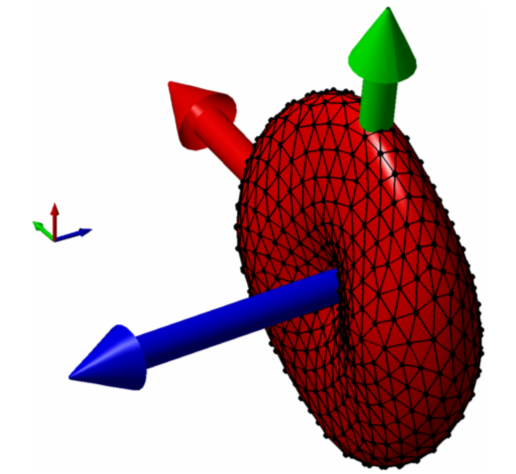

(a)

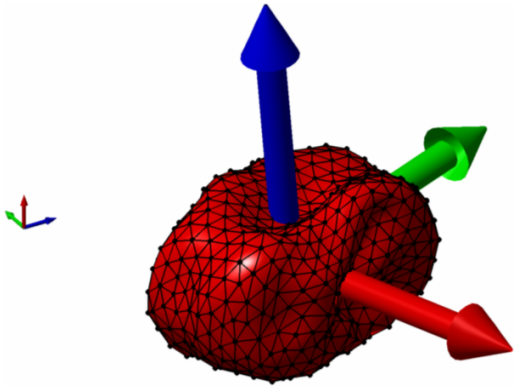

(b)

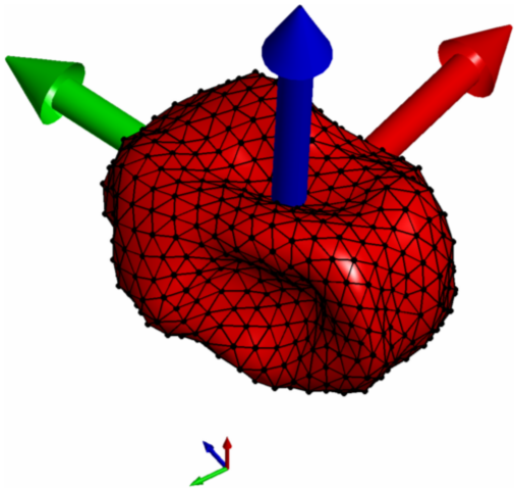

(c)

Figure 4.34: Snap shots of the RBC structure at the points marked a, b and c in Figure 4.28b.

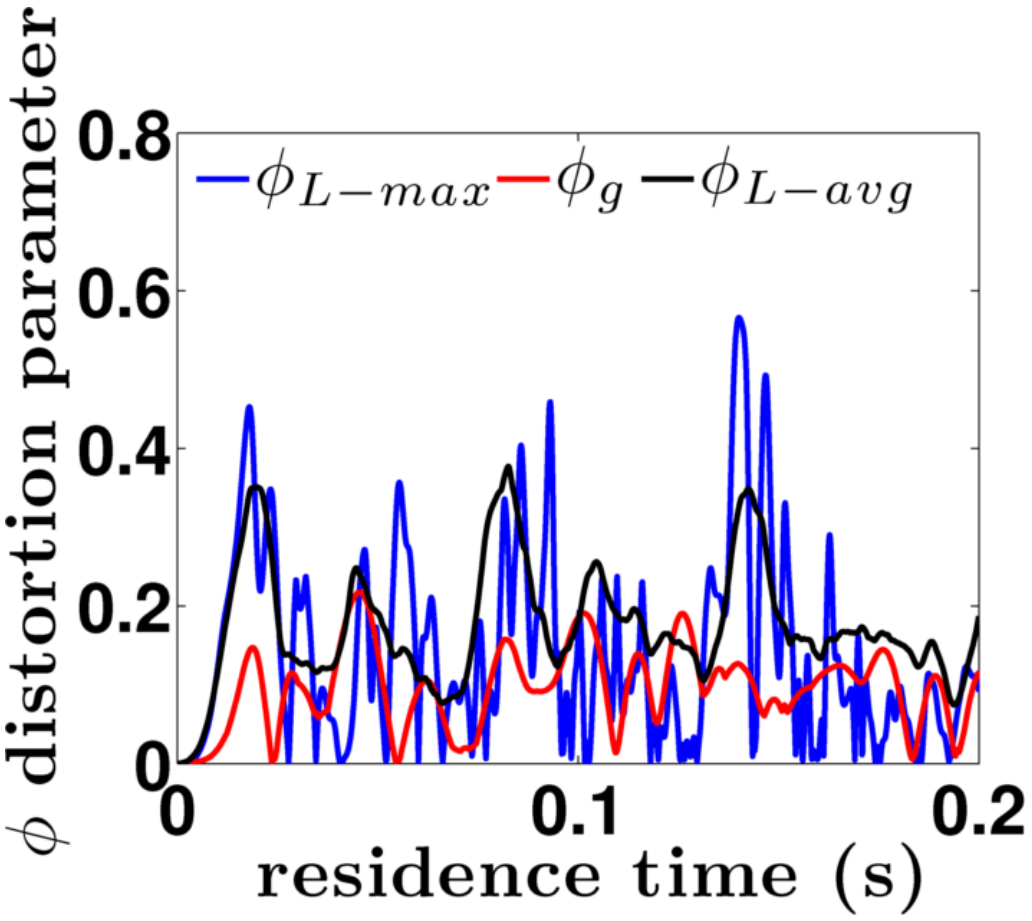

Figure 4.35: The local distortion parameter, ϕ_{l-max} for maximum accumulated damage (blue curve), average accumulated damage ϕ_{L-avg} (black curve) and the global distortion parameter ϕ_g (red curve).

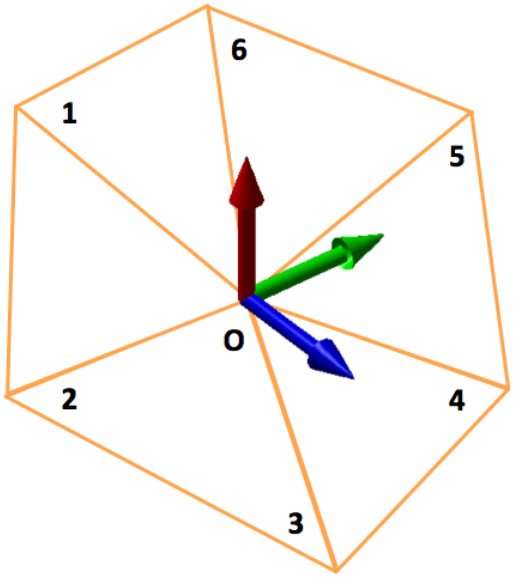

(a)

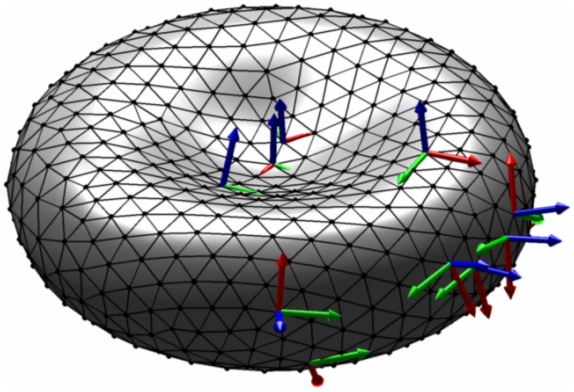

(b)

Figure 4.36: (a) The local eigenvectors representing the local distortion for node "O" surrounded by the 1st-nearest neighbors (vertices from 1 to 6), (b) an illustration of the local eigenvectors calculated at varies nodes on the RBC surface.

calculated from the hemolysis coarse-grained approach presented in this dissertation are compared to the calculated surface tension values required to rupture the RBC membrane. However, this is not trivial, due to the complexity of hemolysis processes and the lack of enough experimental data about the rupture tension values for RBC membranes. Therefore, we take the rupture tensions for pure lipid bilayers [161] as a qualitative reference. The magnitudes of local surface tensions calculated over the RBC surface were one order of magnitude less than the required tensions. Since there is no indication that a complete breakdown of the RBC structure (fragmentation hemolysis) is taking place during a single cardiac cycle, rather it suggests that pores open across the RBC membrane allowing hemoglobin to exit. Additionally, the filtration experiments by Chien et al. [170] and osmotic driven hemolysis experiments by Anderson et al. [173] show that the open pores in the membrane reseal rapidly, if the stresses were released in less than ~ 1 second, which is in the same order of the single heart beat. In other words, the life-time of the hydrodynamic stresses imposed by the PHVs on RBCs is insufficient to cause permanent damage to the structure. On the other hand, the level of stresses required to rapidly lysis RBCs into fragments lies in the range of 10^3-10^4 (Forstrom jet tests [176] and ultrasonic hemolysis [172]), which is two orders of magnitude higher than equivalent scalar stresses calculated for PHVs [177].Therefore, we conclude that is more likely that the hemolysis pathway for the RBCs flowing the PHVs under study is of the membrane perforation mechanism [174].

4.4.7 Simulation for a Real Device

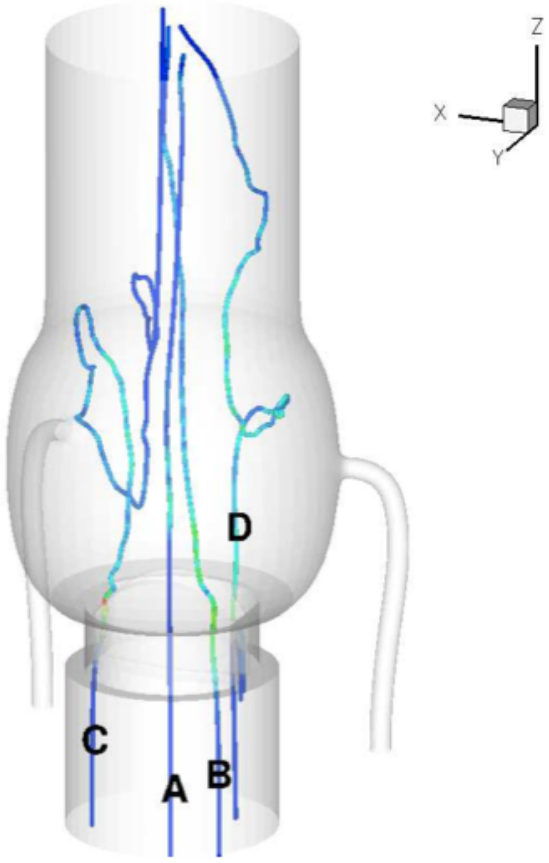

Figure 4.37: The four pathlines that are considered in this study.

In our study multi-scale simulation techniques were involved. First, CFD-FSI coupled simulations were conducted [177] to simulate a Newtonian fluid, with a blood equivalent viscosity, through an aortic prosthetic valve (St.Jude Medical Inc. Minneapolis), from which the flow domain was obtained. Then, the flow field solution was used to extract the velocity gradients tensor, ∇u, along the trajectories of massless particles. However, a countless number of trajectories could be sampled, a few interesting pathlines that RBCs undergo during their passage through the

heart were chosen. Figure 4.37 show the path of the four sample trajectories. They represent different scenarios for RBC passage through the aortic valve with varies residence times 0.108, 0.12, 0.9088 and 1.0304 seconds for the pathlines A, B, C and D, respectively. Obtaining and analyzing the deformation of the RBCs along these pathlines enable us to study the effect of hydrodynamic loading and if possible point out the flow conditions that causes damage to the membrane locally. An explicit and accurate representation of the RBC and its deformation states were attained using the mesoscopic model proposed by [116, 115]. The procedure followed starting from the pathline data to the hemolysis quantification is explained below.

Here we compare the strain-based hemolysis model relying on the DPD-RBC simulations output with the stress-based hemolysis model by Griespen et al. [110], equations (4.38), with the trajectories of the four sample pathlines were applied to the DPD-RBC model and the coordinates of the RBCs were used to calculate the eigenvalues of the RBC structure, hence the stresses felt by the RBC. Then the anticipated damage in both cases was compared. Figures 4.38-4.41 show the eigenvalues of the RBC structure (on top) and the scalar stresses for the different hemolysis models in equations (4.38), (4.39) & (4.40) (on bottom). Note that the droplet model used by Arora et al. [6] assumes a spherical shape (unity eigenvalues) prior to deformation. Since the actual undeformed RBC model has non-unity eigenvalues, the eigenvalues used in our calculations and plotted in Figures 4.38-4.41 are scaled to the initial eigenvalues of the RBC model (at t=0). Bottom of Figures 4.38-4.41 demonstrate the different measure of τ, the stresses experienced by the

RBC, calculated from the DPD-RBC model and from equation (4.40). There are discrepancies between τ calculated from the two techniques. First, the phase shift emphasizes the visco-elastic behavior of the RBC pronounced in the lag-time, in both loading and unloading cases, between the peaks of the two curves (solid gray and dashed blue). Second, the magnitude of the two curves is not the same all the time because the stress calculated from the double inner product of the stress tensor $\boldsymbol{\tau}$ (solid gray curve) neglects the actual shape of the RBC and the 3D nature of the problem. However, the application of the stress tensor $\boldsymbol{\tau}$ in the DPD-RBC simulations produces the correct deformation and reflects it in the distortion parameter ϕ (dashed blue curve). The evolution of the morphology tensor (the droplet model) used by Arora et al. [6] underestimates the deformation and hence the stresses.

Shown in Figures 4.42-4.45 are the hemolysis indices for four different models Giersiepen et al. [110] is the blue curve, Grigioni et al. [7] is the green curve, Arora et al. [6] is the magenta curve and RBC-DPD simulations is the orange curve. The strain-based hemolysis model using the morphology tensor to represent the RBC underestimates the damage in all of the four cases, while the damage predicted using the strain-based model (equation (4.40)) with RBC-DPD simulations shows a better agreement with the stress-based models (equation (4.38) and (4.39)), with slight difference in total accumulated damage. The damage predicted for pathlines C Figure 4.40 and D Figure 4.41 by the RBC-DPD simulation agrees more with Grigioni et al. [7] model, while not far from that of Giersiepen et al. [110]. Interestingly, for pathline B the stresses calculated and hence the predicted damage, using equa-

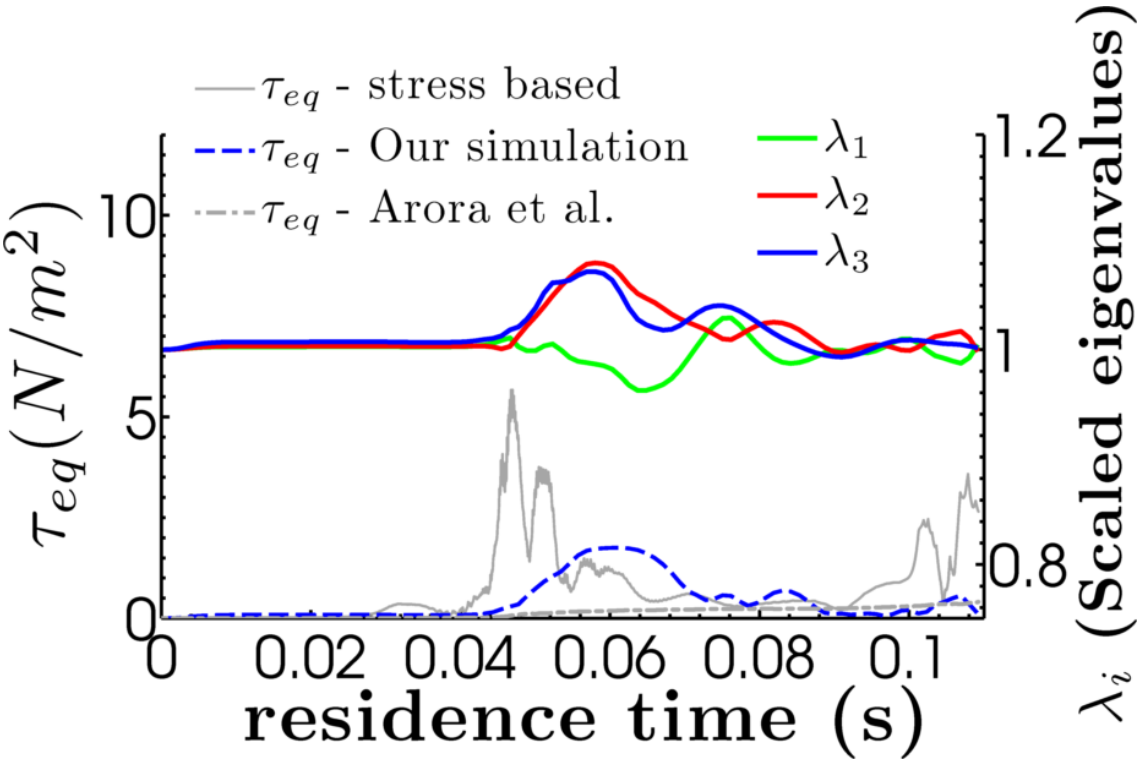

Figure 4.38: Pathline A: (Top) are the eigenvalues of the inertia tensor for the RBC coordinates along the trajectory. (Bottom) are the equivalent instantaneous stresses used to calculate the damage indices for the stress-based and the strain-based. The solid-gray line gives τ in equations (4.38) & (4.39), the dashed-gray line for Arora et al. [6] and the dashed-blue line from our simulations, where the last two stress were used in equation (4.40).

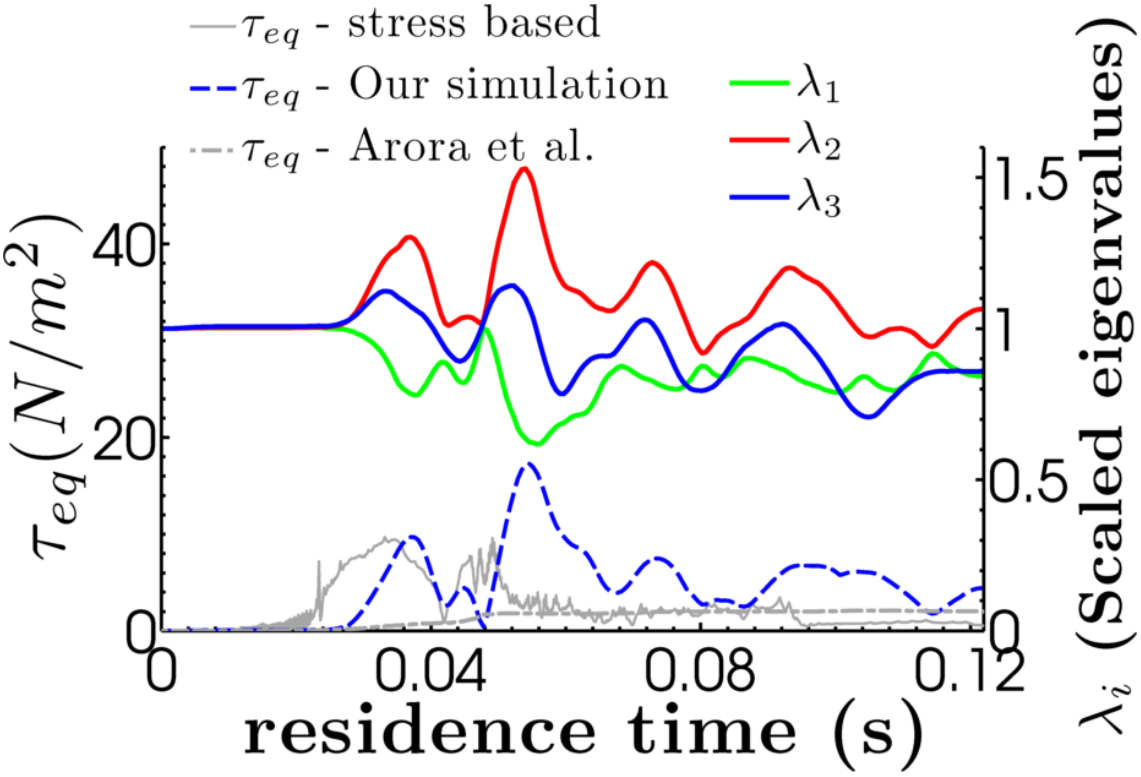

Figure 4.39: Pathline B: (Top) are the eigenvalues of the inertia tensor for the RBC coordinates along the trajectory. (Bottom) are the equivalent instantaneous stresses used to calculate the damage indices for the stress-based and the strain-based. The solid-gray line gives τ in equations (4.38) & (4.39), the dashed-gray line for Arora et al [6] and the dashed-blue line from our simulations, where the last two stress were used in equation (4.40).

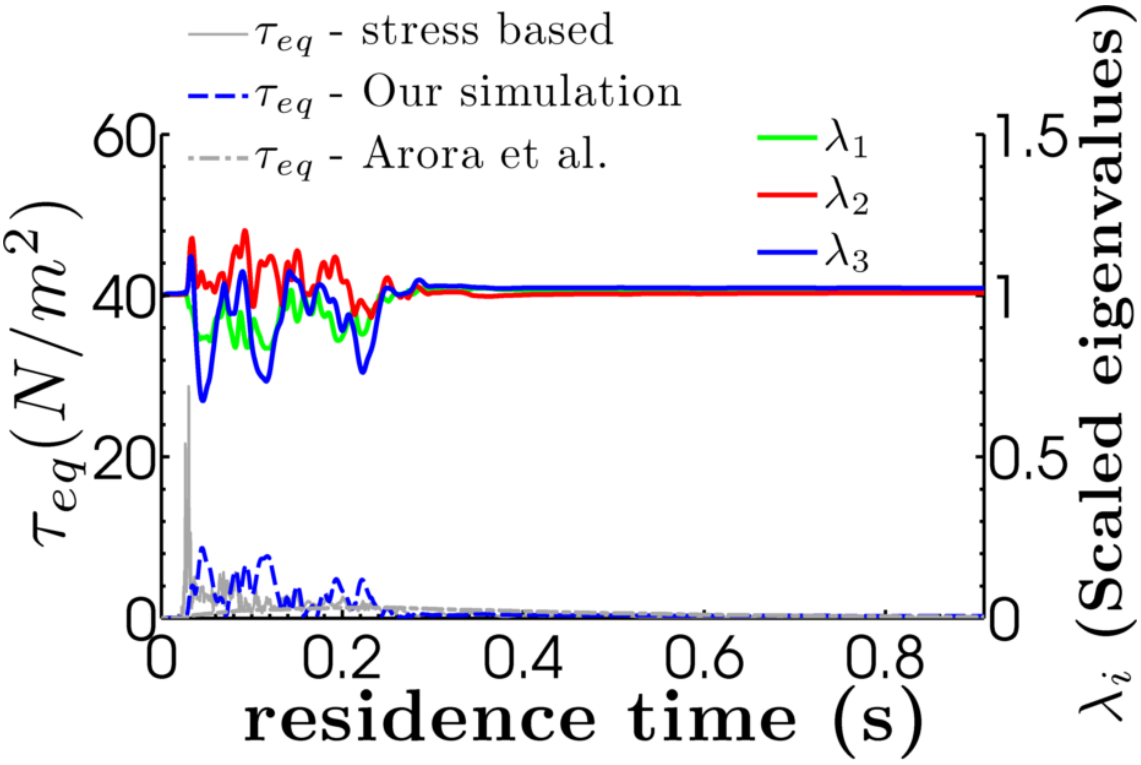

Figure 4.40: Pathline C: (Top) are the eigenvalues of the inertia tensor for the RBC coordinates along the trajectory. (Bottom) are the equivalent instantaneous stresses used to calculate the damage indices for the stress-based and the strain-based. The solid-gray line gives τ in equations (4.38) & (4.39), the gray-dashed line for Arora et al. [6] and the blue-dashed line from our simulations, where the last two stress were used in equation (4.40).

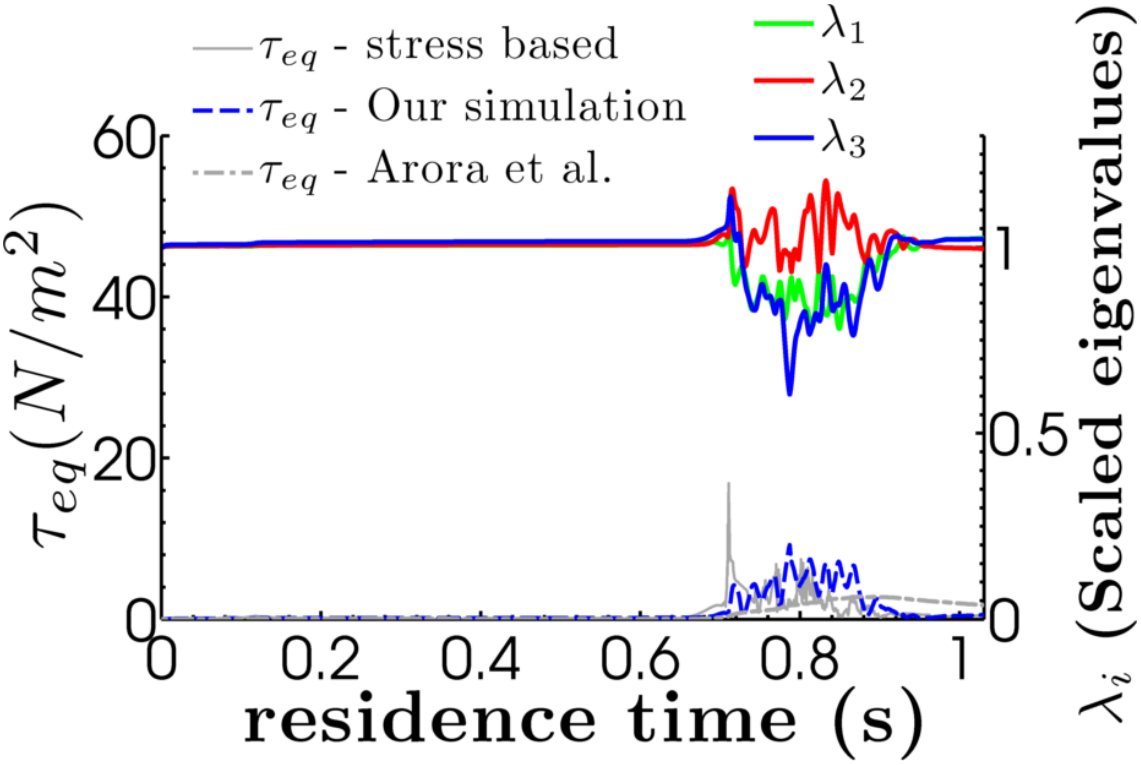

Figure 4.41: Pathline D: (Top) are the eigenvalues of the inertia tensor for the RBC coordinates along the trajectory. (Bottom) are the equivalent instantaneous stresses used to calculate the damage indices for the stress-based and the strain-based. The solid-gray line gives τ in equations (4.38) and (4.39), the dashed-gray line for Arora et al. [6] and the dashed-blue line from our simulations, where the last two stress were used in equation (4.40).

tion (4.40), for the RBC-DPD simulation are overestimated compared to Giersiepen et al. [110] equation (4.38). This case clearly demonstrate the complexity and the three-dimensional nature of the problem in hand. Although the maximum stresses in pathline B are less than that reached in cases C and D and the residence time for pathline B is about five times smaller than that of pathline C and D, yet the accumulated damage for case B exceeds that in C and D by about 25% and 30%, respectively. The deformation history of a RBC along the pathlines is the reason for the convoluted deformation, meaning that a combined effect due to the application of stresses to the deformed RBC structure result in predicting more damage than the stress-based ones, where the damage is equated from an undeformed RBC structure. Also, an important difference between the RBC-DPD predicted damage (orange curve) and the stress-based models (blue and green curves) is the gradual accumulation of damage in the case of the RBC-DPD simulations as compared to that of the stress-based models, where an instantaneous damage was predicted upon applying an external load.

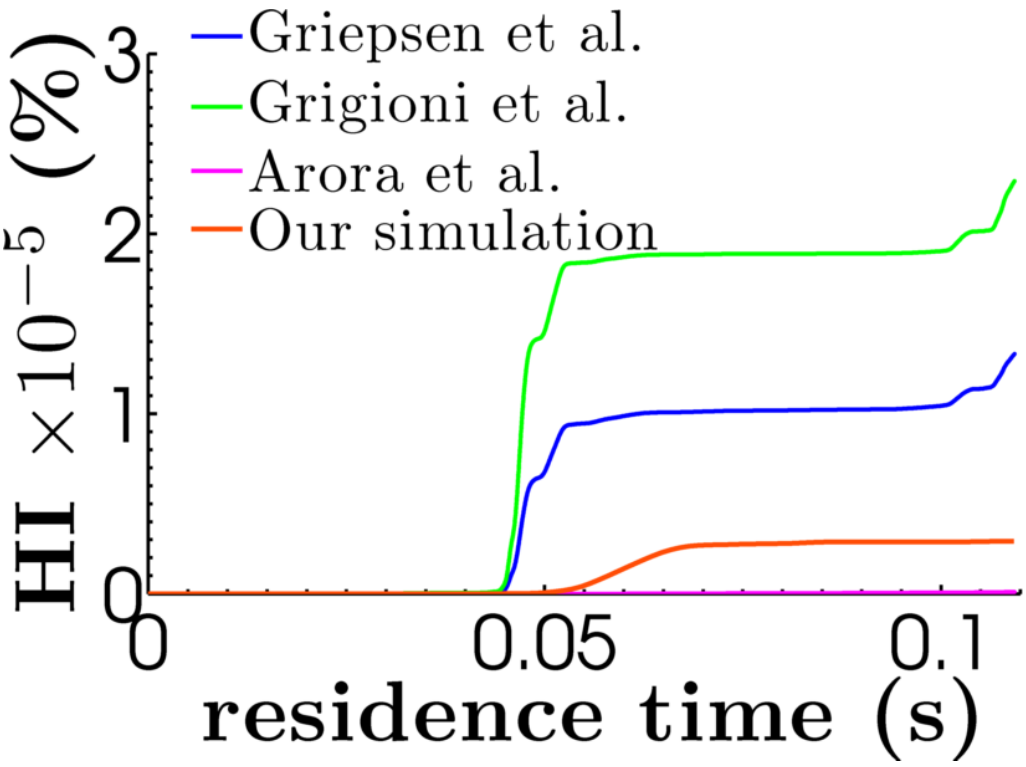

Figure 4.42: Pathline A: The accumulated damage evaluated using four models, Giersiepen et al. [110] equations (4.38), Grigioni et al. [7] equation (4.39), Arora et al. [6] equation (4.40) and the strain-based damage model using the inertia tensor for the RBC coordinates.

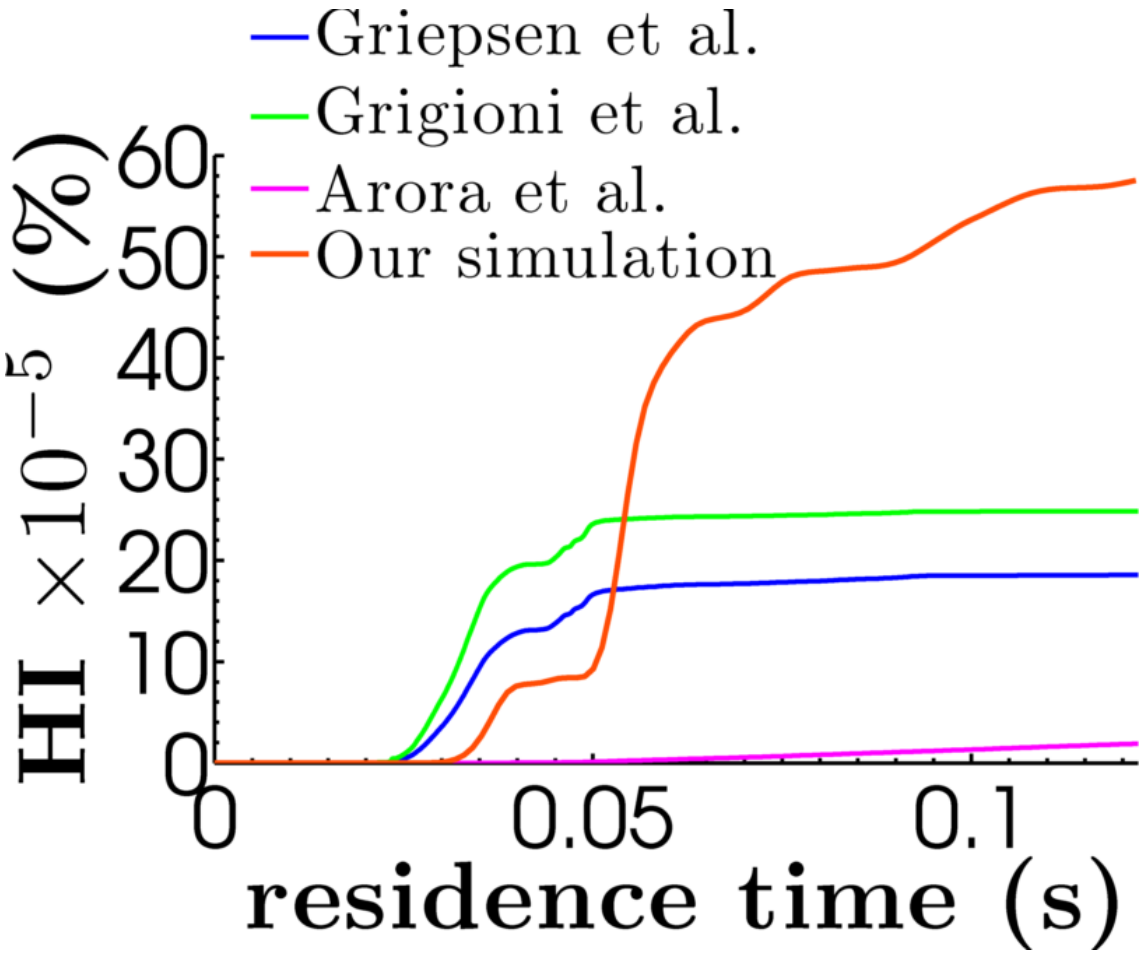

Figure 4.43: Pathline B: The accumulated damage evaluated using four models, Giersiepen et al. [110] equations (4.38), Grigioni et al. [7] equation (4.39), Arora et al. [6] equation (4.40) and the strain-based damage model using the inertia tensor for the RBC coordinates.

Figures 4.46a-4.47b, show the molecular damage index D_{M-tot} for the four pathlines A-D. The top and bottom black curves indicate the lower and upper bounds of the accumulated damage, while the red curve shows the average damage. A good agreement between the accumulated molecular damage index and the strain-based RBC-DPD hemolysis index in terms of the functional form. Both indices realisti-

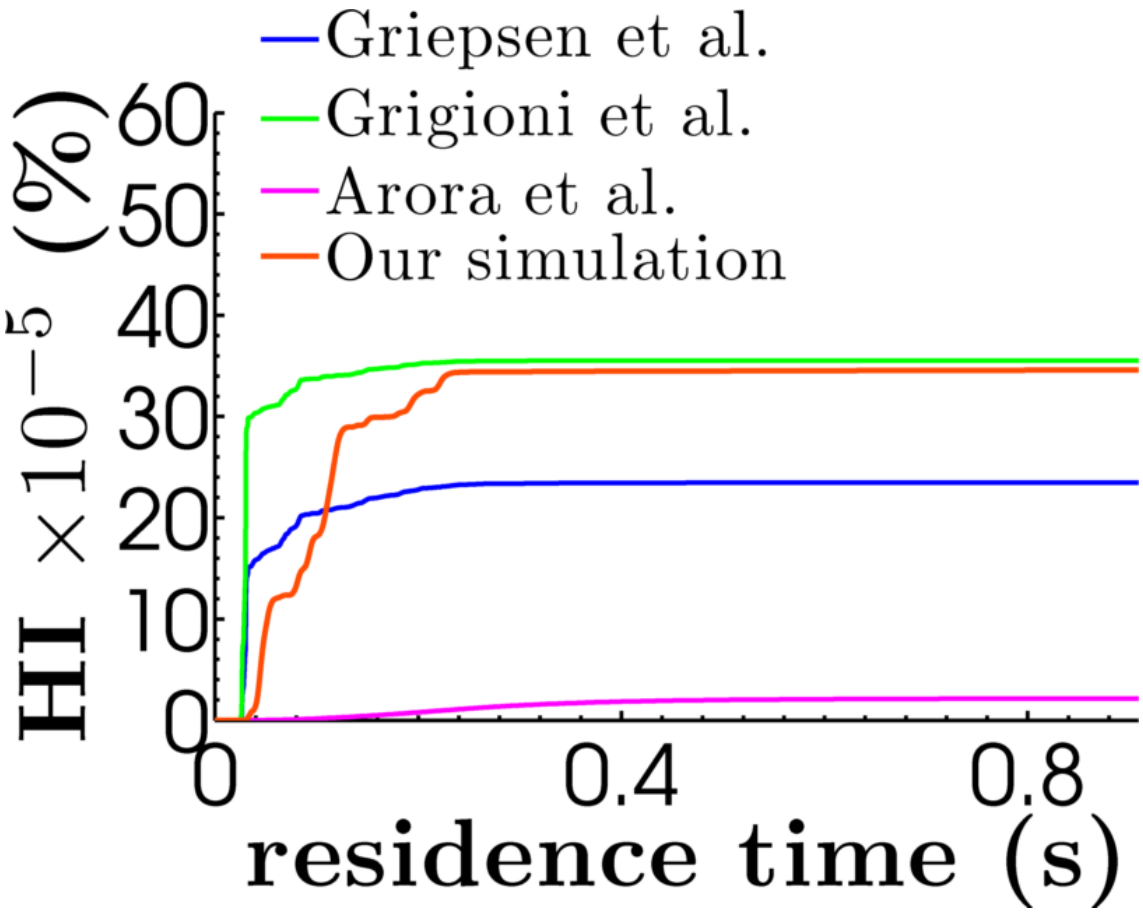

Figure 4.44: Pathline C: The accumulated damage evaluated using four models, Giersiepen et al. [110] equations (4.38), Grigioni et al. [7] equation (4.39), Arora et al. [6] equation (4.40) and the strain-based damage model using the inertia tensor for the RBC coordinates.

cally represent the damage occurring to the RBC structure. However, in the mean time the proposed molecular index is only considered qualitatively, since no available information allows the direct relation to the so called stress or strain based hemolysis models. In addition, there are multiple factors that introduce inaccuracy to the stress-based Giersiepen et al. [110] equation (4.38) & Arora et al. [6]. Therefore, no benchmark data is available to validate the proposed molecular hemolysis model.

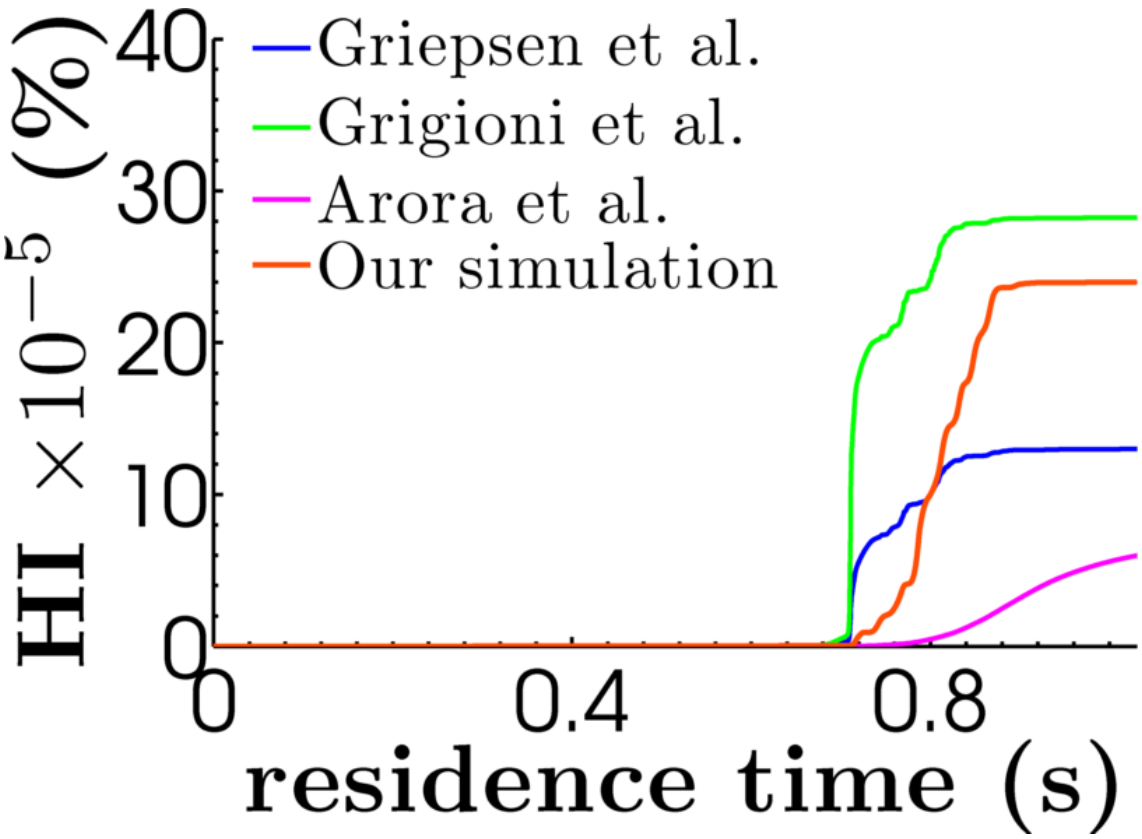

Figure 4.45: Pathline D: The accumulated damage evaluated using four models, Giersiepen et al. [110] equations (4.38), Grigioni et al. [7] equation (4.39), Arora et al. [6] equation (4.40) and the strain-based damage model using the inertia tensor for the RBC coordinates.

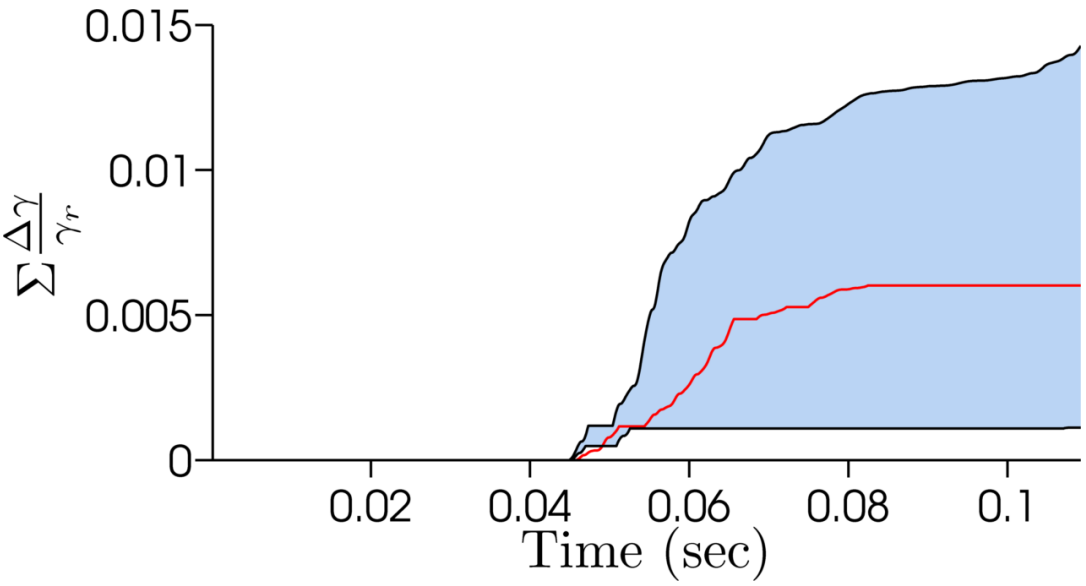

(a)

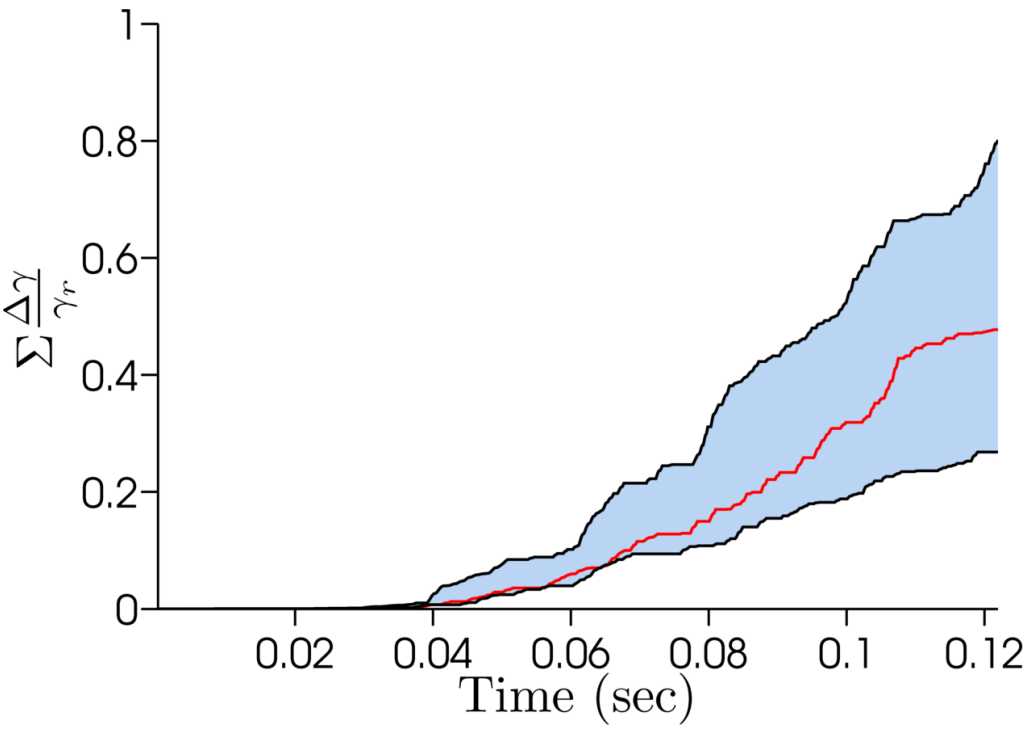

(b)

Figure 4.46: The molecular damage D_M ratio between the change in tension $\Delta\gamma$ and rupture tension γ_r is shown for three locations on the RBC surface. The red solid line represents the location with the average damage over the trajectory of pathline A, while the black lines bounding the blue shade show the maximum and minimum damage accumulated over the pathline trajectory.

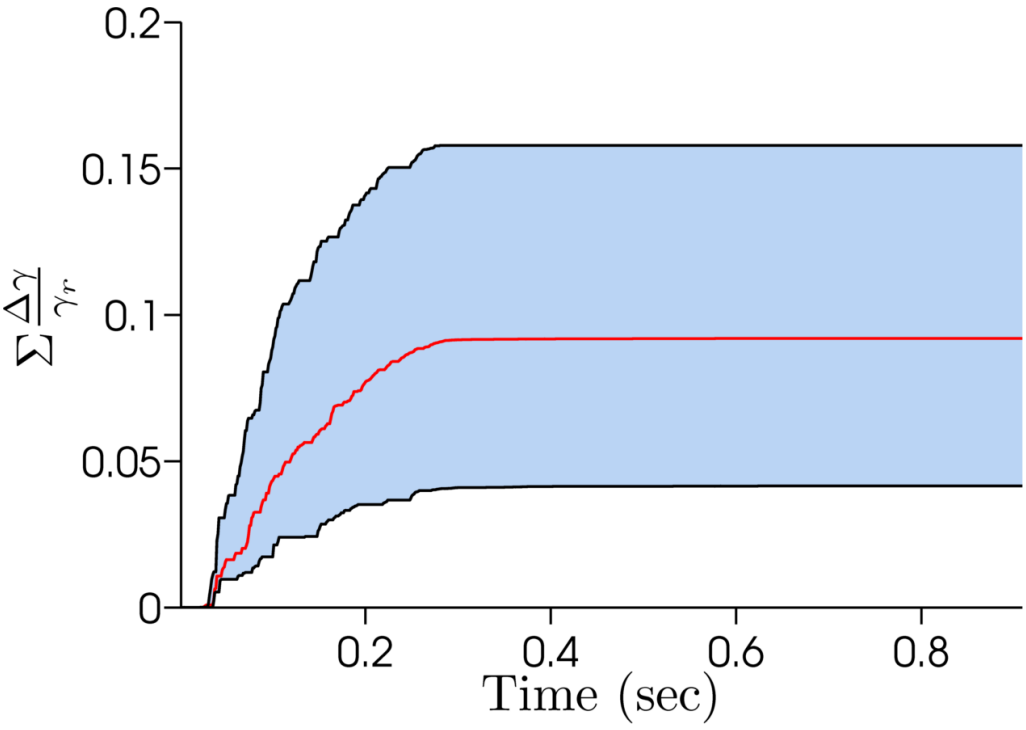

(a)

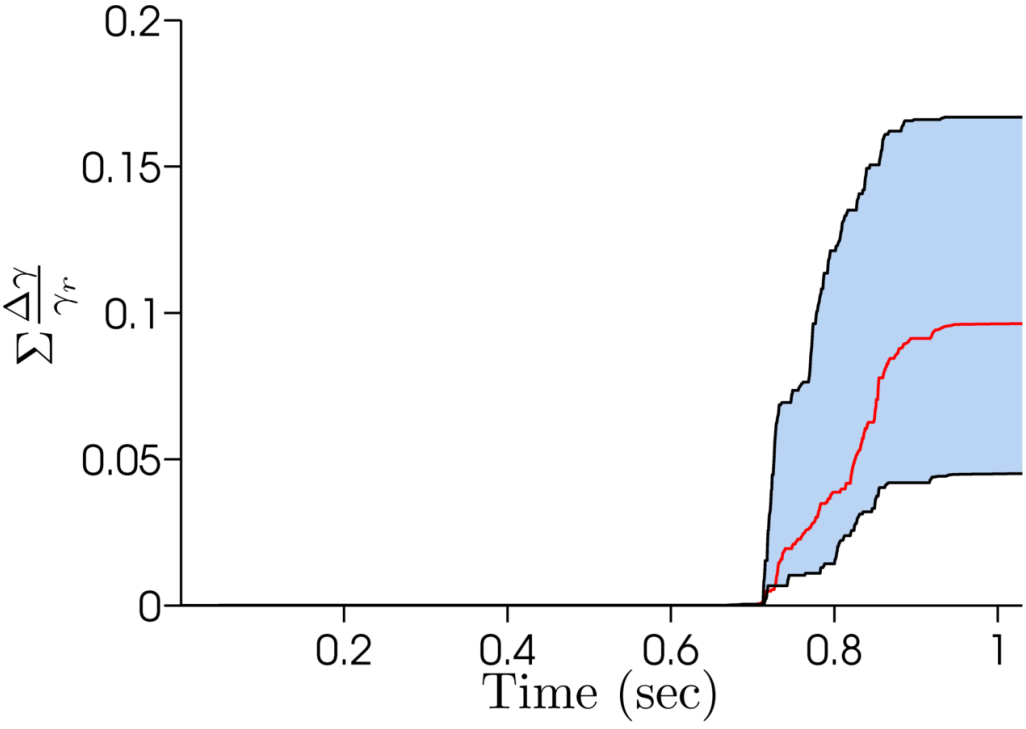

(b)

Figure 4.47: The molecular damage D_M ratio between the change in tension $\Delta\gamma$ and rupture tension γ_r is shown for three locations on the RBC surface. The red solid line represents the location with the average damage over the trajectory of pathline A, while the black lines bounding the blue shade show the maximum and minimum damage accumulated over the pathline trajectory.

4.5 Conclusions

Our goal in this study was to investigate the accuracy of current hemolysis models. The work started by a set of numerical experiments from which we investigated a few points, 1) are the stress-based models the appropriate measure of damage, 2) are the global measures of strain such as the global distortion parameter, ϕ_g really represent the deformation of the RBC or a localized approach is more appropriate, 3) also, we investigated the likely possible scenario of hemolysis pathway when RBC flow through PHVs. Finally, we concluded with the simulation of four pathlines to illustrate the key points mentioned hereinabove.

First, It is important to mention the assumptions upon which our microscopic molecular hemolysis analysis explored in this work was based on; (a) the surface tension is isotropic, therefore the tension calculated at the RBC vertices was a scalar measure (non-directional), such assumption is reasonable since the spatial distribution of the RBC membrane components is uniform with no directional preference; (b) although the difference between RBC membrane and the pure lipid bilayer, e.g. asymmetry in the RBC bilayer structure, presence of integral proteins and Cholesterol distinguish the RBC membrane from that of the lipid bilayers studied in [161] and therefore prevent the exact comparison between the RBC membrane and the pure lipids experiments [161], however, for simplicity, it is assumed that both behave in the same manner, additionally the size of the membrane JC-free areas are big enough to treat as a patches of pure lipid bilayer. This assumption is supported by

the MD simulations by [178] that showed the occurrence a very small patch of lipid bilayer ($\sim 40\ nm^2$) is capable of forming pre-pores that evolve to capable of defects under tension; (c) since hemolysis is accumulative as demonstrated by Yeleswarapu et al. [166], in our analysis loading and unloading were assumed to cause the same damage as long as the membrane is under tension, which is an extremely important difference between the real flow scenario and the experiments. In real flow cases, a certain location on the RBC surface can be subjected to an alternate tension and compression along the course of a pathline, while in experiments only a monotonic loading is used. The experiments don't provide answers for such questions. Whether, damage could be restored immediately upon the removal of external loads, or may be a recovery time is necessary to reset the RBC damage.

The numerical experiments carried out in section 4.4.3 concluded the following: 1) The stress-based hemolysis models are not the correct measure of damage, since they rely on the stresses which do not necessarily correspond to the deformation and hence damage incurred by the RBC, 2) when using the DPD-RBC model we obtained a more accurate prediction of damage because the RBC structure does not conform to an ellipsoid all the time, 3) exploring a local measure of deformation and damage of the RBC seems more reasonable because it expresses the local areal strain and curvature.

After the numerical experiments carried out to reveal the underlying physics of RBCs deformation and hemolysis. We have used the four sample pathlines to test

our findings and understanding. For example, Figures 4.38-4.41 show the stresses calculated relying on the distortion parameter ϕ that represents the global strain of the RBC. Here we are comparing the results of the strain-based hemolysis model using two representation for the RBC, the droplet model proposed by Arora et al. [6] and the solution of the DPD-RBC model from our simulations. The discrepancy in the magnitude and the form of stresses emphasizes the inability of the droplet model used by Arora et al. [6] to accurately predict the behavior of RBC under external loading because not all the conditions and assumptions upon which Arora et al. [6] model was based on were correct. Therefore, the stresses calculated from the our DPD-RBC simulations using equation (4.40) represent a more realistic measure of the RBC deformation.

In addition, two new approaches for studying hemolysis processes from a microscopic perspective were introduced here. The currently established models, either known as "stress-based" or "strain-based", account for the collective behavior of blood by only defining the problem from the fluid point of view. For example, an instantaneous scalar measure of the stresses is used to reduce the transient 3D stress tensor τ, this assumption buries useful information about the real deformation state the RBC undergoes.

The first approach taken here explored the hypothesis that the RBC hemolysis in PHVs is due to the local failure of the lipid bilayer to sustain the tension imposed by the flow. Therefore, building on the reports by Melikov et al. [165] and Seeman

et al. [175] that metastable pores pre-existed (about 0.7 nm in diameter) in RBC membrane, which enlarge to $\sim$ 6 nm when the membrane is stretched by about 6% causing an opening in the bilayer, sufficient for the hemoglobin molecules to exit which results in shortening the lifetime of RBCs in the body. As aforementioned, such mechanism is similar to the osmotic hemolysis [175]. Therefore, the simulation carried out here, examined whether mechanical hemolysis only undergoes a pathway similar to membrane perforation [151] or another mechanisms are involved. Our analysis relied mainly on the surface tension, but also the local bending was inspected to reconcile different modes of deformation that the RBC might undergo. A new qualitative measure, D_M, shown in Figure 4.46a-4.47b for hemolysis was introduced to explore studying the hemolytic process on the microscopic level. The damage was evaluated as ratio between the change in surface tension to the rupture tension.

The second microscopic approach taken to study hemolysis in this dissertation is based on the "strain-based". In this approach instead of predicting the RBC deformation and damage based on the global distortion parameter proposed by Arora et al. [6], we have used a local-based approach, instead of considering the total shape change, we inspected the distortion of each node on the RBC surface. This approach provides more insight about the actual damage, because it accounts for two modes of deformation, the local areal strains and local curvature of the membrane.

Even though the two approach remedy important drawbacks in the current hemolysis model, which use global indicators, it is still very important to verify these two new approaches. But as mentioned before the challenges faced here are obtaining accurate detailed experimental results that will reproduces the real flow characteristics. This experiments should address, if not all at least some of, the ambiguities and unanswered questions raised before. For example, what is the effect of the loading history on the deformation of the RBC, what is the effect of the oscillating loading pattern, how to treat loading as compared to unloading.

Finally, from the magnitudes of local surface tensions that were calculated over the RBC surface, we concluded that no complete breakdown of the RBC structure (fragmentation hemolysis) is taking place during the short term of external loading resembling a single cardiac cycle. Therefore, the case here suggests that pores open across the RBC membrane allowing hemoglobin to exit. According to Chien et al. [170] and Anderson et al. [173] the opened pores in the membrane reseal rapidly, if the applied stresses did not last more than $\sim$ 1 second, around the same order of the single heart beat. Additionally, the level of stresses calculated for PHVs [177] is two orders of magnitude less than that required to rapidly lysis RBCs into fragments (10^3-10^4 as detected in Forstrom jet tests [176] and ultrasonic hemolysis [172]). Therefore, the the membrane perforation mechanism [174] appears to be the most likely pathway of hemolysis for the RBCs flowing the PHVs.

Chapter 5

Intellectual Contributions and Anticipated Benefits

Intellectual Contributions

We list here the contributions of the work done in this dissertation. First we start with the GvpA project that involved molecular mechanics and modeling of the major protein in the gas vesicles walls.

- Development of a molecular mechanics and dynamics simulation scheme to produce a model for the GvpA molecule
- Establishment of a verification scheme to test any model for the GvpA by the reconstructing the AFM image of the gas vesicles walls

Then, we follow by the contributions related to the RBC hemolysis project, which focused primarily on the field of mechanically induced hemolysis. This project uti-

lized the knowledge acquired from the available literature on blood components, mainly RBCs, and combined it with state-of-the-art computational tools to fill the gaps present in current models. Specifically, the expected contributions are as follows:

- Development of a multi-scale simulation methodology to model realistic blood flows that incorporates discretized RBC structures, RBC-RBC interactions and blood-damage.
- Development of software tools for utilizing the above methodology in the simulation and design of actual bio-devices.

Anticipated benefits

The above contributions are expected to result in significant benefits to society at large. Specifically, they will lead to:

- Presenting a model for the GvpA molecule
- Providing a model for the gas vesicle wall by introducing a docked configuration
- Verification of the GvpA model by reconstructing the gas vesicle wall image
- Better physical understanding of mechanical hemolysis and its dependence on hydrodynamic loading

- Reduction in computational time for blood simulations
- Availability of a sophisticated and accurate computational tool for blood flow modeling, which will be useful in the design and assessment of different biodevices
- Overall lower cost, more efficient and safer biodevices

Appendices

Appendix A

Secondary Structure prediction consensus

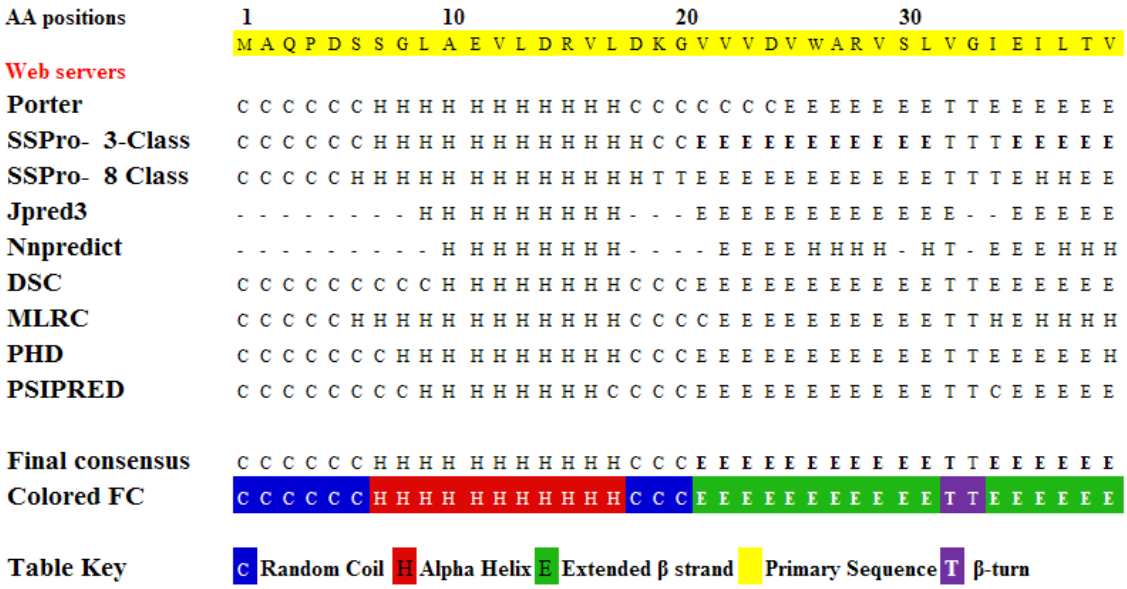

Figure A.1: The secondary structure prediction consensus of GvpA using different web severs, for sequence 1-39; PORTER [55], SSPro [56], Jpred3 [57], NNpredict [58], DSC [59], MLRC [60], PHD [61], and PSIPRED [62].

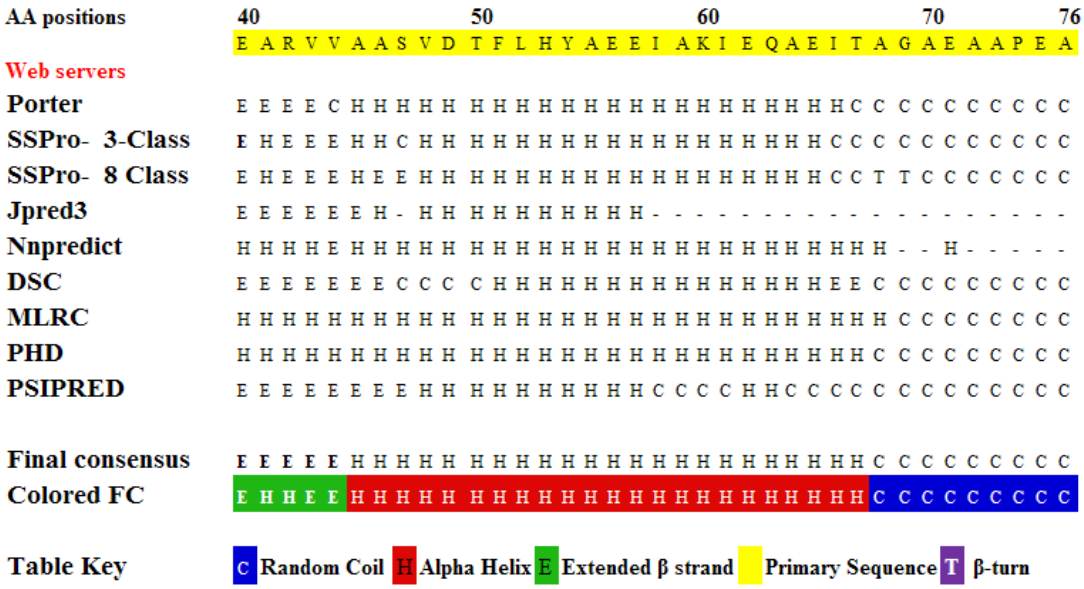

Figure A.2: The secondary structure prediction consensus of GvpA using different web severs, for sequence 40-76; PORTER [55], SSPro [56], Jpred3 [57], NNpredict [58], DSC [59], MLRC [60], PHD [61], and PSIPRED [62].

Appendix B

BLASTP: sequence identity and similarity for GvpA

The following table lists the strain name, lineage, accession no., sequence identity, sequence similarity, and the peptide length for 65 different strains that has been identified to have at least 35% homology with the GvpA sequence from the Halobacterium sp. NRC-1 (accession no. AAC82809) using BlastP. The description of each column follows: second column shows the strain name; third column shows the taxonomical lineage of the strain (i.e. superkingdom, phylum, class, order, family, genus, and species); fourth column shows the accession no. at the http://www.ncbi.nlm.nih.gov website; sixth and seventh provide the sequence identity and similarity, respectively; the last column provides the peptide length of that specific protein.

	Strain name	Lineage	Accession no.	Seq. identity	Seq. Similarity	Length
1	Halorubrum vacuolatum	Archaea; Euryarchaeota; Halobacteria; Halobacteriales; Halobacteriaceae; Halorubrum.	O33397	95	97	78
2	Haloferax mediterranei	Archaea; Euryarchaeota; Halobacteria; Halobacteriales; Halobacteriaceae; Haloferax.	P23761	95	98	78
3	Halobacterium salinarum	Archaea; Euryarchaeota; Halobacteria; Halobacteriales; Halobacteriaceae; Halobacterium.	CAA68593	94	94	85

4	Haloquadratum walsbyi DSM 16790	Archaea; Euryarchaeota; Halobacteria; Halobacteriales; Halobacteriaceae; Haloquadratum.	YP_657547	91	95	72
5	Halogeometricum borinquense DSM 11551	Archaea; Euryarchaeota; Halobacteria; Halobacteriales; Halobacteriaceae; Halogeometricum.	EEJ56295	97	97	78
6	Methanosaeta thermophila PT	Archaea; Euryarchaeota; Methanomicrobia; Methanosarcinales; Methanosaetaceae; Methanosaeta.	ABK13862	81	97	76

7	Natrialba magadii ATCC 43099	Archaea; Euryarchaeota; Halobacteria; Halobacteriales; Halobacteriaceae; Natrialba.	EEG12615	88	96	95
8	Methanosarcina barkeri str. Fusaro	Archaea; Euryarchaeota; Methanomicrobia; Methanosarcinales; Methanosarcinaceae; Methanosarcina.	YP_303890	83	88	76
9	Legionella drancourtii LLAP12	Bacteria; Proteobacteria; Gammaproteobacteria; Legionellales; Legionellaceae; Legionella.	ZP_05111929	74	92	72

10	Burkholderia thailandensis MSMB43	Bacteria; Proteobacteria; Betaproteobacteria; Burkholderiales; Burkholderiaceae; Burkholderia; pseudomallei group	ZP_02467023	71	89	73
11	Burkholderia oklahomensis EO147	Bacteria; Proteobacteria; etaproteobacteria; Burkholderiales; Burkholderiaceae; Burkholderia; pseudomallei group.	ZP_02359285	71	89	73
12	Ancylobacter aquaticus	Bacteria; Proteobacteria; Alphaproteobacteria; Rhizobiales; Xanthobacteraceae; Ancylobacter	AAF16863	67	76	70

13	Bacillus megaterium	Bacteria; Firmicutes; Bacillales; Bacillaceae; Bacillus	AAC38419	63	77	86
14	Nostoc punctiforme PCC 73102	Bacteria; Cyanobacteria; Nostocales; Nostocaceae; Nostoc	ACC80763	59	78	73
15	Microcystis aeruginosa PCC 7806	Bacteria; Cyanobacteria; Chroococcales; Microcystis	CAE11898	62	79	71
16	Geobacter uraniireducens Rf4	Bacteria; Proteobacteria; Deltaproteobacteria; Desulfuromonadales; Geobacteraceae; Geobacter	ABQ27012	73	84	72
17	Microcystis aeruginosa NIES-843	Bacteria; Cyanobacteria; Chroococcales; Microcystis	YP_001658772	62	79	71
18	Arthrospira maxima CS-328	Bacteria; Cyanobacteria; Oscillatoriales; Arthrospira	ZP_03276570	66	81	72

19	Rhodococcus jostii RHA1	Bacteria; Actinobacteria; Actinobacteridae; Actinomycetales; Corynebacterineae; Nocardiaceae; Rhodococcu	YP_703478	60	81	122
20	Psychromonas ingrahamii 37	Bacteria; Proteobacteria; Gammaproteobacteria; Alteromonadales; Psychromonadaceae; Psychromona	ABM03082	70	90	72
21	Anabaena variabilis ATCC 29413	Bacteria; Cyanobacteria; Nostocales; Nostocaceae; Anabaena	ABA19705	60	78	71
22	Desulfotomaculum acetoxidans DSM 771	Bacteria; Firmicutes; Clostridia; Clostridiales; Peptococcaceae; Desulfotomaculum	YP_003192391	73	86	71

23	Microcystis BC 84/1	Bacteria; Cyanobacteria; Chroococcales; Microcystis	P08412	66	83	71
24	Planktothrix rubescens	Bacteria; Cyanobacteria; Oscillatoriales; Planktothrix	CAB59543	63	81	72
25	Thiocapsa pendens	Bacteria; Proteobacteria; Gammaproteobacteria; Chromatiales	P80998	67	83	66
26	Trichodesmium erythraeum IMS101	Bacteria; Cyanobacteria; Oscillatoriales; Trichodesmium	ABG51546	71	88	75
27	Synechococcus sp. JA-3-3Ab	Bacteria; Cyanobacteria; Chroococcales; Synechococcus	ABC99033	64	75	72
28	Pseudanabaena sp. PCC 6901	Bacteria; Cyanobacteria; Oscillatoriales; Pseudanabaena	CAA40898	61	75	72

29	Fremyella diplosiphon-Calothrix	Bacteria; Cyanobacteria; Nostocales; Microchaetaceae; Microchaete	CAA29467	60	78	71
30	Bacillus megaterium GvpB	Bacteria; Firmicutes; Bacillales; Bacillaceae; Bacillu	AAC38416	70	89	88
31	Arthrospira sp. PCC 9901 - s	Bacteria; Cyanobacteria; Oscillatoriales; Arthrospir	ABX79574	71	88	63
32	Anabaena flos-aquae	Bacteria; Cyanobacteria; Nostocales; Nostocaceae; Anabaena	AAA82499	59	78	71
33	Nodularia spumigena	Bacteria; Cyanobacteria; Nostocales; Nostocaceae; Nodularia	AAP46539	59	78	71

34	Chlorobium luteolum DSM 273	Bacteria; Chlorobi; Chlorobia; Chlorobiales; Chlorobiaceae; Chlorobium/Pelodictyon group; Pelodictyon	YP_374609	67	79	68
35	Pelodictyon phaeoclathratiforme BU-1	Bacteria; Chlorobi; Chlorobia; Chlorobiales; Chlorobiaceae; Chlorobium/Pelodictyon group; Pelodictyon	YP_002018666	67	79	68
36	Candidatus Desulforudis audaxviator MP104C	Bacteria; Firmicutes; Clostridia; Clostridiales; Peptococcaceae; Candidatus Desulforudi	YP_001717636	60	81	75
37	Frankia sp. EAN1pec	Bacteria; Actinobacteria; Actinobacteridae; Actinomycetales; Frankineae; Frankiaceae; Frankia	ABW13396	61	84	143

38	Mycobacterium sp. MCS	Bacteria; Actinobacteria; Actinobacteridae; Actinomycetales; Corynebacterineae; Mycobacteriaceae; Mycobacterium	ABG08442	62	87	139
39	Octadecabacter antarcticus 307	Bacteria; Proteobacteria; Alphaproteobacteria; Rhodobacterales; Rhodobacteraceae; Octadecabacte	ZP_05052282	67	80	67
40	Oscillatoria agardhii, green	Bacteria; Cyanobacteria; Oscillatoriales; Planktothrix	AAB23334	66	88	62
41	Pelotomaculum thermopropionicum SI	Bacteria; Firmicutes; Clostridia; Clostridiales; Peptococcaceae; Pelotomaculum	BAF58616	63	87	69

42	Frankia alni ACN14a	Bacteria; Actinobacteria; Actinobacteridae; Actinomycetales; Frankineae; Frankiaceae; Franki	CAJ61669	59	83	143
43	Stackebrandtia nassauensis DSM 44728B B	Bacteria; Actinobacteria; Actinobacteridae; Actinomycetales; Glycomycineae; Glycomycetaceae; Stackebrandti	ZP_04480707	55	83	138
44	Candidatus Koribacter versatilis Ellin345	Bacteria; Acidobacteria; Candidatus Koribacter	YP_591479	64	84	98
45	Streptomyces hygroscopicus ATCC 53653	Bacteria; Actinobacteria; Actinobacteridae; Actinomycetales; Streptomycineae; Streptomycetaceae; Streptomyces	ZP_05512490	52	73	154

46	Polaribacter irgensii 23-P	Bacteria; Bacteroidetes; Flavobacteria; Flavobacteriales; Flavobacteriaceae; Polaribacter.	ZP_01116988	67	84	68
47	Frankia sp. EuI1c	Bacteria; Actinobacteria; Actinobacteridae; Actinomycetales; Frankineae; Frankiaceae; Frankia	ZP_06237942	57	83	166
48	Rhodococcus opacus B4	Bacteria; Actinobacteria; Actinobacteridae; Actinomycetales; Corynebacterineae; Nocardiaceae; Rhodococcus	YP_002777522	61	87	136
49	Bradyrhizobium sp. ORS278	Bacteria; Proteobacteria; Alphaproteobacteria; Rhizobiales; Bradyrhizobiaceae; Bradyrhizobium	AL75183	63	81	70

50	Streptomyces sp. ACT-1	Bacteria; Actinobacteria; Actinobacteridae; Actinomycetales; Streptomycineae; Streptomycetaceae; Streptomyce	EFB80904	47	71	163
51	Streptomyces flavogriseus ATCC 33331	Bacteria; Actinobacteria; Actinobacteridae; Actinomycetales; Streptomycineae; Streptomycetaceae; Streptomyces	ZP_05802772	48	73	150
52	Myxococcus xanthus DK 1622	Bacteria; Proteobacteria; Deltaproteobacteria; Myxococcales; Cystobacterineae; Myxococcaceae; Myxococcus	YP_630987	64	88	74

53	Streptomyces sp. ACTE	Bacteria; Actinobacteria; Actinobacteridae; Actinomycetales; Streptomycineae; Streptomycetaceae; Streptomyces	ZP_06274785	52	79	152
54	Rhodobacter sphaeroides ATCC 17029	Bacteria; Proteobacteria; Alphaproteobacteria; Rhodobacterales; Rhodobacteraceae; Rhodobacter	YP_001045123	58	83	70
55	Trichodesmium erythraeum IMS101	Bacteria; Cyanobacteria; Oscillatoriales; Trichodesmium	YP_722018	60	83	54
56	Octadecabacter antarcticus 238	Bacteria; Proteobacteria; Alphaproteobacteria; Rhodobacterales; Rhodobacteraceae; Octadecabacter	ZP_05068349	41	64	113

57	Streptomyces flavogriseus ATCC 33331	Bacteria; Actinobacteria; Actinobacteridae; Actinomycetales; Streptomycineae; Streptomycetaceae; Streptomyce	ZP_05802767	48	74	114
58	Rhodobacter sphaeroides ATCC 17029	Bacteria; Proteobacteria; Alphaproteobacteria; Rhodobacterales; Rhodobacteraceae; Rhodobacte	YP_001045132	54	80	104
59	Rhodobacter sphaeroides 2.4.1	Bacteria; Proteobacteria; Alphaproteobacteria; Rhodobacterales; Rhodobacteraceae; Rhodobacter	YP_355083	53	76	104

60	Rhodobacter sphaeroides KD131	Bacteria; Proteobacteria; Alphaproteobacteria; Rhodobacterales; Rhodobacteraceae; Rhodobacter	YP_002520683	53	80	104
61	Legionella drancourtii LLAP12	Bacteria; Proteobacteria; Gammaproteobacteria; Legionellales; Legionellaceae; Legionella	ZP_05111936	43	79	106
62	Candidatus Desulforudis audaxviator MP104C	Bacteria; Firmicutes; Clostridia; Clostridiales; Peptococcaceae; Candidatus Desulforudis	YP_001717627	35	52	126
63	Desulfotomaculum acetoxidans DSM 771	Bacteria; Firmicutes; Clostridia; Clostridiales; Peptococcaceae; Desulfotomaculu	YP_003192400	40	68	123

64	Geobacter uraniireducens Rf4	Bacteria; Proteobacteria; Deltaproteobacteria; Desulfuromonadales; Geobacteraceae; Geobacte	YP_001231571	44	61	75
65	Trichodesmium erythraeum IMS101	Bacteria; Cyanobacteria; Oscillatoriales; Trichodesmium	YP_722025	46	74	103

Appendix C

Calculating the Gaussian mean curvature

General approach: Let x_w be a point with coordinates expressed in the global frame of coordinates in which the data is obtained. Let $x = (x, y, z)^T$ be the coordinates of that point in the principal coordinate frame associated with a given point p. Then

$$x = R(x_w - p_w) \tag{C.1}$$

where R is a rotation matrix called the attitude matrix.

To estimate all the parameters of the principal quadric at p at the same time a two step approach is followed: 1) estimating the surface normal and 2) estimating the principal directions. This is achieved by using the rotated principal quadric, which is the principal quadric expressed in a coordinate frame $x' = (x', y', z')^T$ related to

he principal frame by a rotation about the surface normal:

$$\begin{pmatrix} cos\alpha & sin\alpha & 0 \\ -sin\alpha & cos\alpha & 0 \\ 0 & 0 & 1 \end{pmatrix} \tag{C.2}$$

The rotated principal quadric has the form

$$z' = a'x'^2 + b'x'y' + c'y'^2, \tag{C.3}$$

and the associated shape operator matrix is

$$S = \begin{pmatrix} 2a' & b' \\ b' & 2c' \end{pmatrix} \tag{C.4}$$

Where its eigenvalues and eigenvectors are the principal curvatures and directions. A straightforward calculation gives:

$$\begin{aligned} \kappa_1 &= a' + c' + \sqrt{(a'-c')^2 + b'^2} \\ \kappa_2 &= a' + c' - \sqrt{(a'-c')^2 + b'^2} \\ K &= 4a'c' - b'^2 \\ H &= a' + c' \end{aligned} \tag{C.5}$$

The transformation from the world coordinate frame to a rotated principal frame is then

$$x' = R'(x_w - p_w) \tag{C.6}$$

One useful rotated principal frame is defined by choosing $R' = (r_1, r_2, r_3)^T$ as follows:

$$\begin{aligned} r_3 &= n \\ r_1 &= \frac{(I - nn^T)i}{\|(I - nn^T)i\|} \\ r_2 &= r_3 \times r_1, \end{aligned} \tag{C.7}$$

where i is along the first axis in the global coordinate frame and I is the identity matrix. In other words, rotation R' aligns x' with the projection of x_w onto the tangent plane defined by n.

A step-by-step typical method for estimating the principal quadric then goes as follows:(e.g. [179, 180, 181, 182])

1. Estimate the surface normal at p.
2. Construct the rotation matrix R' using equation C.7.
3. Map the world data to the rotated principal frame with equation C.6.
4. Fit the mapped data to the rotated principal quadric using equation C.4, and solve the resulting system, giving a', b', c'.
5. Compute κ_1, κ_2, from a', b', c' using equation C.5.

6. Estimate the attitude matrix by concatenating the transformations, equation C.2, and R'.

The coefficients of the rotated principal quadric (Step 4) are obtained by solving the following over-determined system of linear equations:

$$\begin{bmatrix} x_1^2 & y_1^2 & x_1 y_1 \\ \vdots & \vdots & \vdots \\ x_n^2 & y_n^2 & x_n y_{n1} \end{bmatrix} \begin{bmatrix} a' \\ b' \\ c' \end{bmatrix} = \begin{bmatrix} z_1 \\ \vdots \\ z_n \end{bmatrix} \tag{C.8}$$

This system can be solved using a least-squares method.

Appendix D

The instantaneous shear stress τ

The instantaneous scalar stress τ used in the blood damage models, equations (4.38) and (4.39) is calculated using the deviatoric stress tensor $\boldsymbol{\tau}$ (defined in equation [4.37]), as $\tau = \sqrt{\frac{1}{2}\boldsymbol{\tau} : \boldsymbol{\tau}}$, where the (:) implies the double inner product of the 2^{nd} rank tensor $\boldsymbol{\tau}$ as follows,

$$\mathbf{A{:}B} = \mathbf{C}, \text{ where } A_{ij}B_{ji} = C.$$

In details: $\mathbf{A} : \mathbf{B} = A_{ij}B_{kl}\delta_{jk}\delta_{il} = A_{ij}B_{jl}\delta_{il} = A_{ij}B_{ji}$ (the Kronecker delta is used to enforce the required equality of nearest, as well as next-nearest, indices), (therefore, $C = A_{11}B_{11}+A_{12}B_{21}+A_{13}B_{31}+A_{21}B_{12}+A_{22}B_{22}+A_{23}B_{32}+A_{31}B_{13}+A_{32}B_{23}+A_{33}B_{33}$)

$$\tau = \sqrt{\frac{1}{2}\left[\boldsymbol{\tau}_{11}^2 + \boldsymbol{\tau}_{22}^2 + \boldsymbol{\tau}_{33}^2 + 2\boldsymbol{\tau}_{12}^2 + 2\boldsymbol{\tau}_{23}^2 + 2\boldsymbol{\tau}_{13}^2\right]} \tag{D.1}$$

Bibliography

[1] Emiliano Carretti, Luigi Dei, and Richard G. Weiss. Soft matter and art conservation. rheoreversible gels and beyond. *Soft Matter*, 1:17–22, 2005.

[2] Supratim Banerjee, Rajat K. Das, and Uday Maitra. Supramolecular gels "in action". *Journal Material Chemistry*, 19:6649–6687, 2009.

[3] G. Gompper and M. Schick. *Soft Matter Volume 1: Polymer Melts and Mixtures*, volume 1. Wiley-VCH, 2006.

[4] B. N. Nanjappa, Hsin-Kang Chang, and Chester A. Glomski. Trauma of the erythrocyte membrane associated with low shear stress. *Biophysical Journal*, 13(11):1212–1222, 1973.

[5] H. Schima, M. R. Müller, S. Tsangaris, G. Gheiseder, C. Schlusche, U. Losert, H. Thoma, and E. Wolner. Mechanical blood traumatization by tubing and throttles in in vitro pump tests: Experimental results and implications for hemolysis theory. *International Journal of Artificial Organs*, 17(3):164–170, 1993.

[6] D. Arora, M. Behr, and M. Pasquali. A tensor-based measure for estimating blood damage. *Artificial organs*, 28(11):1002–1015, 2004.

[7] Mauro Grigioni, Umberto Morbiducci, Giuseppe D'Avenio, Giacomo Di Benedetto, and Costantino Del Gaudio. A novel formulation for blood trauma prediction by a modified power-law mathematical model. *Biomechanics and Modeling in Mechanobiology*, 4(4):249–260, 2005.

[8] Mauro Grigioni, Carla Daniele, Umberto Morbiducci, Giuseppe D'Avenio, Giacomo Di Benedetto, and Vincenzo Barbaro. The power-law mathematical model for blood damage prediction: Analytical developments and physical inconsistencies. *Internation Journal Artifical Organs*, 28(5):467–475, 2004.

[9] A. E. Blaurock and A. E. Walsby. Crystalline structure of the gas vesicle wall from anabaena flos-aquae. *Journal of Molecular Biology*, 105(2):183, 1976.

[10] S. DasSarma and P. Arora. Genetic analysis of the gas vesicle gene cluster in haloarchaea. *Fems Microbiology Letters*, 153(1):1–10, 1997.

[11] M.J. Krantz and C.E. Ballou. Analysis of halobacterium halobium gas vesicles. *Journal of bacteriology*, 114(3):1058, 1973.

[12] TJ McMaster, MJ Miles, and AE Walsby. Direct observation of protein secondary structure in gas vesicles by atomic force microscopy. *Biophysical Journal*, 70(5):2432–2436, 1996.

[13] AE Walsby. Gas vesicles. *Annual review of plant physiology*, 26(1):427–439, 1975.

[14] SD Bentley, KF Chater, A.M. Cerdeno-Tarraga, GL Challis, NR Thomson, KD James, DE Harris, MA Quail, H. Kieser, D. Harper, et al. Complete genome sequence of the model actinomycete streptomyces coelicolor a3 (2). *Nature*, 417(6885):141–147, 2002.

[15] N. Li and M.C. Cannon. Gas vesicle genes identified in bacillus megaterium and functional expression in escherichia coli. *Journal of bacteriology*, 180(9):2450–2458, 1998.

[16] TN Zhilina and GA Zavarzin. Comparative cytology of methanosarcina and a description of methanosarcina vacuolata n. sp. *Mikrobiologiia*, 48(2):279, 1979.

[17] AE Walsby. Structure and function of gas vacuoles. *Bacteriological reviews*, 36(1):1, 1972.

[18] A.C. Sivertsen, M.J. Bayro, M. Belenky, R.G. Griffin, and J. Herzfeld. Solid-state nmr characterization of gas vesicle structure. *Biophysical journal*, 99(6):1932–1939, 2010.

[19] G. E. Fogg. *The Blue-green algae*. Academic Press, London ; New York, 1973.

[20] A. Sundararajan and L.K. Ju. Evaluation of oxygen permeability of gas vesicles from cyanobacterium anabaena flos-aquae. *Journal of biotechnology*, 77(2-3):151–156, 2000.

[21] A. E. Walsby. Pressure relationships of gas vacuoles. *Proceedings of the Royal Society of London Series B-Biological Sciences*, 178(1052):301, 1971.

[22] AE Walsby. Gas vesicles. *Microbiological reviews*, 58(1):94, 1994.

[23] S. DasSarma, P. Arora, F. Lin, E. Molinari, and LR Yin. Wild-type gas vesicle formation requires at least ten genes in the gvp gene cluster of halobacterium halobium plasmid pnrc100. *Journal of bacteriology*, 176(24):7646–7652, 1994.

[24] J. G. Jones, N. R. Hackett, J. T. Halladay, D. J. Scothorn, C. F. Yang, W. L. Ng, and S. Dassarma. Analysis of insertion mutants reveals 2 new genes in the pnrc100 gas vesicle gene-cluster of halobacterium-halobium. *Nucleic Acids Research*, 17(19):7785–7793, 1989.

[25] J.T. Halladay, JG Jones, F. Lin, A.B. MacDonald, and S. DasSarma. The rightward gas vesicle operon in halobacterium plasmid pnrc100: identification of the gvpa and gvpc gene products by use of antibody probes and genetic analysis of the region downstream of gvpc. *Journal of bacteriology*, 175(3):684–692, 1993.

[26] A. E. Walsby and P. K. Hayes. The minor cyanobacterial gas vesicle protein, gvpc, is attached to the outer surface of the gas vesicle. *Journal of General Microbiology*, 134(10):2647–2657, 1988.

[27] P K Hayes, B Buchholz, and E Walsby, A. Gas vesicles are strengthened by the outer-surface protein, gvpc. *Archives of Microbiology*, 157(3):229–234, 1992.

[28] C. Thongthai and P. Suntinanalert. *Halophiles in Thai Fish Sauce (Nam Pla)*. General and Applied Aspects of Halophilic Microorganisms. Plenum Press, New York. pp.381-388, 1991.

[29] Rosa Margesin and Franz Schinner. Potential of halotolerant and halophilic microorganisms for biotechnology. *Extremophiles*, 5(2):73–83, 2001.

[30] Shiladitya DasSarma, Fazeela Morshed, Stuart Elizabeth, and Samuel Black. Recombinant gas vesicles and uses thereof, 1998.

[31] E. S. Stuart, F. Morshed, M. Sremac, and S. DasSarma. Antigen presentation using novel particulate organelles from halophilic archaea. *Journal of Biotechnology*, 88(2):119–128, 2001.

[32] J.B. Delehanty, H. Mattoussi, and I.L. Medintz. Delivering quantum dots into cells: strategies, progress and remaining issues. *Analytical and bioanalytical chemistry*, 393(4):1091–1105, 2009.

[33] Y. Malam, M. Loizidou, and A.M. Seifalian. Liposomes and nanoparticles: nanosized vehicles for drug delivery in cancer. *Trends in pharmacological sciences*, 30(11):592–599, 2009.

[34] N.G. Portney and M. Ozkan. Nano-oncology: drug delivery, imaging, and sensing. *Analytical and bioanalytical chemistry*, 384(3):620–630, 2006.

[35] K.S. Soppimath, T.M. Aminabhavi, A.R. Kulkarni, and W.E. Rudzinski. Biodegradable polymeric nanoparticles as drug delivery devices. *Journal of controlled release*, 70(1):1–20, 2001.

[36] Peter Hoet, Irene Bruske-Hohlfeld, and Oleg Salata. Nanoparticles - known and unknown health risks. *Journal of Nanobiotechnology*, 2(12), 2004.

[37] S Lanone, F Rogerieux, J Geys, A Dupont, E Maillot-Marechal, J Boczkowski, G Lacroix, and P Hoet. Comparative toxicity of 24 manufactured nanoparticles in human alveolar epithelial and macrophage cell lines. *Particle and Fibre Toxicology*, 6, 2009.

[38] R. S. Powell, A. E. Walsby, P. K. Hayes, and R. Porter. Antibodies to the n-terminal sequence of gvpa bind to the ends of gas vesicles. *Journal of General Microbiology*, 137(10):2395–2400, 1991.

[39] Shiladitya DasSarma, Brian Berquist, James Coker, Priya DasSarma, and Jochen Muller. Post-genomics of the model haloarchaeon halobacterium sp. nrc-1. *Saline Systems*, 2(3), 2006.

[40] D. D. Jones and M. Jost. Isolation and chemical characteristics of gas-vacuole membranes from microcystis-aeruginosa kuetz. emend. elenkin. *Archiv Fur Mikrobiologie*, 70(1):43–&, 1970.

[41] D. D. Jones and M. Jost. Characterization of the protein from gas-vacuole membranes of the blue-green alga, microcystis aeruginosa. *Planta*, 100(4):277–287, 1971.

[42] Y. Zhang. Progress and challenges in protein structure prediction. *Current Opinion in Structural Biology*, 18(3):342–348, 2008.

[43] Richard Bonneau, Charlie E. M. Strauss, Carol A. Rohl, Dylan Chivian, Phillip Bradley, Lars Malmstrom, Tim Robertson, and David Baker. De novo prediction of three-dimensional structures for major protein families. *Journal of Molecular Biology*, 322(1):65, 2002.

[44] J. Moult. A decade of casp: progress, bottlenecks and prognosis in protein structure prediction. *Current Opinion in Structural Biology*, 15(3):285–289, 2005.

[45] James J. Vincent, Chin-Hsien Tai, B.K. Sathyanarayana, and Byungkook Lee. Assessment of casp6 predictions for new and nearly new fold targets. *Proteins: Structure, Function, and Bioinformatics*, 61(S7):67–83, 2005.

[46] Y. Zhang. Template-based modeling and free modeling by i-tasser in casp7. *Proteins: Structure, Function, and Bioinformatics*, 69(S8):108–117, 2007.

[47] Moshe Ben-David, Orly Noivirt-Brik, Aviv Paz, Jaime Prilusky, Joel L. Sussman, and Yaakov Levy. Assessment of casp8 structure predictions for template free targets. *Proteins: Structure, Function, and Bioinformatics*, 77(S9):50–65, 2009.

[48] Richard Bonneau, Jerry Tsai, Ingo Ruczinski, Dylan Chivian, Carol Rohl, Charlie E. M. Strauss, and David Baker. Rosetta in casp4: Progress in ab initio protein structure prediction. *Proteins: Structure, Function, and Genetics*, 45(S5):119, 2001.

[49] Sitao Wu, Jeffrey Skolnick, and Yang Zhang. Ab initio modeling of small proteins by iterative tasser simulations. *BMC Biology*, 5(17), 2007.

[50] Jayashree Srinivasan, Thomas E. Cheatham, Piotr Cieplak, Peter A. Kollman, and David A. Case. Continuum solvent studies of the stability of dna, rna, and phosphoramidatedna helices. *Journal of the American Chemical Society*, 120(37):9401–9409, 1998.

[51] T. Strunk, K. Hamacher, F. Hoffgaard, H. Engelhardt, M.D. Zillig, K. Faist, W. Wenzel, and F. Pfeifer. Structural model of the gas vesicle protein gvpa and analysis of gvpa mutants in vivo. *Molecular Microbiology*, 2011.

[52] J. E. Walker, A. E. Walsby, and P. K. Hayes. Homology of gas vesicles proteins in cyanobacteria and halobacteria. *Journal of General Microbiology*, 130:2709, 1984.

[53] S.L. DasSarma, M.D. Capes, P. DasSarma, and S. DasSarma. Haloweb: the haloarchaeal genomes database. *Saline Systems*, 6(1):12, 2010.

[54] Wailap Victor Ng, Sean P. Kennedy, Gregory G. Mahairas, Brian Berquist, Min Pan, Hem Dutt Shukla, Stephen R. Lasky, Nitin S. Baliga, Vesteinn Thorsson, Jennifer Sbrogna, Steven Swartzell, Douglas Weir, John Hall, Timothy A. Dahl, Russell Welti, Young Ah Goo, Brent Leithauser, Kim Keller, Randy Cruz, Michael J. Danson, David W. Hough, Deborah G. Maddocks, Peter E. Jablonski, Mark P. Krebs, Christine M. Angevine, Heather Dale, Thomas A. Isenbarger, Ronald F. Peck, Mechthild Pohlschroder, John L. Spudich, Kwang-Hwan Jung, Maqsudul Alam, Tracey Freitas, Shaobin Hou, Charles J. Daniels, Patrick P. Dennis, Arina D. Omer, Holger Ebhardt, Todd M. Lowe, Ping Liang, Monica Riley, Leroy Hood, and Shiladitya DasSarma. Genome sequence of halobacterium species nrc-1. *Proceedings of the National Academy of Sciences of the United States of America*, 97(22):12176–12181, 2000.

[55] Gianluca Pollastri and Aoife McLysaght. Porter: a new, accurate server for protein secondary structure prediction. *Bioinformatics*, 21(8):1719, 2005.

[56] J. Cheng, AZ Randall, MJ Sweredoski, and P. Baldi. Scratch: a protein structure and structural feature prediction server. *Nucleic acids research*, 33(suppl 2):W72–W76, 2005.

[57] Christian Cole, Jonathan D. Barber, and Geoffrey J. Barton. The jpred 3 secondary structure prediction server. *Nuclic Acids Research*, 36($suppl_2$):W197, 2008.

[58] DG Kneller, FE Cohen, R. Langridge, et al. Improvements in protein secondary structure prediction by an enhanced neural network. *Journal of molecular biology*, 214(1):171, 1990.

[59] Ross D. King and Michael J. E. Sternberg. Identification and application of the concepts important for accurate and reliable protein secondary structure prediction. *Protein Science*, 5(11):2298, 1996.

[60] Y. Guermeur, C. Geourjon, P. Gallinari, and G. Deleage. Improved performance in protein secondary structure prediction by inhomogeneous score combination. *Bioinformatics*, 15(5):413, 1999.

[61] Burkhard Rost and Chris Sander. Prediction of protein secondary structure at better than 70accuracy. *Journal of Molecular Biology*, 232(2):584, 1993.

[62] K. Bryson, L.J. McGuffin, R.L. Marsden, J.J. Ward, J.S. Sodhi, and D.T. Jones. Protein structure prediction servers at university college london. *Nucleic acids research*, 33(suppl 2):W36–W38, 2005.

[63] Barbara Stuart and D. J. Ando. *Modern infrared spectroscopy*. Analytical Chemistry by Open Learning. Published on behalf of ACOL (University of Greenwich) by Wiley, Chichester ; New York, 1996.

[64] David Whitford. *Proteins : structure and function*. John Wiley & Sons, Chichester, West Sussex, England ; Hoboken, NJ, 2005.

[65] N. Eswar, B. Webb, M.A. Marti-Renom, MS Madhusudhan, D. Eramian, M.Y. Shen, U. Pieper, and A. Sali. Comparative protein structure modeling using modeller. *Current Protocol in Protein Science*, 2(12):15–32, 2007.

[66] Andrej Sali, Liz Potterton, Feng Yuan, Herman van Vlijmen, and Martin Karplus. Evaluation of comparative protein modeling by modeller. *Proteins: Structure, Function, and Bioinformatics*, 23(3):318–326, 1995.

[67] Ursula Pieper, Narayanan Eswar, Ben M. Webb, David Eramian, Libusha Kelly, David T. Barkan, Hannah Carter, Parminder Mankoo, Rachel Karchin, Marc A. Marti-Renom, Fred P. Davis, and Andrej Sali. Modbase, a database of annotated comparative protein structure models and associated resources. *Nuclic Acids Research*, 37($suppl_1$):D347–354, 2009.

[68] Christiam Camacho, George Coulouris, Vahram Avagyan, Ning Ma, Jason Papadopoulos, Kevin Bealer, and Thomas Madden. Blast+: architecture and applications. *BMC Bioinformatics*, 10(1):421, 2009.

[69] Y. Zhang. I-tasser server for protein 3d structure prediction. *BMC Bioinformatics*, 9(1):40, 2008.

[70] Sitao Wu and Yang Zhang. Lomets: A local meta-threading-server for protein structure prediction. *Nuclic Acids Research*, 35(10):3375–3382, 2007.

[71] Daniel John Rigden. *From protein structure to function with bioinformatics*. Springer, 2009.

[72] MR Lee, J Tsai, D Baker, and PA Kollman. Molecular dynamics in the endgame of protein structure prediction. *Journal of Molecular Biology*, 313(2):417–430, 2001.

[73] M. Buck, S. Bouguet-Bonnet, R.W. Pastor, and A.D. MacKerell Jr. Importance of the cmap correction to the charmm22 protein force field: dynamics of hen lysozyme. *Biophysical journal*, 90(4):L36–L38, 2006.

[74] Tom Darden, Darrin York, and Lee Pedersen. Particle mesh ewald: An n center-dot log(n) method for ewald sums in large systems. *Journal Chemical Physics*, 98(12):10089, 1993.

[75] H. Grubmüller, H. Heller, A. Windemuth, and K. Schulten. Generalized verlet algorithm for efficient molecular dynamics simulations with long-range interactions. *Molecular Simulation*, 6(1-3):121–142, 1991.

[76] M. Tuckerman, B.J. Berne, and G.J. Martyna. Reversible multiple time scale molecular dynamics. *The Journal of chemical physics*, 97:1990, 1992.

[77] J.P. Ryckaert, G. Ciccotti, and H.J.C. Berendsen. Numerical integration of the cartesian equations of motion of a system with constraints: molecular dynamics of alkanes. *Journal of Computational Physics*, 23(3):327–341, 1977.

[78] Scott E. Feller, Yuhong Zhang, Richard W. Pastor, and Bernard R. Brooks. Constant pressure molecular dynamics simulation: The langevin piston method. *The Journal Chemical Physics*, 103(11):4613–4621, 1995.

[79] James C. Phillips, Rosemary Braun, Wei Wang, James Gumbart, Emad Tajkhorshid, Elizabeth Villa, Christophe Chipot, Robert D. Skeel, Laxmikant Kale, Klaus Schulten, G. Pollastri, and P. Baldi. Scalable molecular dynamics with namd prediction of contact maps by giohmms and recurrent neural networks using lateral propagation from all four cardinal corners. *Chemical Physics Letters*, 26(16):1781–1802, 2005.

[80] Matthew R. Lee, Yong Duan, and Peter A. Kollman. Use of MM-PB/SA in estimating the free energies of proteins: Application to native, intermediates, and unfolded villin headpiece. *Proteins: Structure, Function, and Genetics*, 39(4):309–316, 2000.

[81] W Rocchia, S Sridharan, A Nicholls, E Alexov, A Chiabrera, and B Honig. Rapid grid-based construction of the molecular surface and the use of induced surface charge to calculate reaction field energies: Applications to the molecular systems and geometric objects. *Journal of Computational Chemistry*, 23(1):128–137, 2002.

[82] W Rocchia, E Alexov, and B Honig. Extending the applicability of the nonlinear poisson-boltzmann equation: Multiple dielectric constants and multivalent ions. *Journal of Physical Chemistry B*, 105(28):6507–6514, 2001.

[83] W. Clark Still, Anna Tempczyk, Ronald C. Hawley, and Thomas Hendrickson. Semianalytical treatment of solvation for molecular mechanics and dynamics. *Journal of the American Chemical Society*, 112(16):6127–6129, 1990.

[84] D. Sitkoff, K.A. Sharp, and B. Honig. Accurate calculation of hydration free energies using macroscopic solvent models. *The Journal of Physical Chemistry*, 98(7):1978–1988, 1994.

[85] B Lee and F M Richards. The interpretation of protein structures: estimation of static accessibility. *Journal of Molecular Biology*, 55(3):379–400, 1971.

[86] W Humphrey, A Dalke, and K Schulten. VMD: Visual Molecular Dynamics. *Journal of Molecular Graphics*, 14(1):33–38, 1996.

[87] AC Sivertsen, MJ Bayro, M Belenky, RG Griffin, and J Herzfeld. Solid-state nmr evidence for inequivalent gvpa subunits in gas vesicles. *Journal of Molecular Biology*, pages 1032–1039, 2009.

[88] S.D. Solares. Single biomolecule imaging with frequency and force modulation in tapping-mode atomic force microscopy. *The Journal of Physical Chemistry B*, 111(9):2125–2129, 2007.

[89] S.D. Solares and J.C. Crone. Real-time simulation of isolated biomolecule characterization with frequency and force modulation atomic force microscopy. *The Journal of Physical Chemistry C*, 111(27):10029–10034, 2007.

[90] F.J. Giessibl. Advances in atomic force microscopy. *Reviews of modern physics*, 75(3):949, 2003.

[91] B. J. Carrington and R. L. Mancera. Comparative estimation of vibrational entropy changes in proteins through normal modes analysis. *Journal of Molecular Graphics and Modelling*, 23(2):167–174, 2004.

[92] Bruce Tidor and Martin Karplus. The contribution of cross-links to protein stability: A normal mode analysis of the configurational entropy of the native state. *Proteins: Structure, Function, and Genetics*, 15(1):71–79, 1993.

[93] M. J. Danson and D. W. Hough. The structural basis of protein halophilicity. *Comparative biochemistry and physiology: A-Physiology*, 117A(3):307–312, 1997.

[94] T. A. Halgren and W. Damm. Polarizable force fields. *Current Opinion in Structural Biology*, 11(2):236–242, 2001.

[95] A. Bleasy. Emboss needle: Pairwise alignment algorithms, 2000.

[96] Saul B. Needleman and Christian D. Wunsch. A general method applicable to the search for similarities in the amino acid sequence of two proteins. *Journal of Molecular Biology*, 48(3):443–453, 1970.

[97] AE Griffiths, AE Walsby, and PK HAYES. The homologies of gas vesicles proteins. *Journal of General Microbiology*, 138:1243–1250, 1992.

[98] Marina Belenky, Rebecca Meyers, and Judith Herzfeld. Subunit structure of gas vesicles: A maldi-tof mass spectrometry study. *Proceedings of the National Academy of Sciences*, 86(1):499–505, 2004.

[99] Sonja Offner, Ulrike Ziese, Gerhard Wanner, Dieter Typke, and Felicitas Pfeifer. Structural characteristics of halobacterial gas vesicles. *Microbiology*, 144(5):1331–1342, 1998.

[100] Donald Lloyd-Jones, Robert Adams, Mercedes Carnethon, Giovanni De Simone, T. Bruce Ferguson, Katherine Flegal, Earl Ford, Karen Furie, Alan Go, Kurt Greenlund, Nancy Haase, Susan Hailpern, Michael Ho, Virginia Howard, Brett Kissela, Steven Kittner, Daniel Lackland, Lynda Lisabeth, Ariane Marelli, Mary McDermott, James Meigs, Dariush Mozaffarian, Graham Nichol, Christopher O'Donnell, Veronique Roger, Wayne Rosamond, Ralph Sacco, Paul Sorlie, Randall Stafford, Julia Steinberger, Thomas Thom, Sylvia Wasserthiel-Smoller, Nathan Wong, Judith Wylie-Rosett, Yuling Hong, for the American Heart Association Statistics Committee, and Stroke Statistics Subcommittee. Heart disease and stroke statistics-2009 update: A report from the american heart association statistics committee and stroke statistics subcommittee. *Circulation*, 119(3):e21–181, 2009.

[101] Gerald Lim H W, Michael Wortis, and Ranjan Mukhopadhyay. Stomatocyte-discocyte-echinocyte sequence of the human red blood cell: evidence for the bilayer- couple hypothesis from membrane mechanics. *Proceedings of the National Academy of Sciences, U S A*, 99(26):16766–9, 2002.

[102] DE Discher, DH Boal, and SK Boey. Simulations of the erythrocyte cytoskeleton at large deformation. II. micropipette aspiration. *Biophysical Journal*, 75(3):1584–1597, 1998.

[103] M Dao, CT Lim, and S Suresh. Mechanics of the human red blood cell deformed by optical tweezers. *Journal of the Mechanics and Physics of Solids*, 51(11-12):2259–2280, 2003.

[104] Yaron Shapira, Mordehay Vaturi, and Alex Sagie. Hemolysis associated with prosthetic heart valves: A review. *Cardiology in Review*, 17(3), 2009.

[105] Andrey Nikolaevich Kolmogorov. The local structure of turbulence in incompressible viscous fluid for very large reynolds numbers. *Proceedings of the Royal Society of London, Series A: Mathematical and Physical Sciences*, 434(1890):9–13, 1991.

[106] Andrey Nikolaevich Kolmogorov. Dissipation of energy in the locally isotropic turbulence. *Proceedings: Mathematical and Physical Sciences*, 434(1890):15–17, 1991.

[107] T J Vander Salm, L A Pape, and J F Mauser. Mitral valve replacement with complete retention of native leaflets. *Annual Thorac Surgery*, 59(1):52–55, 1995.

[108] American Society for Testing and Materials. "Standard practice for assessment of hemolysis in continuous flow blood pumps". Standard F 1841 - 97, ASTM, 1997.

[109] D. Arora. *Computational hemodynamics: Hemolysis and viscoelasticity*. Phd thesis, Rice University., Texas, United States, 2006.

[110] M Giersiepen, L J Wurzinger, R Opitz, and H Reul. Estimation of shear stress-related blood damage in heart valve prostheses in -vitro comparison of 25 aortic valves. *Internation Journal Artifical Organs*, 13(5):300–306, 1990.

[111] G Bao and S Suresh. Cell and molecular mechanics of biological materials. *Nature Materials*, 2(11):715–25, 2003.

[112] E.A. Evans and R. Skalak. *Mechanics and thermodynamics of biomembranes*. CRC Press, Inc., Boca Raton, Florida., 1980.

[113] P. Bagchi. Mesoscale simulation of blood flow in small vessels. *Biophysical Journal*, 92(6):1858–1877, 2007.

[114] S K Boey, D H Boal, and D E Discher. Simulations of the erythrocyte cytoskeleton at large deformation. I. Microscopic models. *Biophysical Journal*, 75(3):1573–83, 1998.

[115] D.A. Fedosov, B. Caswell, and G.E. Karniadakis. A multiscale red blood cell model with accurate mechanics, rheology, and dynamics. *Biophysical journal*, 98(10):2215, 2010.

[116] Dmitry A. Fedosov, Bruce Caswell, and George Em Karniadakis. Systematic coarse-graining of spectrin-level red blood cell models. *Computer Methods in Applied Mechanics and Engineering*, 199(29-32):1937–1948, 2010.

[117] Hiroshi Noguchi and Gerhard Gompper. Shape transitions of fluid vesicles and red blood cells in capillary flows. *PNAS Proceedings of the National Academy of Science USA*, 102(40):14159–14164, 2005.

[118] Witold Dzwinel, Krzysztof Boryczko, and David A. Yuen. A discrete-particle model of blood dynamics in capillary vessels. *Journal of Colloid and Interface Science*, 258(1):163–173, 2003.

[119] G. M. Artmann, K. L. Sung, T. Horn, D. Whittemore, G. Norwich, and S. Chien. Micropipette aspiration of human erythrocytes induces echinocytes via membrane phospholipid translocation. *Biophysical Journal*, 72(3):1434–1441, 1997.

[120] E.A. Evans. Bending elastic modulus of red blood cell membrane derived from buckling instability in micropipet aspiration tests. *Biophysical Journal*, 43(1):27–30, 1983.

[121] K. Gunnar Engstrom and Herbert J. Meiselman. Effects of pressure on red blood cell geometry during micropipette aspiration. *Cytometry*, 23(1):22–27, 1996.

[122] D. E. Discher, N. Mohandas, and E. A. Evans. Molecular maps of red cell deformation: hidden elasticity and in situ connectivity. *Science*, 266(5187):1032–1035, 1994.

[123] C. T. Lim, M. Dao, S. Suresh, C. H. Sow, and K. T. Chew. Large deformation of living cells using laser traps. *Acta Materialia*, 52(7):1837–1845, 2004.

[124] R. Waugh and E.A. Evans. Thermoelasticity of red blood cell membrane. *Biophysical Journal*, 26(1):115–131, 1979.

[125] S. Shin, M. S. Park, Y. H. Ku, and J. S. Suh. Shear-dependent aggregation characteristics of red blood cells in a pressure-driven microfluidic channel. *Clinical Hemorheology and Microcirculation*, 34(1):353–361, 2006.

[126] Rui Zhao, James F Antaki, Tikeswar Naik, Timothy N Bachman, Marina V Kameneva, and Zhongjun J Wu. Microscopic investigation of erythrocyte deformation dynamics. *Biorheology*, 43(6):747–765, 2006.

[127] M. Dao, J. Li, and S. Suresh. Spectrin-level and continuum modeling of the large deformation of whole human red blood cells. *Biophysical Journal*, 88(1):3707–3719, 2005.

[128] J. Li, G. Lykotrafitis, M. Dao, and S. Suresh. Cytoskeletal dynamics of human erythrocyte. *Proceedings of the National Academy of Sciences*, 104(12):4937–4942, 2007.

[129] Stuart R. Keller and Richard Skalak. Motion of a tank-treading ellipsoidal particle in a shear flow. *Journal of Fluid Mechanics*, 120:27–47, 1982.

[130] P. J. Hoogerbrugge and J. M. V. A. Koelman. Simulating microscopic hydrodynamic phenomena with dissipative particle dynamics. *EPL (Europhysics Letters)*, 19(3):155, 1992.

[131] P. Español and P. Warren. Statistical mechanics of dissipative particle dynamics. *EPL (Europhysics Letters)*, 30(4):191–196, 1995.

[132] Igor Pivkin and George Karniadakis. Accurate coarse-grained modeling of red blood cells. *Physical Review Letters*, 101(11):118105, 2008.

[133] Dmitry Fedosov, George Karniadakis, and Bruce Caswell. Steady shear rheometry of dissipative particle dynamics models of polymer fluids in reverse poiseuille flow. *The Journal of Chemical Physics*, 132(14):144103, 2010.

[134] Manouk Abkarian, Magalie Faivre, and Annie Viallat. Swinging of red blood cells under shear flow. *Physical Review Letters*, 98(18):188302, 2007.

[135] J M Skotheim and T W Secomb. Red blood cells and other nonspherical capsules in shear flow: oscillatory dynamics and the tank-treading-to-tumbling transition. *Physical Review Letter*, 98(7):078301, 2007.

[136] G. Popescu, Y. Park, R. R. Dasari, K. Badizadegan, and M. S. Feld. Coherence properties of red blood cell membrane motions. *Physical Review E*, 76(3):031902–031906, 2007.

[137] Y. Park, M. Diez-Silva, G. Popescu, G. Lykotrafitis, W. Choi, M. S. Feld, and S. Suresh. Refractive index maps and membrane dynamics of human red blood cells parasitized by plasmodium falciparum. *Proceedings of the National Academy of Sciences, USA*, 105(37):13730–13735, 2008.

[138] J. Deschamps, V. Kantsler, E. Segre, and V. Steinberg. Dynamics of a vesicle in general flow. *Proceedings of the National Academy of Sciences*, 106(28):11444–11447, 2009.

[139] C. D. Eggleton and A. S. Popel. Large deformation of red blood cell ghosts in a simple shear flow. *Physics of Fluids*, 10(8):1834–1845, 1998.

[140] Wing Kam Liu, Yaling Liu, David Farrell, Lucy Zhang, X. Sheldon Wang, Yoshio Fukui, Neelesh Patankar, Yongjie Zhang, Chandrajit Bajaj, Junghoon Lee, Juhee Hong, Xinyu Chen, and Huayi Hsu. Immersed finite element method and its applications to biological systems. *Computer Methods in Applied Mechanics and Engineering*, 195(13-16):1722–1749, 2006.

[141] Prosenjit Bagchi, Paul C. Johnson, and Aleksander S. Popel. Computational fluid dynamic simulation of aggregation of deformable cells in a shear flow. *Journal of Biomechanical Engineering*, 127(7):1070–1080, 2005.

[142] S. Chien and L. A. Lang. Physicochemical basis and clinical implications of red cell aggregation. *Clinical Hemorheology*, 7:71–91, 1987.

[143] Jacob Israelachvili. *Intermolecular and Surface Forces, Second Edition: With Applications to Colloidal and Biological Systems (Colloid Science)*. Academic Press, 2nd edition, 1992.

[144] D. E. Brooks and G. V. F. Seaman. The effect of neutral polymers on the electrokinetic potential of cells and other charged particles : I. models for the zeta potential increase. *Journal of Colloid and Interface Science*, 43(3):670–686, 1973.

[145] B. Neu and H.J. Meiselman. Depletion-mediated red blood cell aggregation in polymer solutions. *Biophysical Journal*, 83(5):2482–2490, 2002.

[146] K. Buxbaum, E. Evans, and D. E. Brooks. Quantitation of surface affinities of red blood cells in dextran solutions and plasma. *Biochemistry*, 21(13):3235–3239, 1982.

[147] Charles Peskin. The immersed boundary method. *Acta Numerica*, 11(-1):479–517, 2002.

[148] Lucy Zhang, Axel Gerstenberger, Xiaodong Wang, and Wing Kam Liu. Immersed finite element method. *Computer Methods in Applied Mechanics and Engineering*, 193(21-22):2051 – 2067, 2004.

[149] Yaling Liu and Wing Kam Liu. Rheology of red blood cell aggregation by computer simulation. *Journal of Computational Physics*, 220(1):139 – 154, 2006.

[150] J Kurchan. In and out of equilibrium. *Nature*, 433(7023):222–225, 2005.

[151] P L Blackshear, Jr, F D Dorman, and J H Steinbach. Some mechanical effects that influence hemolysis. *Transactions - American Society for Artificial Internal Organs*, 11:112–117, 1965.

[152] D. Hanle, E. Harrison, A. Yoganathan, and W. Corcoran. Turbulence downstream from the ionescu-shiley bioprosthesis in steady and pulsatile flow. *Medical and Biological Engineering and Computing*, 25(6):645–649, 1987-11-01.

[153] M. Grigioni, C. Daniele, G. D'Avenio, and V. Barbaro. A discussion on the threshold limit for hemolysis related to Reynolds shear stress. *Journal of Biomechanics*, 32(10):1107–1112, 1999.

[154] P. C. Lu, H. C. Lai, and J. S. Liu. A reevaluation and discussion on the threshold limit for hemolysis in a turbulent shear flow. *Journal of Biomechanics*, 34(10):1361–1364, 2001.

[155] A M Sallam and N H Hwang. Human red blood cell hemolysis in a turbulent shear flow: contribution of Reynolds shear stresses. *Biorheology*, 21(6):783–97, 1984.

[156] Masao Doi and Takao Ohta. Dynamics and rheology of complex interfaces. I. *The Journal of Chemical Physics*, 95(2):1242–1248, 1991.

[157] P. L. Maffettone and M. Minale. Equation of change for ellipsoidal drops in viscous flow. *Journal of Non-Newtonian Fluid Mechanics*, 78(2-3):227–241, 1998.

[158] E. D. Wetzel and C. L. Tucker. Area tensors for modeling microstructure during laminar liquid-liquid mixing. *International Journal of Multiphase Flow*, 25(1):35–61, 1999.

[159] M. Dao, J Li, and S. Suresh. Molecularly based analysis of deformation of spectrin network and human erythrocyte. *Materials science and engineering c-biomimetic and supramolecular systems*, 26(8):1232–1244, 2006.

[160] Pep Español. Fluid particle model. *Physical Review E*, 57(3):2930–2948, 1998.

[161] E. Evans, V. Heinrich, F. Ludwig, and W. Rawicz. Dynamic tension spectroscopy and strength of biomembranes. *Biophysical journal*, 85(4):2342–2350, 2003.

[162] M.P. Allen and D.J. Tildesley. *Computer simulation of liquids*. Clarendon Press, 1999.

[163] S. Petitjean. A survey of methods for recovering quadrics in triangle meshes. *ACM Computing Surveys (CSUR)*, 34(2):211–262, 2002.

[164] RM Hochmuth, PR Worthy, and EA Evans. Red cell extensional recovery and the determination of membrane viscosity. *Biophysical Journal*, 26(1):101–114, 1979.

[165] K.C. Melikov, V.A. Frolov, A. Shcherbakov, A.V. Samsonov, Y.A. Chizmadzhev, and L.V. Chernomordik. Voltage-induced nonconductive pre-pores and metastable single pores in unmodified planar lipid bilayer. *Biophysical Journal*, 80(4):1829–1836, 2001.

[166] K.K. Yeleswarapu, J.F. Antaki, M.V. Kameneva, and K.R. Rajagopal. A mathematical model for shear-induced hemolysis. *Artificial Organs*, 19(7):576–582, 1995.

[167] A.W.L. Jay. Viscoelastic properties of the human red blood cell membrane:: I. deformation, volume loss, and rupture of red cells in micropipettes. *Biophysical Journal*, 13(11):1166–1182, 1973.

[168] E.A. Evans and P.L. La Celle. Intrinsic material properties of the erythrocyte membrane indicated by mechanical analysis of deformation. *Blood*, 45(1):29, 1975.

[169] L.Z. Andrew and K.C. Clark. A red cell deformation model for hemolysis in cross flow membrane plasmapheresis. *Chemical engineering communications*, 30(3-5):191–207, 1984.

[170] S. Chien, S.A. Luse, and C.A. Bryant. Hemolysis during filtration through micropores: a scanning electron microscopic and hemorheologic correlation. *Microvascular research*, 3(2):183–203, 1971.

[171] PF Leblond, L. Coulombe, et al. The measurement of erythrocyte deformability using micropore membranes. a sensitive technique with clinical applications. *The Journal of laboratory and clinical medicine*, 94(1):133, 1979.

[172] Summary. *Scandinavian Journal of Haematology*, 17:52–53, 1976.

[173] PC Anderson and RE Lovrien. Human red cell hemolysis rates in the subsecond to seconds range. an analysis. *Biophysical Journal*, 20(2):181–191, 1977.

[174] R. Skalak and S. Chien. *Handbook of bioengineering*. McGraw-Hill New York, 1987.

[175] P. Seeman, WO Kwant, T. Sauks, and W. Argent. Membrane expansion of intact erythrocytes by anesthetics. *Biochimica et Biophysica Acta (BBA)-Biomembranes*, 183(3):490–498, 1969.

[176] R.J. Forstrom. *A new measure of erythrocyte membrane strength: the jet fragility test*. PhD thesis, University of Minnesota., 1969.

[177] M D. DE Tullio, A. Cristallo, E. Balaras, and R. Verzicco. Direct numerical simulation of the pulsatile flow through an aortic bileaflet mechanical heart valve. *Journal of Fluid Mechanics*, 622:259–290, 2009.

[178] D.P. Tieleman, H. Leontiadou, A.E. Mark, and S.J. Marrink. Simulation of pore formation in lipid bilayers by mechanical stress and electric fields. *Journal of the American Chemical Society*, 125(21):6382–6383, 2003.

[179] P.T. Sander and S.W. Zucker. Inferring surface trace and differential structure from 3-d images. *Pattern Analysis and Machine Intelligence, IEEE Transactions on*, 12(9):833–854, 1990.

[180] E.M. Stokely and S.Y. Wu. Surface parametrization and curvature measurement of arbitrary 3-d objects: five practical methods. *IEEE Transactions on pattern analysis and machine Intelligence*, 14(8):833–840, 1992.

[181] F.P. Ferrie, J. Lagarde, and P. Whaite. Darboux frames, snakes, and superquadrics: Geometry from the bottom up. *Pattern Analysis and Machine Intelligence, IEEE Transactions on*, 15(8):771–784, 1993.

[182] B. Hamann. Curvature approximation for triangulated surfaces. In *Geometric modelling*, pages 139–153. Springer-Verlag, 1993.